Calculation of correction factors for three detectors in small composite clinical fields for the CyberKnife radiosurgery system

Eric Jessie Christiansen

Master of Science

Medical Physics Unit

McGill University

Montreal, Quebec

15 December, 2015

A thesis submitted to McGill University in partial fulfillment of the requirements of the degree of Master of Science in Medical Radiation Physics.

ACKNOWLEDGEMENTS

First and foremost, I would like to thank my supervisor Eric Vandervoort for his guidance and support in all aspects of this project. Also at TOHCC, I would like to thank Jason Belec for his expertise in beam modeling, as well as my colleagues Miro Vujicic and Raanan Marants for many helpful discussions throughout the year. I would like to especially thank Brenda Clark who gave me my first experience in medical physics as a summer student at TOHCC.

The modeling of the CyberKnife beam would not have been possible without the help of Warren Kilby (Accuray, Inc.), who answered my many detailed questions regarding the linac head. Bryan Muir (NRC) helped greatly in my understanding of the `egs_chamber` user code and how to apply it to detector modeling. I would like to thank Bryan and Warren for their help.

My formal education in medical physics began at McGill University, in the Medical Physics Unit. That first year of classes was the most challenging and most rewarding year of my post-secondary education, and I will not soon forget what I have learned. I am grateful to the teachers and clinical staff for passing on their knowledge in this way. I would like to especially thank Jan Seuntjens, who taught me the principles of medical radiation physics forming the foundation of this study.

I would like to thank my family, for their love and support: Melanie Christiansen, Greg and Paula Christiansen, and my mom Dominique Goulet. I would not be here without them. Last, but certainly not least, I am forever grateful to Kyra for her endless love and encouragement.

ABSTRACT

A formalism has been proposed in which correction factors $k_{Q_{\text{clin}},Q_{\text{msr}}}^{f_{\text{clin}},f_{\text{msr}}}$ are used to correct dosimeter response in small composite clinical fields relative to that in a larger machine-specific reference (MSR) field. The formalism has been applied to calculate $k_{Q_{\text{clin}},Q_{\text{msr}}}^{f_{\text{clin}},f_{\text{msr}}}$ for 18 clinical fields delivered by the CyberKnife radiosurgery system, and for 3 detectors: the Exradin A16 and A26 microchambers, and the W1 plastic scintillator. The corrections for the microchambers were large, primarily due to the presence of the low-density air cavity, and the volume averaging effect. The scintillator was found to be correction-free for most fields, and therefore able to be used to measure corrections for other detectors. The clinical fields were grouped into 6 plan-classes according to commonly shared characteristics. The suitability of using a plan-class specific reference (PCSR) field to represent the detector response of each field within the class was investigated. Plan-classes comprising isocentric fields were well represented by a PCSR field (clinical and PCSR field corrections differed by $\leq 1.5\%$). Non-isocentric field corrections were calculated at the point of maximum dose and a point selected to minimize the dose gradient near the detector. $k_{Q_{\text{clin}},Q_{\text{msr}}}^{f_{\text{clin}},f_{\text{msr}}}$ varied between these two points by as much as 4.6%, reflecting a large variation in dosimetric conditions. Furthermore, the variability of $k_{Q_{\text{clin}},Q_{\text{msr}}}^{f_{\text{clin}},f_{\text{msr}}}$ within a single plan-class was found to improve at the former point for certain classes, and at the latter for others. This precludes the use of a PCSR field for non-isocentric plan-classes until a method is found that can select a point at which the variation of $k_{Q_{\text{clin}},Q_{\text{msr}}}^{f_{\text{clin}},f_{\text{msr}}}$ within a wide range of plan-classes is consistently small.

RÉSUMÉ

Un formalisme a été proposé dans lequel les facteurs de correction $k_{Q_{\text{clin}},Q_{\text{msr}}}^{f_{\text{clin}},f_{\text{msr}}}$ sont utilisés pour corriger la réponse de dosimètre dans les petits champs cliniques composites en comparaison avec la réponse dans un champ de référence plus grand et spécifique à l'accélérateur. Le formalisme a été appliqué pour calculer $k_{Q_{\text{clin}},Q_{\text{msr}}}^{f_{\text{clin}},f_{\text{msr}}}$ pour 18 champs cliniques fournis par le système de radiochirurgie CyberKnife et pour 3 détecteurs: les microchambres Exradin A16 et A26 et le scintillateur au plastique W1. Les corrections pour les microchambres était grandes, principalement en raison de la présence de la cavité d'air de faible densité et l'effet du volume moyen. Il a été trouvé que le scintillateur a un facteur de correction nul pour la plupart des champs, ce qui lui permet d'être utilisé pour mesurer les facteurs de corrections pour d'autres détecteurs. Les champs cliniques ont été regroupé en 6 classes de plan en fonction de caractéristiques partagées. La pertinence d'utiliser un champ de référence spécifique à la classe de plan (RSCP) pour représenter la réponse du détecteur pour chaque champ clinique au sein de sa classe a été étudiée. Les classes de plan comprenant les champs isocentriques étaient bien représentées par un champ RSCP (les corrections pour les champs cliniques et RSCP différaient de $\leq 1,5\%$). Les corrections pour les champs non-isocentriques ont été calculées au point de la dose maximale et à un point choisi pour minimiser le gradient de dose près du détecteur. La variation de $k_{Q_{\text{clin}},Q_{\text{msr}}}^{f_{\text{clin}},f_{\text{msr}}}$ entre ces deux points est d'autant que 4,6%, ce qui indique une variation importante des conditions dosimétriques. De plus, la variation des $k_{Q_{\text{clin}},Q_{\text{msr}}}^{f_{\text{clin}},f_{\text{msr}}}$ d'une même classe de plan peut être minimisée en utilisant le premier point pour certaines classes et le deuxième point pour les autres classes. Ceci exclut l'utilisation d'un champ RSCP pour les classes de plan non-isocentriques jusqu'à ce qu'une méthode soit trouvée pour sélectionner un point qui permettra une faible variation des $k_{Q_{\text{clin}},Q_{\text{msr}}}^{f_{\text{clin}},f_{\text{msr}}}$ pour une grande diversité de classe de plan.

TABLE OF CONTENTS

LIST OF TABLES

LIST OF FIGURES

LIST OF ABBREVIATIONS

3D-CRT: three-dimensional conformal radiotherapy

AAPM: American Association of Physicists in Medicine

ABS: acrylonitrile butadiene styrene

BCSE: bremsstrahlung cross-section enhancement

CoP: Code of Practice

CPE: charged particle equilibrium

CS: correlated sampling

CT: computed tomography

DBS: directional bremsstrahlung splitting

DNA: deoxyribonucleic acid

EBRT: external beam radiotherapy

EPOM: effective point of measurement

FFF: flattening-filter free

FWHM: full width at half maximum

ICRU: International Comission on Radiation Units and Measurements

IGRT: image guided radiotherapy

IMAT: intensity modulated arc therapy

IMRT: intensity modulated radiotherapy

IPSS: intermediate phase-space storage

linac: linear accelerator

MLC: multi-leaf collimator

MSR: machine-specific reference

MU: monitor unit

NIST: National Institute of Standards and Technology

NRC: National Research Council

OAR: off-axis ratio

OF: output factor

PCSR: plan-class specific reference

PDD: percentage depth-dose

PMMA: poly(methyl methacralate)

RMSD: root-mean-square deviation

RNG: random number generator

RR: Russian Roulette

SAD: source to axis distance

SDD: source to detector distance

SRS: stereotactic radiosurgery

SSD: source to surface distance

TG: Task Group

TOHCC: The Ottawa Hospital Cancer Centre

TPS: treatment planning system

voxel: volume element

XCSE: photon cross-section enhancement

XML: Extensible Markup Language

CHAPTER 1
Introduction

1.1 External Beam Radiation Therapy

Since the discovery of x-rays by Wilhelm Roentgen in 1895, ionizing radiation has been used for the treatment of cancer [1]. The deoxyribonucleic acid (DNA) molecules within living cells are damaged by ionizing radiation, leading to cell death. The death of cancerous cells leads to tumour control and an effective treatment of the patient; this is the desired outcome of radiotherapy. The death of normal, non-cancerous cells may lead to acute effects such as inflammation and hemorrhage, or to late effects such as fibrosis, atrophy, and lens opacification. One of the basic quantities of ionizing radiation is dose, which is defined as the energy deposited by ionizing radiation within an infinitesimal volume of a given medium, divided by the mass of that volume, typically measured in Gray ($1\,\mathrm{Gy} = 1\,\mathrm{J/kg}$). Cancerous cells are more sensitive to radiation than are normal cells, especially when the radiation is delivered over multiple smaller dose treatments, a technique called fractionation [2]. This is exploited in radiation therapy to create an effective treatment plan that is as safe for the patient as possible.

External beam radiotherapy (EBRT) is one of the main methods of using ionizing radiation to treat cancer. EBRT delivers beams of radiation, typically energetic electrons or photons, from outside the patient's body. The main technological improvements in EBRT have been to increase the geometric accuracy of radiation delivery, leading to improved conformality of the dose distribution to the tumour, and the reduction of dose to organs at risk. The invention of the ^{60}Co unit by Harold E. Johns in the 1950s, and later the medical linear accelerator, served to boost the photon energies available in the clinic, which improved the treatment of tumours seated deeply within the patient. The multi-leaf collimator (MLC), first invented in 1965, has been increasingly used in more dynamic deliveries to improve

treatment conformality, minimzing the dose delivered to healthy tissue while maximizing the dose received by the tumour [2].

The use of image guided radiotherapy (IGRT) has greatly improved the accuracy of radiation delivery to the target. The patient is typically imaged daily, just before treatment, ensuring that the position of the target and organs at risk inside the patient has not varied between fractions. Movement of these volumes within the patient may be detected and corrected for, increasing the total precision of the treatment [2].

1.1.1 Gantry-Based Linear Accelerators

The medical linear accelerator (linac) is the most common implementation of EBRT. Electrons are accelerated through evacuated structures named accelerating wave guides to a specific energy (usually in the range 4 MeV to 25 MeV). To produce a photon beam, these energetic electrons are made to strike a target, usually composed of copper or tungsten, inside which radiative interactions with the constituent atoms take places, giving rise to bremsstrahlung photons. The resulting photon beam is shaped first using a primary conical collimator, then using two pairs of secondary collimators, called jaws. These secondary collimators define rectangular fields typically with a maximum dimension of $400 \times 400\,\mathrm{mm}^2$. A flattening filter may be used to modulate the photon fluence, resulting in a flat dose distribution at a specific depth within the patient; increasingly, flattening-filter free (FFF) linacs are used, in which the MLC is used to dynamically modulate the dose [3]. The output of the linac is tracked using an air-filled ionization chamber downstream from the primary collimator, called the monitor chamber [2].

The typical linac is mounted on a gantry such that it can rotate around a point in space, usually placed within the patient for most treatments. This point is called the isocentre; it is typically at a source to axis distance (SAD) of 1000 mm. The modern gantry-based linac employs the MLC in a variety of ways, depending on the needs of the treatment. The simplest method is to shape the MLC to the contour of the target with the linac at fixed positions around the patient; this is referred to as three-dimensional conformal radiotherapy

(3D-CRT). Intensity modulated radiotherapy (IMRT) involves using the MLC to modulate the intensity of the beam across the field. This can be done in either step and shoot mode, in which modulated fields are delivered with a sequence of static subfields, or dynamic mode, in which the fields are delivered while the leaves are in motion. Finally, in intensity modulated arc therapy (IMAT), the leaves of the MLC are set in motion as the gantry rotates around the patient. Each successive implementation of has MLC generally resulted in a more conformal dose distribution than the last [2].

1.1.2 Robot-Based Linear Accelerators

Lesions in the brain can be treated using stereotactic radiosurgery (SRS), a method of radiotherapy in which large doses of radiation (10 Gy to 60 Gy) are delivered in a single fraction. This is considered an ablative dose, as the intent is to destroy the target instead of relying on the differential in cell death of the tumour versus normal tissues [4]. Consequently, a position accuracy in the millimeter range is required in order to irradiate the target safely. This accuracy has historically been achieved by fixing the patient to the treatment couch of a conventional linac using a rigid frame that is invasively fixed to the patient's skull (frame-based radiosurgery). Recently, however, frameless radiosurgery systems which rely on in-room imaging systems, such as CyberKnife, have been implemented in the clinic. The CyberKnife radiosurgery system (Accuray, Inc.) consists of a miniature 6 MV linac mounted on an industrial robotic manipulator, combined with two orthogonal x-ray imagers which localize the patient with a high degree of accuracy. The photon beam is FFF, and is shaped by one of twelve fixed collimators, ranging in size from 5 mm to 60 mm [2].

The robotic manipulator, or arm, has a much larger range of motion than the gantry-based linacs described in Section 1.1.1. In theory, radiation could be delivered from almost any position around patient, however, in clinical treatments, the CyberKnife unit is constrained to direct beams only in certain fixed points arranged in a sphere around the patient, called nodes. Nodes are arranged in sets, named paths, each path optimized to treat a different part of the body. The nodes within the trigeminal neuralgia path lie closest to

the patient, with an average SAD of 700 mm; the skull path has an average SAD of 800 mm; and the nodes within the body path are typically 1000 mm from the centre of the sphere. A single treatment usually only uses nodes from a single path, though this is not necessary. Conversely, clinical fields are typically optimized to use only a subset of the nodes within a single path, in order to improve the conformality of the dose distribution to the specific target, limit the dose to organs at risk, and reduce the total treatment time.

There are two main delivery methods which CyberKnife can use to treat the patient: isocentric and non-isocentric delivery. In the isocentric delivery, the central axes of each beam at every node position used all coincide at a common point within the patient. This delivery typically results in spherical dose distributions. More irregularly shaped lesions, which constitute the majority of cases, are treated using non-isocentric delivery, in which the targets of each beam are not constrained to coincide at a common point. Instead, the beam targets are randomly distributed on the surface of the targeted volume within the patient. The smallest collimators (5 mm, 7.5 mm, and 10 mm in diameter) are used to further improve the conformality of dose distributions, especially for lesions with small, irregularly shaped features, and for sites close to particular organs at risk.

One of the primary roles of the clinical medical physicist is to ensure that the large amount of complex technology used to treat the patient is operating correctly to deliver the amount of radiation, or dose, as prescribed by the physician. This study is concerned with improving the accuracy of determining dose within clinical treatments delivered by the CyberKnife radiosurgery system.

1.2 Reference Dosimetry

The techniques used to calibrate the dose output of medical linear accelerators are referred to as clinical reference dosimetry; the current Code of Practice (CoP) for reference dosimetry in North America is described in the American Association of Physicists in Medicine (AAPM) report of Task Group 51 (TG-51) [5] and its addendum [6]. The calibration requires the determination of the dose to water in specific reference conditions for a

given number of monitor units (MU) collected in the monitor chamber. The reference conditions for photon beams are: a $100 \times 100\,\mathrm{mm}^2$ field incident on a water tank at 1000 mm source to surface distance (SSD), with the reference point at a depth of 100 mm in water. The experimental determination of dose to water at this point is done using an air-filled ionization chamber, the calibration of which is traceable to national standards of absorbed dose to water. In Canada, this is accomplished using primary-standard water calorimetry at the National Research Council (NRC). Reference class ion chambers are calibrated in water in a ^{60}Co gamma ray beam, having a mean photon energy of 1.25 MeV. The quality of a beam refers to its spectrum of photon energies; for the aforementioned cobalt beam, the quality is denoted by Q_0. The absorbed dose to water calibration coefficient N_{D,w,Q_0}, typically measured in cGy/nC, is then defined using the following relation:

$$D_{w,Q_0}^{f_{\mathrm{ref}}} = M_{Q_0}^{f_{\mathrm{ref}}} \cdot N_{D,w,Q_0} \tag{1.1}$$

Here, D_{w,Q_0} is the dose to water in the cobalt beam, and M_{Q_0} is the charge collected in the chamber in the same beam, corrected for polarity, recombination, electrometer, and pressure and temperature effects [5]. f_{ref} denotes the reference field conditions that are used in the chamber calibration.

Equation (1.1) defines the relationship between dose to water and charge measured by the calibrated chamber only in the ^{60}Co beam with quality Q_0, through the chamber and beam quality-specific calibration coefficient N_{D,w,Q_0}. A clinical linear accelerator delivers an x-ray beam with quality Q different from Q_0; therefore the calibration coefficient for the chamber in the clinical beam is $N_{D,w,Q_0} \neq N_{D,w,Q}$. The beam quality conversion factor k_{Q,Q_0} relates these two calibration coefficients:

$$k_{Q,Q_0} = \frac{N_{D,w,Q}}{N_{D,w,Q_0}} \tag{1.2a}$$

$$k_{Q,Q_0} = \frac{D_{w,Q}^{f_{\mathrm{ref}}} / M_{Q}^{f_{\mathrm{ref}}}}{D_{w,Q_0}^{f_{\mathrm{ref}}} / M_{Q_0}^{f_{\mathrm{ref}}}} \tag{1.2b}$$

Therefore the equation for the dose to water in the clinical field with beam quality k_{Q,Q_0} is

$$D_{w,Q}^{f_{\text{ref}}} = M_Q^{f_{\text{ref}}} \cdot N_{D,w,Q_0} \cdot k_{Q,Q_0} \tag{1.3}$$

k_{Q,Q_0} is primarily determined by the ratio of mean restricted stopping power ratios water-to-air in the beam qualities of interest Q and Q_0: $\left[\left(\frac{\overline{L}}{\rho}\right)_{air}^{w}\right]_{Q_0}^{Q}$; this behaviour is predicted by the Bragg-Gray and Spencer-Attix cavity theories. Other factors not included in cavity theory are required in order to correct for the presence of the non-water components of the chamber, including the stem (P_{stem}), central electrode (P_{cel}), and wall (P_{wall}), and for changes in the electron spectrum due to the introduction of an air cavity (P_{fl}, P_ρ, and P_{vol}). The total expression for the beam quality correction factor is therefore [7, 8]:

$$k_{Q,Q_0} = \left[P_{\text{stem}} P_{\text{cel}} P_{\text{wall}} \left(\frac{\overline{L}}{\rho}\right)_{air}^{w} P_{\text{fl}} P_\rho P_{\text{vol}}\right]_{Q_0}^{Q} \tag{1.4}$$

As stated previously, the correction factor k_{Q,Q_0} is a function of the beam quality Q. TG-51 and its addendum specify Q using the beam quality specifier $\text{PDD}(10)_{\text{X}}$, which represents the photon component of the percentage depth-dose (PDD) at 100 mm depth for a $100 \times 100\,\text{mm}^2$ field on the surface of a water phantom at an SSD of 1000 mm. A beam composed of more energetic photons will in general have a larger $\text{PDD}(10)_{\text{X}}$ than one with less energetic photons (see Section 2.2.1). The addendum to the TG-51 report includes a procedure to calculate the k_{Q,Q_0} correction factor for calibrated reference chambers of many different models, using the beam quality specifier $\text{PDD}(10)_{\text{X}}$. This procedure is based on Monte Carlo calculations of k_{Q,Q_0} [7], which were subsequently verified by calorimetric measurements [9, 10]. In general, the k_{Q,Q_0} correction factor decreases as the beam quality specifier $\text{PDD}(10)_{\text{X}}$ increases. The typical range of k_{Q,Q_0} values is from 0.96 at high energies (24 MeV) to 1 at the ^{60}Co gamma ray energy (1.25 MeV) [5, 7].

1.3 Clinical Field Dosimetry

One of the responsibilities of the clinical medical physicist is to determine the dose to water delivered to the patient in complex clinical fields in order to ensure that the dose

prescribed by the physician is delivered accurately. Contemporary clinical fields are generally composed of multiple subfields; these are called composite fields. A single field is referred to as a static field. While *in vivo* dosimetry is possible [11] for clinical field dosimetry, more typically these types of measurements are performed prior to treatment with a surrogate, called a phantom. The phantom is usually constructed of water, water-equivalent or tissue-mimicking plastics, balancing the two opposing requirements of simplicity and similarity to the patient. Measurements are performed by inserting a suitable detector inside the phantom and delivering the composite fields intended for patient treatment. In this study, the clinical field detectors investigated were ion chambers and plastic scintillators, but diodes, diamond detectors, thermoluminescent dosimeters, and radiochromic film may also be used. Ion chambers used for small clinical field dosimetry are usually smaller than those used for reference dosimetry ($\sim 1\,\mathrm{mm}^3$ versus $\sim 100\,\mathrm{mm}^3$); these are therefore referred to as microchambers.

The detectors used for clinical field dosimetry typically require a cross-calibration against a calibrated reference class ion chamber in the reference field with beam quality Q (see Section 1.2). First, the dose to water is determined in reference conditions, using the calibrated ion chamber. Then, the corrected signal of the clinical field detector is measured in the same setup. Corrections for microchambers were listed in Section 1.2; the plastic scintillator requires a correction to eliminate the contaminating Cerenkov signal [12]. The cross-calibration is done by considering a modification of Equation (1.3):

$$N_{D,w,Q_0} \cdot k_{Q,Q_0} = \frac{D_{w,Q}^{f_{\mathrm{ref}}}}{M_Q^{f_{\mathrm{ref}}}} \tag{1.5}$$

The product $N_{D,w,Q_0} \cdot k_{Q,Q_0}$ is understood to be specific to the new detector, whether it is a microchamber or plastic scintillator. This gives the calibration coefficient for the new detector in the reference field with beam quality Q. Many simple clinical fields are primarily composed of larger fields. A correction factor from the reference field with beam quality Q, though technically required, is generally not considered for these fields, as the dosimetric

conditions are similar to those in the reference field [13]. Therefore the calibration coefficient for these simple clinical fields is taken to be this product $N_{D,w,Q_0} \cdot k_{Q,Q_0}$.

1.3.1 Small Field Conditions

As stated in Section 1.1.2, clinical fields for the CyberKnife radiosurgery system often use many small fields in order to deliver conformal dose distributions to small and/or complex targets. The small fields comprising these clinical fields are dramatically different from the $100 \times 100\,\mathrm{mm}^2$ reference field. The difference in field size can greatly affect the detector response in composite clinical fields relative to the reference field, which may require an additional correction factor to the calibration coefficient measured in the cross-calibration step described above.

Before the final point is explored, it is necessary to precisely define the notion of a small field. Commonly, field sizes of less than $30 \times 30\,\mathrm{mm}^2$ are considered to be small, but a more scientific approach is required to define small fields. There are three factors that determine if a radiation field is small or not, two of which are related to the size of the photon source emitted from the x-ray target and the collimation system; the third is related to the detector used to measure the field [14]. First, a field is considered small if the collimator defining the field partially occludes the photon source. This leads to a large decrease in the dose to water output of the linear accelerator with decreasing field size.

The second factor is related to the concept of charged particle equilibrium (CPE). Energetic electrons and positrons that are produced in matter by interactions initiated by megavoltage photon beams have a considerable forward and lateral range in water, on the order of tens of millimetres [15]. CPE is realized in an infinitesimal volume inside a medium if, for every charged particle of a given type and energy departing the volume is replaced by a charged particle of the same type and energy from outside the volume [1]. Disequilibrium exists, therefore, when the charged particles leaving the volume are not adequately replaced by those entering the volume. For small fields, the concept of lateral charged particle disequilibrium is important: a photon field is considered to be small if its radius is less than the

lateral range of charged particles. In this case, charged particles leaving the beam central axis (and any point within the field) travel outside of the field and therefore cannot be fully replaced: lateral disequilibrium exists across the entire small field. The lack of lateral CPE also leads to a decrease to the dose to water output of the linear accelerator.

The final factor that is used to determine if a field is small or not is the size and type of detector used. This factor will help in the understanding of the small field correction factor described previously. Neglecting for a moment all other structural or electrical components, a radiation dosimeter is composed of a non-water active volume, in which dose is deposited; the signal measured by the detector is proportional to the average dose across the entire volume. When the size of the volume is larger than the radiation field, significant volume averaging can occur. The dose distribution inside the active volume is highly non-uniform, such that the mean dose within the volume is not representative of the dose to a point in the centre of the volume for a detector located on the beam central axis. This leads to a decrease in the experimental value of the dose output of the linear accelerator if only the reference dosimetry calibration of Equation (1.5) is considered; this effect must be corrected for using the perturbation factor P_{vol} (see Equation (1.4)). Francescon *et al.* calculated, using Monte Carlo methods, P_{vol} values in the range of 1.097 to 1.227 in a 5 mm CyberKnife field for the PTW PinPoint 31014 microchamber (2 mm diameter) [16], indicating that this detector under-responds by at least 10% in this small field when only volume averaging is considered.

If lateral CPE does not exist in the field under consideration, the presence of a non-water volume can present an additional perturbation to the detector response. For example, air-filled microchambers are frequently used for clinical field dosimetry. The Fano theorem states that if CPE is established, the dose to a volume is independent of its density [17]. In general, the opposite is also true, implying that a low-density volume (such as those found in microchambers) will present a perturbation to the dose distribution if lateral CPE does not exist [14, 16, 18]. This effect also leads to a decrease in the experimentally determined dose output of the linear accelerator, similar to the volume averaging effect described previously.

The perturbation factor P_ρ is applied to correct for the variation in dose due to the low-density volume. Francescon *et al.* calculated P_ρ values in the range of 1.090 to 1.300 in the 5 mm CyberKnife field for the PinPoint 31014 microchamber [16]. This presents an additional 10% under-response that must be corrected for if this detector were to be used in the 5 mm field.

1.3.2 Small Clinical Field Dosimetry Formalism

A formalism for the dosimetry of small clinical fields was developed [13] in order to extend the correction factors found in reference dosimetry CoPs to these nonstandard fields. This formalism consists of two related routes to determine the dose to water at a point in a clinical field through a series of correction factors. Strictly speaking, the formalism applies only to ion chambers, but it can be generalized to include any detector whose measured signal is proportional to the dose deposited in its active volume.

Both routes are extensions of the reference dosimetry protocols described in Section 1.2. The first route introduces a static machine-specific reference (MSR) field f_{msr} for treatment machines that cannot establish the conventional reference field of $100 \times 100\,\mathrm{mm}^2$. For the case of CyberKnife, the MSR field is taken to be the 60 mm diameter collimator [13]. A correction factor $k_{Q_{\mathrm{msr}},Q}^{f_{\mathrm{msr}},f_{\mathrm{ref}}}$ is required to correct for the difference in detector response between the reference field with beam quality Q and the MSR field with beam quality Q_{msr}. It is expected that neither the beam quality nor detector response will change substantially between the reference and MSR fields, therefore the $k_{Q_{\mathrm{msr}},Q}^{f_{\mathrm{msr}},f_{\mathrm{ref}}}$ correction factor should be close to unity [13]. The detector response in the small clinical field f_{clin} relative to the MSR field is corrected for using a similar correction factor, $k_{Q_{\mathrm{clin}},Q_{\mathrm{msr}}}^{f_{\mathrm{clin}},f_{\mathrm{msr}}}$. This correction factor contains the perturbation factors P_{vol} and P_ρ described in Section 1.3.1. The definitions of

these two correction factors are similar:

$$k^{f_{\text{msr}},f_{\text{ref}}}_{Q_{\text{msr}},Q} = \frac{D^{f_{\text{msr}}}_{w,Q_{\text{msr}}}/M^{f_{\text{msr}}}_{Q_{\text{msr}}}}{D^{f_{\text{ref}}}_{w,Q}/M^{f_{\text{ref}}}_{Q}} \tag{1.6a}$$

$$k^{f_{\text{clin}},f_{\text{msr}}}_{Q_{\text{clin}},Q_{\text{msr}}} = \frac{D^{f_{\text{clin}}}_{w,Q_{\text{clin}}}/M^{f_{\text{clin}}}_{Q_{\text{clin}}}}{D^{f_{\text{msr}}}_{w,Q_{\text{msr}}}/M^{f_{\text{msr}}}_{Q_{\text{msr}}}} \tag{1.6b}$$

The full expression for the absorbed dose to water in the small clinical field f_{clin} can be calculated by extending Equation (1.3), used in reference dosimetry, with the appropriate correction factors specific to the clinical field and detector used:

$$D^{f_{\text{clin}}}_{w,Q_{\text{clin}}} = M^{f_{\text{clin}}}_{Q_{\text{clin}}} \cdot N_{D,w,Q_0} \cdot k_{Q,Q_0} \cdot k^{f_{\text{msr}},f_{\text{ref}}}_{Q_{\text{msr}},Q} \cdot k^{f_{\text{clin}},f_{\text{msr}}}_{Q_{\text{clin}},Q_{\text{msr}}} \tag{1.7}$$

Plan Class Route

In the second route, an additional intermediate field is defined, called the plan-class specific reference (PCSR) field f_{pcsr}. This route may also include the MSR field introduced earlier; this is a requirement if the machine cannot establish the conventional reference field. Before the PCSR field is properly defined, it is instructive to first calculate the expression for the absorbed dose to water in the small clinical field. For this, two additional correction factors are required: $k^{f_{\text{pcsr}},f_{\text{msr}}}_{Q_{\text{pcsr}},Q_{\text{msr}}}$, correcting for the detector response in the PCSR field relative to the MSR field; and $k^{f_{\text{clin}},f_{\text{pcsr}}}_{Q_{\text{clin}},Q_{\text{pcsr}}}$, correcting for the detector response in the clinical field relative to the PCSR field. These correction factors are defined similarly to those in Equation (1.6):

$$k^{f_{\text{pcsr}},f_{\text{msr}}}_{Q_{\text{pcsr}},Q_{\text{msr}}} = \frac{D^{f_{\text{pcsr}}}_{w,Q_{\text{pcsr}}}/M^{f_{\text{pcsr}}}_{Q_{\text{pcsr}}}}{D^{f_{\text{msr}}}_{w,Q_{\text{msr}}}/M^{f_{\text{msr}}}_{Q_{\text{msr}}}} \tag{1.8a}$$

$$k^{f_{\text{clin}},f_{\text{pcsr}}}_{Q_{\text{clin}},Q_{\text{pcsr}}} = \frac{D^{f_{\text{clin}}}_{w,Q_{\text{clin}}}/M^{f_{\text{clin}}}_{Q_{\text{clin}}}}{D^{f_{\text{pcsr}}}_{w,Q_{\text{pcsr}}}/M^{f_{\text{pcsr}}}_{Q_{\text{pcsr}}}} \tag{1.8b}$$

Similarly to the first route, the final equation for the absorbed dose to water in the small clinical field for the second route is as follows:

$$D^{f_{\text{clin}}}_{w,Q_{\text{clin}}} = M^{f_{\text{clin}}}_{Q_{\text{clin}}} \cdot N_{D,w,Q_0} \cdot k_{Q,Q_0} \cdot k^{f_{\text{msr}},f_{\text{ref}}}_{Q_{\text{msr}},Q} \cdot k^{f_{\text{pcsr}},f_{\text{msr}}}_{Q_{\text{pcsr}},Q_{\text{msr}}} \cdot k^{f_{\text{clin}},f_{\text{pcsr}}}_{Q_{\text{clin}},Q_{\text{pcsr}}} \tag{1.9}$$

In order to explain the practical differences between the two routes, it is necessary to define the PCSR field. This field should be representative of a class of clinical plans of interest, in two distinct aspects. First, it should share similar identifiable characteristics as the clinical fields within a plan-class; the class of clinical fields should also be defined according to these characteristics. Some examples of identifiable characteristics that are specific to CyberKnife include the set of collimators that are used to define the total clinical field, the type of delivery that is used (isocentric or non-isocentric), and the beam path. Other characteristics that apply to EBRT in general include the site of the target (e.g. brain metastases, trigeminal neuralgia, lung, prostate), as well as its shape and total volume. The PCSR field should also provide a uniform dose over a volume extending over the dimensions of the detector [13].

The second criterion for determining if the PCSR field is representative of a plan-class of clinical fields is the comparison of the detector response in the clinical fields to the PCSR fields. The detector response in the PCSR field should be similar to the response in each clinical field within the plan-class that it represents. This criterion can be described quantitatively, in two equivalent relations:

$$k_{Q_{\text{pcsr}},Q_{\text{msr}}}^{f_{\text{pcsr}},f_{\text{msr}}} \approx k_{Q_{\text{clin}},Q_{\text{msr}}}^{f_{\text{clin}},f_{\text{msr}}} \tag{1.10a}$$

$$k_{Q_{\text{clin}},Q_{\text{pcsr}}}^{f_{\text{clin}},f_{\text{pcsr}}} \approx 1 \tag{1.10b}$$

This criterion reveals the advantage that the second route of small clinical field dosimetry has over the first. If the detector response in any clinical field within a plan-class is similar to the response in the class's representative PCSR field, then it is possible to remove the final $k_{Q_{\text{clin}},Q_{\text{pcsr}}}^{f_{\text{clin}},f_{\text{pcsr}}}$ correction factor present in Equation (1.9). This not only simplifies the expression for the dose to water, but it eliminates the need to calculate and/or measure $k_{Q_{\text{clin}},Q_{\text{pcsr}}}^{f_{\text{clin}},f_{\text{pcsr}}}$ correction factors for every clinical field for which the absorbed dose to water needs to be determined. This presents a large clinical advantage, as the determination of the $k_{Q_{\text{clin}},Q_{\text{pcsr}}}^{f_{\text{clin}},f_{\text{pcsr}}}$ correction factor, whether through calculation or measurement, can be a lengthy procedure,

whereas clinical field dosimetry often needs to be completed as soon as possible, so that the patient may be treated.

Measuring Clinical Field Correction Factors

The $k^{f_{\text{clin}},f_{\text{msr}}}_{Q_{\text{clin}},Q_{\text{msr}}}$, $k^{f_{\text{pcsr}},f_{\text{msr}}}_{Q_{\text{pcsr}},Q_{\text{msr}}}$, and $k^{f_{\text{clin}},f_{\text{pcsr}}}_{Q_{\text{clin}},Q_{\text{pcsr}}}$ correction factors can be measured by independently measuring the numerator and denominator of each correction factor: $\left(D^{f_{\text{clin}}}_{w,Q_{\text{clin}}}/M^{f_{\text{clin}}}_{Q_{\text{clin}}}\right)$, $\left(D^{f_{\text{msr}}}_{w,Q_{\text{msr}}}/M^{f_{\text{msr}}}_{Q_{\text{msr}}}\right)$, and $\left(D^{f_{\text{pcsr}}}_{w,Q_{\text{pcsr}}}/M^{f_{\text{pcsr}}}_{Q_{\text{pcsr}}}\right)$ ratios of dose and detector signal are measured in the clinical field of interest, the MSR field, and the PCSR field, respectively (see Equations (1.6b), (1.8a), and (1.8b)). The dose to water term ($D^{f_i}_{w,Q_i}$) in each of these ratios may be determined using calorimetry, or using a dosimeter whose response does not exhibit a substantial beam quality or field dependence, such as alanine, radiochromic film, or ferrous sulphate dosimetry [13].

Calculating Clinical Field Correction Factors

Alternatively, the $k^{f_{\text{clin}},f_{\text{msr}}}_{Q_{\text{clin}},Q_{\text{msr}}}$, $k^{f_{\text{pcsr}},f_{\text{msr}}}_{Q_{\text{pcsr}},Q_{\text{msr}}}$, and $k^{f_{\text{clin}},f_{\text{pcsr}}}_{Q_{\text{clin}},Q_{\text{pcsr}}}$ correction factors may be calculated using a Monte Carlo simulation [13]. Similarly to the measurement case, the dose ratios representing the numerator and denominator of the $k^{f_{\text{clin}},f_{\text{msr}}}_{Q_{\text{clin}},Q_{\text{msr}}}$, $k^{f_{\text{pcsr}},f_{\text{msr}}}_{Q_{\text{pcsr}},Q_{\text{msr}}}$, and $k^{f_{\text{clin}},f_{\text{pcsr}}}_{Q_{\text{clin}},Q_{\text{pcsr}}}$ correction factors are calculated. In these simulations, the entire field (clinical, PCSR, or MSR) is modelled, as well as the phantom in which measurements are performed, and the detector of interest. The dose to water $D^{f_i}_{w,Q_i}$ at a point within the phantom can be approximated by calculated the dose to a small volume of water. The measured signal $M^{f_i}_{Q_i}$ cannot be calculated directly; instead, it is assumed that this signal is proportional to the average dose within the active volume of the detector (see Section 1.3.1).

Before the calculation can be performed, a model of the linear accelerator head, including the collimating system and parameters of the electron beam incident on the target, must be constructed and commissioned. The details of the beam model affect the values of correction factors that are derived from the model: Francescon *et al.* [19] have shown that the $k^{f_{\text{clin}},f_{\text{msr}}}_{Q_{\text{clin}},Q_{\text{msr}}}$ correction factor for microchambers in a single 5 mm field can increase by as much 4% when the full width at half maximum (FWHM) of the incident electron beam is increase

from 1.4 mm to 2.6 mm. Therefore the applicability of the calculated correction factors to a particular treatment unity depends partly on the validity of the beam model.

1.3.3 Correction Factors in Small Static Fields: Published Results

The $k_{Q_{\text{clin}},Q_{\text{msr}}}^{f_{\text{clin}},f_{\text{msr}}}$ correction factors have been previously calculated for small static fields produced by the CyberKnife radiosurgery system for a large number of detectors of different type (microchambers, diodes, a diamond detector, and a plastic scintillator), and in varied conditions (variable field size, SAD, and orientation relative to the beam central axis) [16, 19–23]. The following presents a summary of the results in the literature for the A16 microchamber and the W1 plastic scintillator by Exradin, both of which are investigated in this study.

A16 Microchamber

The correction factors for the microchamber in the parallel orientation positioned on central axis were greater than 1, and generally increased with decreasing field size, due to the increase in the volume averaging effect P_{vol} and the increasing lack of lateral CPE (see Section 1.3.1). For the 5 mm collimator, a correction of approximately 10% was required; this decreased to 2% for the 7.5 mm collimator, and 1% for the 10 mm. The diameter of the A16 is approximately equal to half the diameter of the 5 mm field, at 2.4 mm; it has a total active volume of 7 mm^3. When the orientation of the detector was changed to be perpendicular to the central axis, the correction factors increased to as much as 17% above unity for the 5 mm collimator [19, 22]. This can be attributed to the longer length of the air cavity in the stem direction (2.4 mm diameter versus 4.4 mm): the lack of lateral CPE has more of an effect in this orientation than when the stem is parallel to the central axis, thereby increasing the correction factor.

When the SAD was increased from 800 mm to 1000 mm, the $k_{Q_{\text{clin}},Q_{\text{msr}}}^{f_{\text{clin}},f_{\text{msr}}}$ correction factor for the parallel orientation decreased by approximately 3% for the 5 mm collimator; a negligible decrease was observed for the other collimators. When the SAD was decreased to 650 mm, the correction factor increased by 4% for the 5 mm collimator and by 2% for

the 7.5 mm. The observed increase of the correction factor with decreasing SAD can be explained by considering that the effective field size at the detector position decreases with decreasing SAD [22].

The position of the chamber relative to the beam central axis was determined to affect the value of the correction factor by the largest amount. In the parallel orientation, the $k_{Q_{\text{clin}},Q_{\text{msr}}}^{f_{\text{clin}},f_{\text{msr}}}$ for the 5 mm collimator increased from 1.10 on central axis to 1.11 at a position of 1.5 mm off-axis, then decreased sharply to a value of 0.82 at 5 mm off-axis. In the perpendicular orientation, the correction factor increased from 1.17 on central axis to 1.19 at 1.5 mm, then decreased to 0.85 at 5 mm off-axis. The value of $k_{Q_{\text{clin}},Q_{\text{msr}}}^{f_{\text{clin}},f_{\text{msr}}}$ switched from above to below unity at distances 3 mm and 3.5 mm away from the beam central axis for the parallel and perpendicular orientations, respectively [16].

The works summarized above demonstrate that large factors are required to correct the detector response of the A16 microchamber in small static fields to MSR conditions; the exact value of the correction factor is heavily dependent on the specific measurement conditions. In particular, the off-axis position has a large effect on the value of the $k_{Q_{\text{clin}},Q_{\text{msr}}}^{f_{\text{clin}},f_{\text{msr}}}$, as the correction factor can drop below unity when the detector is in the beam penumbra, indicating a signal over-response in these regions.

W1 Plastic Scintillator

The signal response of plastic scintillators has been verified to be independent of energy by several authors through Monte Carlo simulations; this is generally due to the use of water-equivalent materials used throughout the detector's construction [24–26]. In addition, scintillators can be manufactured such that the active volume is small relative to small fields of interest: the active volume of the W1 plastic scintillator is cylindrically shaped, with a diameter of 1.0 mm and length of 3.0 mm. These features result in a detector requiring minimal $k_{Q_{\text{clin}},Q_{\text{msr}}}^{f_{\text{clin}},f_{\text{msr}}}$ correction factors for small static fields. In the parallel orientation, a correction factor no greater than 1.005 is required for any field larger than or equal to 5 mm [16, 22, 23, 27]. In the perpendicular orientation, the correction factor increases to

1.044 for the 5 mm collimator, and returns to unity for the remaining collimators [23]. In this orientation, the detector is presenting the largest dimension of its active volume (3.0 mm) to the beam central axis, therefore some volume averaging is expected.

The minimal correction factors required for the W1 plastic scintillator in the small static fields suggest the possibility of its use as a reference detector to determine the dose to water terms of the $k^{f_{\text{clin}},f_{\text{msr}}}_{Q_{\text{clin}},Q_{\text{msr}}}$, $k^{f_{\text{pcsr}},f_{\text{msr}}}_{Q_{\text{pcsr}},Q_{\text{msr}}}$, and $k^{f_{\text{clin}},f_{\text{pcsr}}}_{Q_{\text{clin}},Q_{\text{pcsr}}}$ correction factors in small clinical fields (see Equations (1.6b), (1.8a), and (1.8b)).

1.3.4 Correction Factors in Clinical Fields: Published Results

Correction factors for two CyberKnife clinical fields and two representative PCSR fields have been measured and calculated by Gago-Arias *et al.* [28]. Two microchambers were investigated: the PTW31014 (13 mm^3) and the Scanditronix-Wellhofer CC13 (130 mm^3). Alinine pellets were used as a reference dosimeter to determine the dose to water. In general, measured correction factors agreed with the Monte Carlo calculations, within the estimated uncertainties.

The first clinical field was a brain treatment; it was composed of 192 subfields, each shaped by the 15 mm collimator. A PCSR field was created to match this clinical field: it employed the same 15 mm collimator to achieve a homogeneous dose in a 32 mm diameter sphere centred in the phantom. Associated uncertainties affecting the last decimals of the following Monte Carlo calculated correction factors are shown in parentheses with two significant figures (coverage factor $k = 2$). The $k^{f_{\text{clin}},f_{\text{msr}}}_{Q_{\text{clin}},Q_{\text{msr}}}$ correction factor for the PTW31014 chamber was 1.038(12), while the $k^{f_{\text{pcsr}},f_{\text{msr}}}_{Q_{\text{pcsr}},Q_{\text{msr}}}$ was equal to 1.006(11). For the CC13 chamber, $k^{f_{\text{clin}},f_{\text{msr}}}_{Q_{\text{clin}},Q_{\text{msr}}} = 1.0041(88)$ and $k^{f_{\text{pcsr}},f_{\text{msr}}}_{Q_{\text{pcsr}},Q_{\text{msr}}} = 1.0024(88)$.

Second, a lung treatment field was studied. This clinical field was composed of 250 subfields; both the 12.5 mm and 20 mm collimators were employed. The PCSR field representing this clinical field delivered a spherically-shaped homogeneous dose distribution with a 48 mm diameter using the same set of collimators. The $k^{f_{\text{clin}},f_{\text{msr}}}_{Q_{\text{clin}},Q_{\text{msr}}}$ correction factors were not calculated for this field, however, the $k^{f_{\text{pcsr}},f_{\text{msr}}}_{Q_{\text{pcsr}},Q_{\text{msr}}}$ was calculated. The measured results

are reported for the former correction factor, and the calculated results for the latter. For the PTW31014 microchamber , $k_{Q_{\text{clin}},Q_{\text{msr}}}^{f_{\text{clin}},f_{\text{msr}}} = 1.008(12)$ and $k_{Q_{\text{pcsr}},Q_{\text{msr}}}^{f_{\text{pcsr}},f_{\text{msr}}} = 0.999(12)$; for the CC13, $k_{Q_{\text{clin}},Q_{\text{msr}}}^{f_{\text{clin}},f_{\text{msr}}} = 1.000(10)$ and $k_{Q_{\text{pcsr}},Q_{\text{msr}}}^{f_{\text{pcsr}},f_{\text{msr}}} = 1.004(10)$.

In Section 1.3.2, it was observed that the main purpose of the PCSR field was to define an intermediate calibration field in which the response of the detector is similar to that inside of any clinical field within its plan-class. The results above do not indicate that there is a correlation between the $k_{Q_{\text{clin}},Q_{\text{msr}}}^{f_{\text{clin}},f_{\text{msr}}}$ for a clinical field and the $k_{Q_{\text{pcsr}},Q_{\text{msr}}}^{f_{\text{pcsr}},f_{\text{msr}}}$ for its associated PCSR field. However, as the authors state, no general conclusions can be drawn, as only two clinical fields (and two PCSR fields) were investigated. Furthermore, each of the clinical and PCSR fields for which correction factors were calculated and measured employed collimators not considered to be small using the criteria established in Section 1.3.1, with the 12.5 mm, 15 mm, and 20 mm collimators used. This limits the applicability of this study, as correction factors in non-small fields are not expected to vary too greatly from unity [29]. Indeed, the $k_{Q_{\text{clin}},Q_{\text{msr}}}^{f_{\text{clin}},f_{\text{msr}}}$ and $k_{Q_{\text{pcsr}},Q_{\text{msr}}}^{f_{\text{pcsr}},f_{\text{msr}}}$ were within 4% of unity for all fields investigated, and most were within 2%. Composite clinical fields employing collimators smaller than this are expected to have larger correction factors, judging from the values seen in small static fields in Section 1.3.3. This necessitates the calculation of correction factors in these fields.

1.4 Thesis Overview

The goal of this study is to calculate the $k_{Q_{\text{clin}},Q_{\text{msr}}}^{f_{\text{clin}},f_{\text{msr}}}$ correction factors for 21 clinical CyberKnife fields employing small collimators. Three detectors are investigated: the A16 microchamber and W1 plastic scintillator by Exradin, both previously described in Section 1.3.3, as well as the Exradin A26 microchamber. The A16 chamber has been chosen as it is a typical detector with which the medical physicist might perform small clinical field dosimetry, and one for which $k_{Q_{\text{clin}},Q_{\text{msr}}}^{f_{\text{clin}},f_{\text{msr}}}$ correction factors have been shown to be required [16, 19, 21, 22, 29–31].

The use of the W1 plastic scintillator as a detector capable of determining the dose to water in small clinical fields with minimal correction factors will be investigated. The

accuracy of the Cerenkov calibration procedure has been verified in static fields, including in the beam penumbra [12], however, this has not yet been done for arbitrary clinical fields. The accuracy of the Cerenkov light effect is therefore ignored in this study. All correction factors reported are calculated under the assumption that the Cerenkov light is adequately removed in small static fields.

Previously, microchambers have not been recommended for use in reference dosimetry, as they cannot meet the specifications for reference dosimeters outlined in the addendum to TG-51 [6]. Despite its design as a microchamber (3.3 mm cavity diameter versus 2.4 mm for the A16), the A26 microchamber has been characterized with respect to these specifications, suggesting that it may exceed requirements [32]. If the $k_{Q_{\text{clin}},Q_{\text{msr}}}^{f_{\text{clin}},f_{\text{msr}}}$ correction factors are small and predictable, this detector may be used in reference as well as small clinical field dosimetry.

A secondary goal of the thesis is to determine the suitability of the PCSR field. This will be done by sorting clinical fields into plan-classes using the specifications established in Section 1.3.2. A PCSR field will be created for each plan-class for which it is suitable according to criteria defined in Section 3.1.2, and the $k_{Q_{\text{clin}},Q_{\text{pcsr}}}^{f_{\text{clin}},f_{\text{pcsr}}}$ correction factors will be calculated for each clinical field within the respective plan-class. If these correction factors are similar to 1, then the chosen PCSR field is a suitable representative of the given plan-class; otherwise, it is not, and another PCSR field must be found. The suitability of the PCSR field will be determined on a class-by-class basis.

The calculation of the correction factors will be done using Monte Carlo methods, by modelling the CyberKnife unit at The Ottawa Hospital Cancer Centre (TOHCC), as well as each of the detectors described above. Chapter 2 describes the methods and results of the beam modelling procedure. In Chapter 3, the methods used to calculate the small clinical field correction factors are described, including the selection of the clinical fields and plan-classes, and the modelling of the phantom, the clinical field delivery, and the detectors. In Chapter 4, the results of the simulations are reported and discussed, including the correction

factors themselves, as well as the suitability of the PCSR field. Finally, conclusions and recommendations for future work are given in Chapter 5.

CHAPTER 2
Beam Modeling

This chapter describes the procedure used to model the CyberKnife beam, and how the model parameters were selected by comparing measurements of the dose distribution data to Monte Carlo calculations of the same data set. In order to provide an accurate model of the photon beam, the BEAMnrc user code [33] of EGSnrc [34, 35] was used to simulate particle transport throughout the CyberKnife linac head, while the `egs_chamber` user code [36] was used to fully model the detector.

2.1 Geometry and Material Definition

The CyberKnife linac head was modelled in detail according to technical drawings provided by the manufacturer. The first components of this model were the electron beam target and mount, followed by an electron filter. The x-rays originating from radiative interactions in the target were then shaped first by the primary collimator, followed by an intermediary block of tungsten called the patient shield, and finally by the interchangeable secondary collimator. The final two components included in the model were the monitor chamber and the mirror.

The composition of each material used throughout this work (including materials in the linac head, the detector, and the phantom) was simulated using PEGS4. A low-energy particle production threshold of `AE`=512 keV and `AP`=1 keV for knock-on electrons and bremsstrahlung photons, respectively, was selected for each material. The density effect correction to the stopping power as a function of charged particle energy, reported in Report No. 37 of the International Comission on Radiation Units and Measurements (ICRU) [37], was used in the simulation of the materials. The EGSnrc distribution includes pre-calculated density effect parameters for a number of materials, tabulated in density effect files. Each

material to be simulated for which a density effect file was available used these density effect parameters. For all other materials, density effect parameters were generated using the National Institue of Standards and Technology (NIST) ESTAR database [38].

2.2 Electron Beam Parameter Estimation

After each component of the linac head was modelled, the physical characteristics (energy and spatial distribution) of the electron beam incident on the target in the BEAMnrc model were tuned so that the modelled electron beam matched the actual beam. The electron beam was assumed to be monoenergetic, with a Gaussian spatial distribution; therefore the parameters of interest were the electron energy and the full width at half maximum (FWHM) of the beam. These parameters were not known *a priori*, since they vary between different CyberKnife units [19, 28]. Therefore it was necessary to estimate the parameters for the unit at TOHCC.

The parameter estimation was done by comparing measurements and calculations of the various dose distribution datasets, namely the PDD, off-axis ratio (OAR), and output factor (OF). These quantities quantify the penetrability of the photon beam in water, the off-axis spread of dose, and the relative dose at a particular reference depth on central axis as a function of the collimator size, respectively. The values of the electron beam parameters have a known influence on these dosimetric quantities [39]. In order to estimate the parameters, these datasets were calculated for several values of the electron beam parameters following the procedure described below, adapted from a number of sources [19,23,28,39,40]. The final values of the electron beam parameters were taken to be those that provided the best match between measurements and calculations of the dose distribution datasets. Calculations were done using the `egs_chamber` [36] user code, by fully modelling the detector and scoring the dose deposited within the active volume.

2.2.1 Energy Estimation

The energy of the electron beam E was the first parameter to be estimated. This was done by comparing measurements and calculations of the PDD for the 60 mm collimator. It

has been shown that the PDD for large fields is relatively insensitive to the spatial distribution of the electron beam [39]. The PDD is, however, sensitive to the electron energy: as the energy increases, the average photon energy in the resulting x-ray beam also increases. The higher energy photon beam has a lower attenuation coefficient, therefore the value of the PDD will increase at depth with a higher photon (and incident electron) energy.

The PDD for the 60 mm collimator was calculated using a varying incident electron beam energy, ranging from 6.5 MeV to 7.0 MeV in steps of 0.1 MeV. Previously reported values of the initial electron energy of the CyberKnife linac of 6.5 MeV [28] and 7.0 MeV [19] indicate that the electron energy of this particular unit should be in this range, despite the CyberKnife having a nominal accelerating potential (NAP) of 6 MV. An initial FWHM of 2.0 mm was used for these calculations, chosen due to its similarity to previously reported values of 2 mm [28] and 2.1 mm [19].

The PDD for the 60 mm collimator was also measured; comparison between calculations and measurements was done based on the deviation between these two as a function of depth. First, both measured and calculated PDD curves were normalized to 100% at a depth of 100 mm [41]. After normalization, the deviation between the measured and calculated PDD curves was computed:

$$\Delta_E^{\mathrm{PDD}}(z) = \mathrm{PDD}^{\mathrm{meas}}(z) - \mathrm{PDD}_E^{\mathrm{calc}}(z) \tag{2.1}$$

Next, for each energy E, a least-squares linear regression was performed on the dose difference as a function of depth. The ideal electron energy would result in a line of zero slope and y-intercept [40].

2.2.2 FWHM Estimation

After the energy of the electron beam, the next parameter to be estimated was the FWHM. The dosimetric datesets that are most sensitive to the FWHM are the OARs [39] and the small field OFs [19]. In particular, the penumbrae of the OARs, and the entire OAR for small fields, are especially sensitive to the FWHM [14, 40]. As the FWHM increases, so too does the dose in the penumbra relative to the dose on central axis, and therefore the

OAR for small fields. Conversely, the small field OFs decrease with increasing FWHM, due to source occlusion effects [14]. As the FWHM increases, the proportion of the photon source that is occluded by the small field collimator increases, thereby decreasing the value of the OF.

For these reasons, and because this beam model was ultimately used to calculate detector-specific correction factors in clinical fields composed of small subfields, the FWHM was tuned by comparing measured and calculated OARs and OFs in small fields. The OARs for the three smallest collimators, 5 mm, 7.5 mm, and 10 mm, were calculated at a depth of $z = 50$ mm in water. These calculations were repeated using a varying incident electron beam FWHM, from 2.0 mm to 3.0 mm in steps of 0.1 mm. This range was selected based on the similar work done by Francescon *et al.* [19], in which the $k_{Q_{\text{clin}},Q_{\text{msr}}}^{f_{\text{clin}},f_{\text{msr}}}$ correction factors for CyberKnife static fields were calculated as a function of the electron beam FWHM.

The electron energy selected using the method presented in Section 2.2.1 was used. The comparison between calculations and measurements for each collimator A was done using the chi-squared (χ^2) metric:

$$\left(\chi^2/df\right) = \frac{1}{df}\sum_{i=1}^{N}\frac{\left(X_i^{\text{meas}} - X_i^{\text{calc}}\right)^2}{\sigma_{X_i^{\text{meas}}}^2 + \sigma_{X_i^{\text{calc}}}^2} \tag{2.2}$$

Here, X_i^{meas} and X_i^{calc} represent measured and calculated values of the same quantity X_i, df represents the number of degrees of freedom (equal to the number of data points N minus the number of constraints), and $\sigma_{X_i^{\text{meas}}}^2 + \sigma_{X_i^{\text{calc}}}^2$ is the variance (square of the uncertainty) of the difference between the measured and calculated quantities. The chi-squared metric therefore determines the goodness of fit of the calculated to the measured quantities relative to the variance between the two.

The chi-squared metric for the OARs becomes:

$$\left(\chi^2/df\right)_{\text{FWHM}}^{\text{OAR}}(A) = \frac{1}{N-1}\sum_{i=1}^{N}\frac{\left(\text{OAR}^{\text{meas}}(r_i, 50\,\text{mm}, A) - \text{OAR}_{\text{FWHM}}^{\text{calc}}(r_i, 50\,\text{mm}, A)\right)^2}{\sigma_{\text{OAR}^{\text{meas}}}^2(r_i, 50\,\text{mm}, A) + \sigma_{\text{OAR}_{\text{FWHM}}^{\text{calc}}}^2(r_i, 50\,\text{mm}, A)} \tag{2.3}$$

where one degree of freedom has been removed by varying the electron beam FWHM. Both $\mathrm{OAR}^{\mathrm{meas}}(r, 50\,\mathrm{mm}, A)$ and $\mathrm{OAR}^{\mathrm{calc}}_{\mathrm{FWHM}}(r, 50\,\mathrm{mm}, A)$ were sampled at N discrete radii r_i.

The small fields OFs were also calculated using the same range of incident electron beam FWHM used for the OARs. The chi-squared metric was used to compare measurements of the OF to calculations:

$$\left(\chi^2/df\right)^{\mathrm{OF}}_{\mathrm{FWHM}} = \frac{1}{3}\sum_{i=1}^{4} \frac{\left(\mathrm{OF}^{\mathrm{meas}}(A_i) - \mathrm{OF}^{\mathrm{calc}}_{\mathrm{FWHM}}(A_i)\right)^2}{\sigma^2_{\mathrm{OF}^{\mathrm{meas}}}(A_i) + \sigma^2_{\mathrm{OF}^{\mathrm{calc}}_{\mathrm{FWHM}}}(A_i)} \tag{2.4}$$

The summation in the above expression is over the small collimators: $\{A_i\}$ ={5 mm, 7.5 mm, 10 mm, and 60 mm}. A degree of freedom has been removed by varying the electron beam FWHM.

The final estimate of the initial electron beam FWHM was the one that yielded the calculated OARs and OFs that had the closest overall agreement with their respective measurements, as evaluated using the chi-squared metric. Ideally, the $\left(\chi^2/df\right)^{\mathrm{OAR}}_{\mathrm{FWHM}}(A)$ for each collimator A and the $\left(\chi^2/df\right)^{\mathrm{OF}}_{\mathrm{FWHM}}$ would be minimized at the same FWHM. In the case of disagreement of the optimal FWHM, a compromise was reached to select the final value.

As an additional verification of the electron beam parameters, the PDD for the 60 mm collimator was recalculated using the final electron beam energy and FWHM, and compared to the measurement. Small field OARs at two additional depths (15 mm and 200 mm) were also calculated and compared to measurements, but were not included in the $\left(\chi^2/df\right)^{\mathrm{OF}}_{\mathrm{FWHM}}$ assessment of the electron beam FWHM.

2.3 Beam Data Measurements

2.3.1 Measurement Setup

All measurements of the CyberKnife beam data were done with the Exradin A16 ionization chamber. This microchamber has a nominal collecting volume of 7 mm^3; the wall and central electrode are composed of C-552 air-equivalent plastic and aluminum, respectively. The chamber was placed in the IBA Blue Phantom^2 scanning water tank, oriented with the

stem perpendicular to the beam central axis along the inline direction. The water tank included a CCU electrometer synchronized with the tank's chamber position tracking system. This allowed for the extraction of PDDs and OARs, as the chamber ionization was tracked as a function of depth and off-axis position.

The IBA FC-65G Farmer-type ionization chamber (nominal volume of 650 mm^3, graphite wall, and aluminum electrode) was used as a reference chamber for these measurements, in order to track and correct for the variation of the linac output as a function of time. This was done for each dosimetric quantity i (i = PDD, OAR, or OF) by dividing the amount of ionization measured by the A16 (M^i_{A16}) by the ionization measured by the reference chamber (M^i_{ref}):

$$M^i = \frac{M^i_{\text{A16}}}{M^i_{\text{ref}}} \tag{2.5}$$

This reference chamber was inserted in a slot in the linac head, just below the primary collimator. Both chambers were connected to the IBA electrometer; the collecting voltage of each chamber was set to −300 V.

The guiding rails of the water tank were leveled so that the field chamber traveled along the axes defined by the tank. The CyberKnife unit was positioned above the tank at an SSD of 800 mm for the PDD and OARs, and an SSD of 785 mm for the OF measurements. For each setup, the mechanical pointer was used to verify the SSD, and the CyberKnife alignment laser was used to verify the vertical alignment of the unit. This laser was directed along the beam central axis, and collimated by a pinhole aperture (1 mm) attached to the 30 mm collimator. The reflection of the laser light from the water surface back onto the collimator was used as a guide for the alignment. The alignment was adjusted until the light was reflected directly to the pinhole aperture. The SSD was verified with the mechanical pointer after this alignment, and adjusted if necessary.

The depth of the A16 chamber as measured by the water tank system was set to 0 mm at a position such that the water surface bisected and ran along the length of the chamber, as described in AAPM's TG-106 Report [42]. As a first approximation, the position of the

chamber in the crossline (x) and inline (y) directions was set to 0 mm when the aforementioned alignment laser shone approximately in the centre of the collecting volume. A more exact position of the radiological centre of the CyberKnife beam was found by measuring OARs for the 5 mm diameter collimator in each direction, at depths of 15 mm and 200 mm. The radiological centre, or the 0 mm position, was defined to be the midpoint of the positive and negative positions of the 50% maximum signal.

2.3.2 PDD Measurement

The PDD for the 60 mm collimator was measured by irradiating the water tank and microchamber setup while varying the depth of the A16 microchamber from 300 mm below the water surface to 10 mm mm above. No shift of the effective point of measurement (EPOM) was considered, since the chamber (including the low-density air cavity) was fully modelled for the calculation.

The normalization at 100 mm depth was done by first fitting the falloff region of the measured PDD (starting at a depth of 30 mm) to a fourth order polynomial. Using this fit, the measured PDD was normalized to 100% at a depth of 100 mm [39]:

$$\mathrm{PDD}^{\mathrm{meas}}(z) = 100\% \cdot \frac{M^{\mathrm{PDD}}(z)}{M_{fit}^{\mathrm{PDD}}(100\,\mathrm{mm})} \tag{2.6}$$

2.3.3 OAR Measurement

Similar to the PDD measurement, the OARs were measured by irradiating the water tank setup while simultaneously varying the (x, y) position of the A16 microchamber. OARs for the three smallest collimators (5 mm, 7.5 mm, and 10 mm) were measured in the x- and y-directions, at three depths each: 15 mm, 50 mm, and 200 mm. These raw data sets were converted into x and y OARs using the following procedure. The x and y OARs for each collimator-depth pair were first centred using small shifts (≤ 0.3 mm) suggested by the IBA software, based on the 50% maximum dose positions of each OAR. The results of this centering process were two OARs for each depth z and collimator diameter A, $M_{\mathrm{cen}}^{\mathrm{OAR}}(x, 0, z, A)$ and $M_{\mathrm{cen}}^{\mathrm{OAR}}(0, y, z, A)$ (x and y refer to the position in the x- and y-directions, respectively).

Next, each x and y OAR was symmetrized by computing the average of $M_{\text{cen}}^{\text{OAR}}$ and its reflection through the origin [23]:

$$M_{\text{sym}}^{\text{OAR}}(x,0,z,A) = \frac{M_{\text{cen}}^{\text{OAR}}(x,0,z,A) + M_{\text{cen}}^{\text{OAR}}(-x,0,z,A)}{2} \tag{2.7a}$$

$$M_{\text{sym}}^{\text{OAR}}(0,y,z,A) = \frac{M_{\text{cen}}^{\text{OAR}}(0,y,z,A) + M_{\text{cen}}^{\text{OAR}}(0,-y,z,A)}{2} \tag{2.7b}$$

Finally, the OARs were normalized to their respective values at the origin:

$$\text{OAR}_{\text{unc}}^{\text{meas}}(x,0,z,A) = \frac{M_{\text{rad}}^{\text{OAR}}(x,0,z,A)}{M_{\text{rad}}^{\text{OAR}}(0,0,z,A)} \tag{2.8a}$$

$$\text{OAR}_{\text{unc}}^{\text{meas}}(0,y,z,A) = \frac{M_{\text{rad}}^{\text{OAR}}(0,y,z,A)}{M_{\text{rad}}^{\text{OAR}}(0,0,z,A)} \tag{2.8b}$$

A plot of the measured OARs (5 mm collimator, 50 mm depth) before and after symmetrization can be found in Figure 2–1.

Upon comparison to Monte Carlo calculations, it was observed that the magnitude of the experimental OARs was larger than the respective calculations, especially in the umbra region (see Figure 2–1). It is hypothesized that during the water tank measurements, scattered radiation from the linac head and water phantom was able to reach the electrometer, which was placed on the patient couch, causing a background signal independent of the actual ionization inside the microchamber. This effect was difficult to detect in most cases, but since the actual dose (and therefore expected ionization) in the umbra is low, the background signal would comprise a significant portion of the total measured ionization. A separate experiment was conducted to correct for this effect, the details of which are described in Section 2.3.5. The subscript "unc" in Equation (2.8) therefore indicates that the OAR has not been corrected for this effect.

2.3.4 OF Measurement

Before the OFs were measured, the vertical position of the CyberKnife unit above the water tank was changed from 800 mm SSD to 785 mm SSD. The SSD and vertical alignment were verified using the mechanical pointer and laser, respectively. The depth of the A16

microchamber was kept fixed at 15 mm below the water surface, so that the source to detector distance (SDD) was 800 mm. All OF measurements were done with the chamber in the centre of the field. The 5 mm, 7.5 mm, 10 mm, and 60 mm collimators were used. A dose of 100 MU was delivered in this setup, a total of three times per collimator.

A Fluke electrometer, model number 35040, was used for the OF measurements instead of the IBA electrometer, because of its thresholding features and minimal leakage currents. Measurements for each collimator were made using a polarizing voltage −300 V. Polarity effects were later corrected for based on P_{pol} measurements performed in solid water; this experiment is further described in Section 2.3.5. The expression for the uncorrected OF for the small field collimator with diameter A is therefore:

$$\text{OF}_{\text{unc}}^{\text{meas}}(A) = \frac{M^{\text{OF}}(A)}{M^{\text{OF}}(60\,\text{mm})} \tag{2.9}$$

2.3.5 Corrections Based on Solid Water Measurements

Two types of corrections were performed in solid water: the first to correct the observed over-response in the umbra region of the OARs (see Section 2.3.3), and the second to correct for the polarity effect in the OF measurements (see Section 2.3.4). The setup for these corrections was identical to the setup of the water tank for the corresponding meaurement, described in Sections 2.3.1, 2.3.3, and 2.3.4. Although the use of solid water phantoms in reference dosimetry is prohibited [6], the differences between solid water and water were deemed to be minimal for the following corrections.

Measurements were performed with the Exradin A16 microchamber and Fluke electrometer, placed outside of the treatment room. The IBA FC-65G was used again as a reference chamber. All measurements are implicitly given relative to the charge collected in this chamber, as described in Section 2.3.1.

OAR Penumbra Correction

The following calculations are based on the assumption that there is a background signal $m(z, A)$ due to head and phantom scatter, independent of the distance along the x-

and y-axes, unrelated to the charge collected in the chamber, and affecting the measured $\mathrm{OAR}^{\mathrm{meas}}_{\mathrm{unc}}(x,0,z,A)$ and $\mathrm{OAR}^{\mathrm{meas}}_{\mathrm{unc}}(0,y,z,A)$ (Equation (2.8)) for all points x and y. A dependence on both z and A is allowed in order to replicate the original measurements conditions.

The background signal may be corrected for using the following procedure. The derivation is done using OARs in the x-direction; the OARs in the y-direction were corrected using a similar method. Let $M_c^{\mathrm{OAR}}(x,0,z,A)$ denote the true charge collected in the chamber at position $(x,0)$, depth z, and for the collimator with diameter A, and let $\mathrm{OAR}^{\mathrm{meas}}(x,0,z,A)$ denote the true OAR. The measured uncorrected charge $M^{\mathrm{OAR}}_{\mathrm{unc}}(x,0,z,A)$ is equal to the sum of the true charge and the background signal $m(z,A)$:

$$M^{\mathrm{OAR}}(x,0,z,A) = M_c^{\mathrm{OAR}}(x,0,z,A) + m(z,A) \tag{2.10}$$

Then the following relations are obtained, from Equations (2.8) and (2.10):

$$\mathrm{OAR}^{\mathrm{meas}}_{\mathrm{unc}}(x,0,z,A) = \frac{M_c^{\mathrm{OAR}}(x,0,z,A) + m(z,A)}{M_c^{\mathrm{OAR}}(0,0,z,A) + m(z,A)} \tag{2.11a}$$

$$\mathrm{OAR}^{\mathrm{meas}}(x,0,z,A) = \frac{M_c^{\mathrm{OAR}}(x,0,z,A)}{M_c^{\mathrm{OAR}}(0,0,z,A)} \tag{2.11b}$$

Dividing Equation (2.11a) by $M_c^{\mathrm{OAR}}(0,0,z,A)$ and inserting Equation (2.11b) yields:

$$\mathrm{OAR}^{\mathrm{meas}}_{\mathrm{unc}}(x,0,z,A) = \frac{\mathrm{OAR}^{\mathrm{meas}}(x,0,z,A) + \frac{m(z,A)}{M_c^{\mathrm{OAR}}(0,0,z,A)}}{1 + \frac{m(z,A)}{M_c^{\mathrm{OAR}}(0,0,z,A)}} \tag{2.12}$$

Finally, performing algebraic manipulations on the resulting equation gives the relation between the uncorrected and corrected OARs:

$$\mathrm{OAR}^{\mathrm{meas}}(x,0,z,A) = \mathrm{OAR}^{\mathrm{meas}}_{\mathrm{unc}}(x,0,z,A)\left(1 + \frac{m(z,A)}{M_c^{\mathrm{OAR}}(0,0,z,A)}\right) - \frac{m(z,A)}{M_c^{\mathrm{OAR}}(0,0,z,A)} \tag{2.13}$$

The ratio $\frac{m(z,A)}{M_c^{\mathrm{OAR}}(0,0,z,A)}$ can be found by measuring the uncorrected and corrected OARs at a particular position $(x_{\mathrm{s}},0)$. The following expressions follow from evaluating Equation (2.13)

at this sample point and performing manipulations on Equation (2.13):

$$\frac{m(z,A)}{M_c^{\mathrm{OAR}}(0,0,z,A)}\left(1-\mathrm{OAR}_{\mathrm{unc}}^{\mathrm{meas}}(x_{\mathrm{s}},0,z,A)\right)=\mathrm{OAR}_{\mathrm{unc}}^{\mathrm{meas}}(x_{\mathrm{s}},0,z,A)-\mathrm{OAR}^{\mathrm{meas}}(x_{\mathrm{s}},0,z,A) \tag{2.14a}$$

$$\frac{m(z,A)}{M_c^{\mathrm{OAR}}(0,0,z,A)}=\frac{\mathrm{OAR}_{\mathrm{unc}}^{\mathrm{meas}}(x_{\mathrm{s}},0,z,A)-\mathrm{OAR}^{\mathrm{meas}}(x_{\mathrm{s}},0,z,A)}{1-\mathrm{OAR}_{\mathrm{unc}}^{\mathrm{meas}}(x_{\mathrm{s}},0,z,A)} \tag{2.14b}$$

The uncorrected $\mathrm{OAR}_{\mathrm{unc}}^{\mathrm{meas}}(x_{\mathrm{s}},0,z,A)$ is taken from the OAR measurements performed in water, described in Section 2.3.3. The corrected $\mathrm{OAR}^{\mathrm{meas}}(x_{\mathrm{s}},0,z,A)$ was measured in the solid water setup using a Fluke electrometer, for each depth and collimator listed in Section 2.3.3. This electrometer was situated outside of the treatment room, and therefore unaffected by phantom and head scatter. First, charge was collected by the A16 in the centre of the field, at $(x,y)=(0,0)$. Then, the chamber was moved to a position along the x-axis with $x_{\mathrm{s}}=10\,\mathrm{mm}$, in the umbra of the field; the $\mathrm{OAR}^{\mathrm{meas}}(x_{\mathrm{s}},0,z,A)$ is equal to the ratio between the charges collected at this sample position and the origin.

The corrected and uncorrected measurements of the OAR were inserted into Equation (2.14b) in order to retrieve the background signal ratio $\frac{m(z,A)}{M_c^{\mathrm{OAR}}(0,0,z,A)}$ for each depth and collimator. This ratio was used in Equation (2.13) to correct for the observed large umbra signal due to the background signal $m(z,A)$. The corrected OARs are shown compared to the Monte Carlo calculations in Section 2.5.2.

The background signal $m(z,A)$ is shown in Figure 2–2. In addition to the small field collimators, this quantity was calculated for the 60 mm collimator in order to correct for the background signal in the measured PDDs; a sample position of $x_{\mathrm{s}}=42\,\mathrm{mm}$ was used for this collimator. For comparison, the total uncorrected signal for the 5 mm collimator OARs at 50 mm depth was equal to 15.7 pC on central axis, and 0.7 pC in the umbra, at 10 mm away from central axis in the x-direction (charge integration time of 1 s per point); thus $m(z,A)$ represents a significant proportion of the measured signal in the umbra. The background signal was calculated by multiplying the background signal ratio $\frac{m(z,A)}{M_c^{\mathrm{OAR}}(0,0,z,A)}$

by the central corrected charge $M_c^{\mathrm{OAR}}(0,0,z,A)$. The latter quantity was determined by dividing Equation (2.10) by $(1+\frac{m(z,A)}{M_c^{\mathrm{OAR}}(0,0,z,A)})$:

$$M_c^{\mathrm{OAR}}(0,0,z,A) = M_{\mathrm{unc}}^{\mathrm{OAR}}(x,0,z,A)\cdot\frac{1}{1+\frac{m(z,A)}{M_c^{\mathrm{OAR}}(0,0,z,A)}} \tag{2.15}$$

Therefore the background signal can be calculated using the known background signal ratio:

$$m(z,A) = M_{\mathrm{unc}}^{\mathrm{OAR}}(x,0,z,A)\cdot\frac{\frac{m(z,A)}{M_c^{\mathrm{OAR}}(0,0,z,A)}}{1+\frac{m(z,A)}{M_c^{\mathrm{OAR}}(0,0,z,A)}} \tag{2.16}$$

The error bars in Figure 2–2 indicate the uncertainty of $m(z,A)$, which was estimated using the rules of error propagation.

No trend in the depth z or the collimator diameter A is apparent, due to the high uncertainties in the background signal; indeed, $m(z,A)$ is mostly constant within the estimated uncertainties, except for the 60 mm collimator. These high uncertainties arise from the error magnification of the subtracted terms present in the numerator of the ratio $\frac{m(z,A)}{M_c^{\mathrm{OAR}}(0,0,z,A)}$ (see Equation (2.14b)).

OF Polarity Correction

Polarity effects in the OF measurements were corrected for using the P_{pol} correction factor, described in AAPM's TG-51 Report [5]. The measurement setup in Section 2.3.4 was replicated using solid water. Charge was collected in this setup using both positive and negative voltages for each collimator; an absolute voltage of 300 V was maintained in both cases. The polarity correction was measured for each collimator, including the 60 mm. It is equal to the average of the two ionizations $M_{\pm 300\,\mathrm{V}}^{\mathrm{OF}}(A)$ measured using opposite polarities, divided by the ionization at negative polarity (the polarity used in the water measurements in Section 2.3.4):

$$P_{\mathrm{pol}}(A) = \frac{M_{300\,\mathrm{V}}^{\mathrm{OF}}(A) + M_{-300\,\mathrm{V}}^{\mathrm{OF}}(A)}{M_{-300\,\mathrm{V}}^{\mathrm{OF}}(A)} \tag{2.17}$$

This correction factor is multiplied into the chamber readings measured in water in Section 2.3.4. Therefore multiplying the numerator and denominator of Equation (2.9) yields

the following expression for the corrected output factor:

$$\mathrm{OF}^{\mathrm{meas}}(A) = \frac{M^{\mathrm{OF}}_{-300\,\mathrm{V}}(A) P_{\mathrm{pol}}(A)}{M^{\mathrm{OF}}_{-300\,\mathrm{V}}(60\,\mathrm{mm}) P_{\mathrm{pol}}(60\,\mathrm{mm})} \tag{2.18}$$

2.4 Monte Carlo Calculations

2.4.1 BEAMnrc Settings

The BEAMnrc linac model was compiled as a shared library: any particle reaching the phase space scoring plane was input into `egs_chamber`, instead of being stored in a phase space file. Low-energy particle transport thresholds of `ECUT`=512 keV and `PCUT`=10 keV for charged particles and photons, respectively, were used throughout the BEAMnrc simulation. The EGSnrc particle transport settings were set to the BEAMnrc default values. The initial electron and FWHM were varied as described in Sections 2.2.1 and 2.2.2.

Variance Reduction

The efficiency ϵ of a particular Monte Carlo calculation can be calculated using the time t required to calculate a quantity with a statistical uncertainty σ:

$$\epsilon = \frac{1}{\sigma^2 t} \tag{2.19}$$

There are many variance reduction techniques available in BEAMnrc that, by decreasing t, σ, or both, increase the overall efficiency of the simulation.

A number of variance reduction techniques were employed in order to improve the efficiency of the linac portion of the simulation. Bremsstrahlung cross-section enhancement (BCSE) was activated in the target material; a BCSE factor of 20 was used, as recommended for the particular simulation type [43]. This variance reduction technique improves efficiency by increasing the probability of bremsstrahlung interactions in the target material by a user-defined BCSE factor f_{BCSE}. In order to avoid altering the physics of the simulation, two extra steps are performed: first, the weight (or relative importance) of any bremsstrahlung photon generated in the target material is reduced by $1/f_{\mathrm{BCSE}}$. Second, the energy of the

charged particle that gave rise to the photon is decremented by the energy of the new particle with probability $1/f_{\mathrm{BCSE}}$.

Efficiency was further improved using the directional bremsstrahlung splitting (DBS) technique [44]. This technique requires the definition of two parameters: a splitting field size FS, and a splitting number NBRSPL. The details of the DBS algorithm are complex, however this variance reduction technique generally results in a large number of low-weight photons within the splitting field, and a low number of high-weight photons outside this field. FS is usually chosen to include the entire field size of interest. Therefore little time is spent tracking photons which do not contribute to the field of interest.

The radius of the splitting field FS depended on the collimator diameter; for each collimator, this field extended 50 mm past the edge of the nominal field radius. The splitting number NBRSPL was optimized for the 5 mm and 60 mm collimators using the method proposed by Ali and Rogers [43]; the splitting numbers for the remaining collimators were interpolated between these two values. The splitting number and splitting field radius used for each collimator can be found in Table 2–1.

Table 2–1: Directional bremsstrahlung splitting parameters for the collimators used throughout the beam modelling procedure. FS (field size) refers to the radius of the splitting field. NBRSPL refers to the bremsstrahlung splitting number.

Collimator diameter (mm)	FS(mm)	NBRSPL
5	52.5	4000
7.5	53.75	3800
10	55	3600
60	80	1100

2.4.2 `egs_chamber` Settings

The `egs_chamber` user code was used to calculate each dose distribution dataset that was measured: the PDD for the 60 mm collimator, and the OARs and output factors for the three smallest collimators. Each quantity was simulated using the identical setup in which the corresponding measurement was acquired, with a single exception. The simulation of

the OARs was only performed in the x-direction: a large asymmetry was observed in the simulated y-direction OARs, as seen in Figure 2–1b.

This asymmetry is likely due to a discrepancy in the position of the effective point of measurement of the microchamber in the stem direction (the y-direction), that is, an asymmetry in the detector geometry with respect to the radiaiton field in this direction for the experimental setup used. A shift of $-0.13\,\text{mm}$ in the calculated y-direction OARS, estimated using the 50% maximum dose positions, largely rectifies this discrepancy, as shown in Figure 2–1d.

This shift is not necessary in the x-direction, as the microchamber has a well-defined centre in this direction: along the electrode axis. Therefore only this direction was considered in the OAR calculations, in order to minimize the amount of corrections required. Calculated and measured x-direction OARs were compared directly, and the y-direction was ignored.

The setup for these measurements is described in Section 2.3. The dosimetric quantities were calculated with varying electron energy and FWHM, as described in Sections 2.2.1 and 2.2.2.

A full model of the A16 microchamber was created in `egs_chamber`, including the stem, central electrode, wall, and air cavity/active volume. This detailed model allowed for the direct comparison between measurements and calculations without the application of perturbative correction factors [19,23]. This chamber model was inserted into a water phantom, with dimensions $300 \times 300 \times 500\,\text{mm}^3$, where the longer dimension in the depth direction was required in order to maintain the photon and charged particle backscatter present in the measurements. The BEAMnrc linac model was used as a particle source for the `egs_chamber` simulation. Low-energy particle transport thresholds of `ECUT`=512 keV and `PCUT`=10 keV for charged particles and photons, respectively, were used throughout the `egs_chamber` simulations. The EGSnrc particle transport settings were set to the `egs_chamber` default values.

Variance Reduction and Dose Calculation

Every variance reduction technique available in `egs_chamber` was employed to improve the efficiency of the calculation of the dosimetric quantities. The intermediate phase-space storage (IPSS) technique [36, 45] allowed for the efficient calculation of PDD curves and OARs. In each case, the IPSS volume was embedded in the water tank, and was large enough to enclose every possible position of the A16 microchamber. In the first part of the particle shower, particle transport occurs throughout the water tank until particles reach the IPSS volume, where the state of each particle and the state of the random number generator (RNG) is stored. In the second part of the shower, particle transport is performed in every geometry describing different chamber positions, and dose is calculated in the scoring region. The use of this technique ensures that the water tank portion of the shower only occurs once, which can significantly reduce the simulation time.

Correlated sampling (CS) was used in conjunction with IPSS, in order to automatically and more efficiently calculate dose ratios [36, 46, 47]. This is done by using the same initial state of the RNG when simulating the two geometries representing the numerator and denominator of the dose ratio in order to maximize correlations between these two. For the PDD curves, the desired ratio was the dose at a depth of z, divided by the dose at a depth of 100 mm:

$$\mathrm{PDD}_E^{\mathrm{calc}}(z) = 100\% \cdot \frac{D^{\mathrm{PDD}}(z)}{D^{\mathrm{PDD}}(100\,\mathrm{mm})} \tag{2.20}$$

Here, D^i represents the dose in cGy, per electron incident on the target in the linac head, that is absorbed in the chamber active volume, for the dosimetric quantity i (i =PDD, OAR, or OF).

Similarly for the OARs, the quantity of interest was the ratio between the absorbed dose at radius r from the beam central axis, divided by the dose with the chamber in the centre:

$$\mathrm{OAR}_{\mathrm{FWHM}}^{\mathrm{calc}}(r, z, A) = \frac{D^{\mathrm{OAR}}(r, z, A)}{D^{\mathrm{OAR}}(0\,\mathrm{mm}, z, A)} \tag{2.21}$$

OARs were calculated for several depths z and collimator diameters A, in order to replicate the measured set of data described in Section 2.3.3.

Neither the IPSS nor the CS techniques were used for the OF simulations, as these require the calculation of dose to detector only at a single point for a given collimator. The OF is defined by the ratio of the absorbed dose on beam central axis using the collimator of diameter A, divided by the dose using the 60 mm diameter collimator:

$$\mathrm{OF}^{\mathrm{calc}}_{\mathrm{FWHM}}(A) = \frac{D^{\mathrm{OF}}(A)}{D^{\mathrm{OF}}(60\,\mathrm{mm})} \tag{2.22}$$

The photon cross-section enhancement (XCSE) technique was employed in every `egs_chamber` simulation, including simulations of the PDD, OARs, and OFs. Using this variance reduction technique, the probability of photon interactions within a user-defined XCSE region is increased by the XCSE factor f_{XCSE} [36]. The weight of charged particles resulting from these interactions is reduced by $1/f_{\mathrm{XCSE}}$; in addition, the weight of charged particles originating from outside the XCSE region that cross inside the volume is also reduced by the same factor. The XCSE region is usually chosen to surround the dose scoring volume. This technique results in a large number of low-weight charged particles that are generated near and can deposit dose inside the scoring volume, thereby decreasing the uncertainty of the scored dose.

In the first part of the PDD and OAR particle showers, an XCSE shell of 10 mm thickness was defined around the IPSS volume. Once the second part of the shower began, XCSE shells of the same thickness were defined at each chamber position, around the wall surrounding the chamber active volume. For the OF simulations, a single XCSE shell of thickness 10 mm was defined surrounding the chamber active volume. This shell thickness was chosen based on the beam quality of the CyberKnife photon beam [36]. The XCSE factor f_{XCSE} was selected for each dosimetric quantity individually, chosen to optimize the efficiency of the particular simulation. The PDD and OF simulations used $f_{\mathrm{XCSE}} = 128$, while the OAR simulations used a factor of 64.

The final variance reduction technique used in the `egs_chamber` simulations was range-based Russian Roulette (RR) [36, 48]. Low-weight charged particles that have sufficiently low energy that they are unable to reach an RR volume, usually chosen to be the detector active volume, are subjected to an RR game with a user-defined survival probability of $1/N_r,\ N_r > 1$. Charged particles surviving RR have their weight increased by a factor of N_r. This greatly reduces the number of charged particles that are far enough from the scoring volume that they could not deposit energy within the latter, while still allowing for the production of photons, via bremsstrahlung and annihilation interactions, that could reach the scoring volume.

For the PDD and OARs, the first RR volume was the IPSS volume; any charged particle not able to reach this region was subjected to RR. After reaching the IPSS volume, the RR volume was changed to include only the active volume of the detector at each chamber position. For the OF simulations, a single RR volume comprising the active volume of the chamber was used. A Russian Roulette parameter of $N_r = 512$ was used for each simulation, chosen in order to optimize efficiency.

2.5 Results

2.5.1 Energy Estimation

Figure 2–3 shows the slopes and intercepts of the lines of best fit of the difference between the measured and calculated PDDs for different electron energies E. The slopes, intercepts, and uncertainties were computed using weighted linear least squares regression, with the weight of each point given by the reciprocal of the variance of the difference between the measured and calculated PDDs:

$$\sigma^2_{\Delta^{\mathrm{PDD}}_E}(z) = \sigma^2_{\mathrm{PDD}^{\mathrm{meas}}}(z) + \sigma^2_{\mathrm{PDD}^{\mathrm{calc}}_E}(z) \tag{2.23}$$

The uncertainty of the calculated PDDs was given by the statistical uncertainty of the Monte Carlo calculations (type A). The uncertainty of the measured PDDs was given by a combination of contributions due to statistical and detector positionining uncertainties

(type A and B, respectively). The statistical uncertainty was estimated by assuming a Poisson distribution ($\sigma_{M^i} \propto \sqrt{(M^i)}$), and fitting the measured relative standard deviations calculated from the measurements discussed in Section 2.3.5. This amounted to a relation between the relative uncertainty and the measured charge M_i:

$$\frac{\sigma_{M^i}}{M^i} = \frac{0.0067}{\sqrt{M^i/\mathrm{pC}}} \tag{2.24}$$

This uncertainty in the measured charge was propagated through Equation (2.6), yielding the statistical uncertainty in the PDD:

$$\sigma_{\mathrm{PDD}^{\mathrm{meas}},\mathrm{stat}}(z) = 100\% \cdot \frac{\sigma_{M^{\mathrm{PDD}}(z)}}{M^{\mathrm{PDD}}_{\mathrm{fit}}(100\,\mathrm{mm})} \tag{2.25}$$

The uncertainty of the measured PDDs due to detector positioning uncertainty was estimated by computing the maximum deviation of the PDD with respect to the value at each point by moving in the positive and negative direction by an amount σ_z, the uncertainty of the detector position in the z-direction. σ_z was taken to be equal to 0.2 mm for the IBA Blue Phantom^2 scanning water tank. Therefore the positioning uncertainty in the PDD is:

$$\sigma_{\mathrm{PDD}^{\mathrm{meas}},\mathrm{pos}}(z) = \max\left\{\left|\mathrm{PDD}^{\mathrm{meas}}(z) - \mathrm{PDD}^{\mathrm{meas}}(z-\sigma_z)\right|, \left|\mathrm{PDD}^{\mathrm{meas}}(z) - \mathrm{PDD}^{\mathrm{meas}}(z+\sigma_z)\right|\right\} \tag{2.26}$$

The combination of these two uncertainties is given by their summation in quadrature:

$$\sigma_{\mathrm{PDD}^{\mathrm{meas}}}(z) = \sqrt{\sigma^2_{\mathrm{PDD}^{\mathrm{meas}},\mathrm{stat}}(z) + \sigma^2_{\mathrm{PDD}^{\mathrm{meas}},\mathrm{pos}}(z)} \tag{2.27}$$

Lines of best fit were calculated for the slope and y-intercept as a function of E (solid lines in Figure 2–3), also calculated using weighted linear least squares regression. The slope and y-intercept of the difference between the measured and calculated PDDs for electron energy $E = 7\,\mathrm{MeV}$ do not follow the same linear trend as do the rest of the data; the dashed lines in Figure 2–3 therefore indicate lines of best fit for the data excluding the points at this energy. The following is analysed using these lines of best fit. The x-intercept, denoting the optimal energy, was determined to be equal to 6.8(5) MeV for the slope graph, and 7(1) MeV

for the intercept graph, where the values in parentheses denotes the uncertainty in the last digit of the energy. Both of these values are in agreement with one another. The final estimate of $E = 6.7\,\text{MeV}$ was chosen due to the fact that the value of the y-intercept of the line of best fit of the differences at 6.7 MeV is closer to 0 than it is for the 6.8 MeV electron energy: $-0.363\,\%$ versus $-0.410\,\%$.

Figure 2–4 shows the direct comparison between the PDD measured with the A16 microchamber and the PDD calculated using the final initial electron energy of 6.7 MeV, both normalized to 100% at a depth of 100 mm. The measured PDD has been corrected to eliminate the presence of an estimated 0.54 pC background signal (see Figure 2–2) using similar methods as described in Section 2.3.5. The error bars for the measured and calculated values indicate the combined uncertainty in the value of the measured PDD and the estimated statistical uncertainty for the corresponding calculated values, respectively. As indicated in Section 2.2.2, this PDD was calculated using the FWHM obtained in Section 2.5.2. Agreement between measurement and calculation is good except in the buildup region. Similar agreement was found for the initially selected FWHM of 2.0 mm, demonstrating that the change in FWHM does not affect the calculated PDD for the 60 mm collimator.

2.5.2 FWHM Estimation

The spatial distribution of the electron beam was estimated to have a FWHM of 2.5 mm. Using this FWHM when calculating small field OARs and OFs gave the best overall agreement when compared to their respective measurements, as seen in Figure 2–5a. The 5 mm OAR chi-squared metric is minimized for larger values of the FWHM, however, $(\chi^2/df)^{\text{OF}}_{\text{FWHM}}$ increases past FWHM = 2.6 mm, suggesting that a smaller value is more suitable. $(\chi^2/df)^{\text{OAR}}_{\text{FWHM}}\,(7.5\,\text{mm})$ is minimized at FWHM = 2.5 mm, and the chi-squared metric for the other OARs and for the OFs are near their minimum values at this point. Therefore a compromise was reached by selecting 2.5 mm as the value of the electron beam FWHM.

Figures 2–6 to 2–9 show the direct comparison between the small field OARs and OFs measured with the A16 microchamber and the respective simulations, calculated using the

initial electron energy and FWHM of 6.7 MeV and 2.5 mm, respectively. The background signal $m(z, A)$ in the measured OARs has been corrected, as described in Section 2.3.5. As indicated in Section 2.2.2, OARs for several depths are shown.

The error bars on the measured and calculated OARs include statistical and detector positioning uncertainties, calculated using a similar method as was used for the PDDs in Section 2.5.1. In addition to these uncertainties, the error bars on the OFs include the combined uncertainty due to detector modeling and the underlying photon cross-sections, summarized in Table 2–2. The latter two are presently only available for OFs, not for PDDs and OARs. Good agreement within uncertainties between measurements and calculations is observed for each OAR and OF using these initial electron beam parameters. These results, together with the comparison between the measured and calculated PDD shown in Figure 2–4, demonstrate that the current beam model, when used to simulate detector response in small fields, is an adequate representation of the actual CyberKnife beam for this study.

It should be noted that while a totally accurate beam model is desirable, it is not strictly necessary, since in this study, the beam model was not used to calculate quantities that were directly compared to measured quantities. Nevertheless, a realistic model is required in order to draw clinically relevant conclusions.

Table 2–2: Type A and B uncertainties for the measured and calculated small field OFs. Uncertainties due to detector modelling, as well as to detector positioning in the measurements, were estimated by Francescon *et al.* [21], while uncertainties due to the underlying photon cross sections were estimated by Muir *et al.* [10].

	Type A	Type B		
	Statistical	Combined detector modelling and cross-section	Detector positioning	Total
Measurement	<0.21%		<0.50%	<0.54%
Calculation	<0.18%	<0.56%		<0.59%

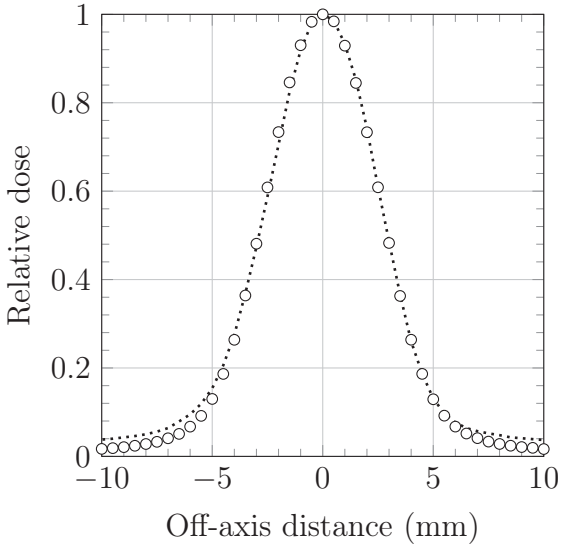

(a) x-direction. Measured: not symmetrized; calculated: not shifted.

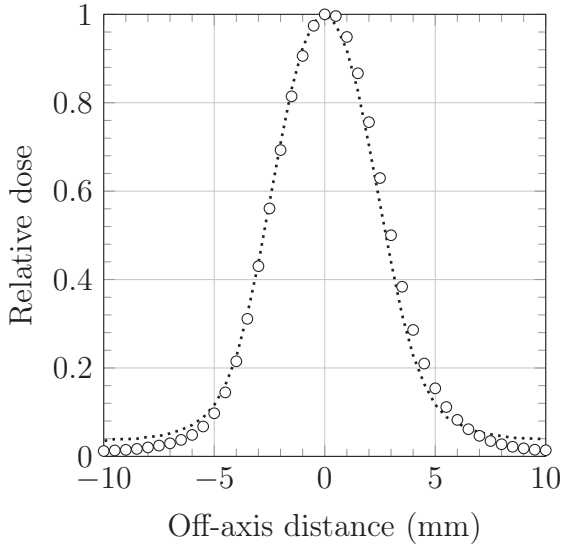

(b) y-direction. Measured: not symmetrized; calculated: not shifted.

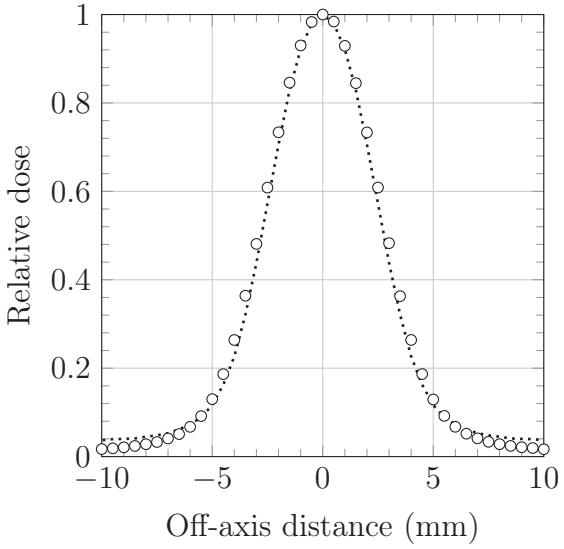

(c) x-direction. Measured: symmetrized; calculated: not shifted.

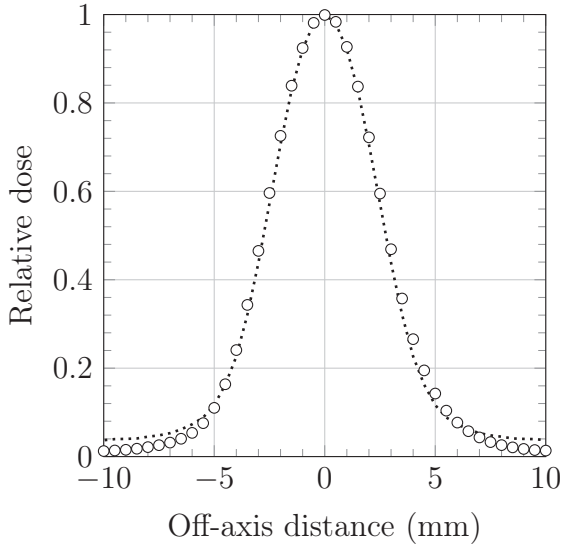

(d) y-direction. Measured: symmetrized; calculated: shifted -0.13 mm.

Figure 2–1: Measured (dots) and calculated (circles) OARs in the x- and y-directions (5 mm collimator, 50 mm depth), before and after required symmetrizations (measured x and y) and shift (calculated y). The measured OARS are significantly greater than the calculated values in the umbra due to a background signal.

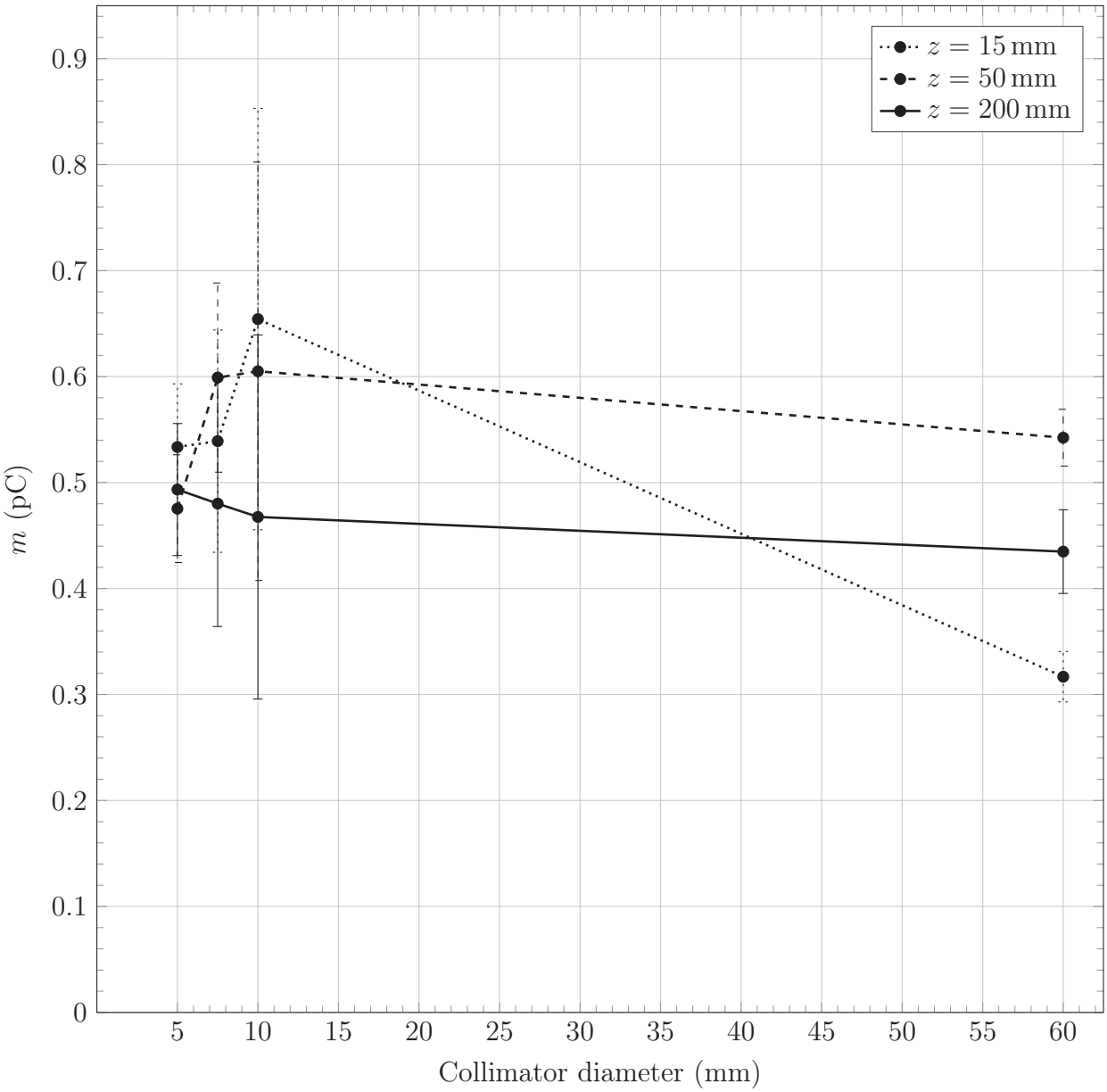

Figure 2–2: The extracted background signal $m(z, A)$ in the measured OARs, hypothesized to have been caused by head and phantom scatter in the electrometer. The charge integration time for each measurement point is 1 s.

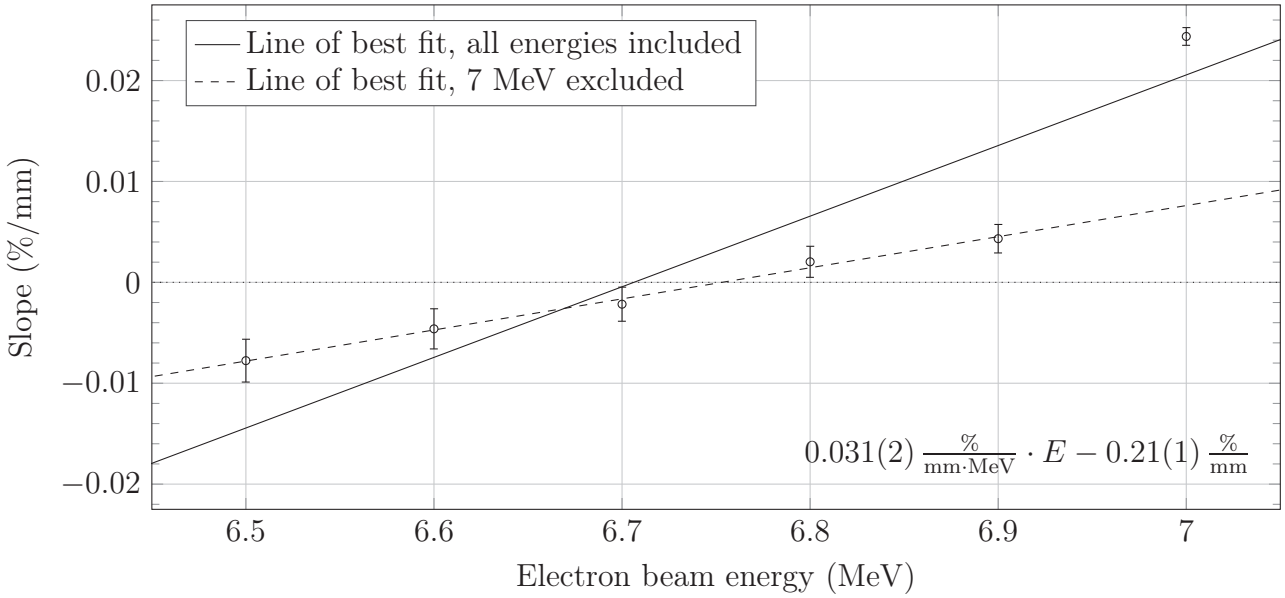

(a) Slope of the line of best fit against initial electron energy E.

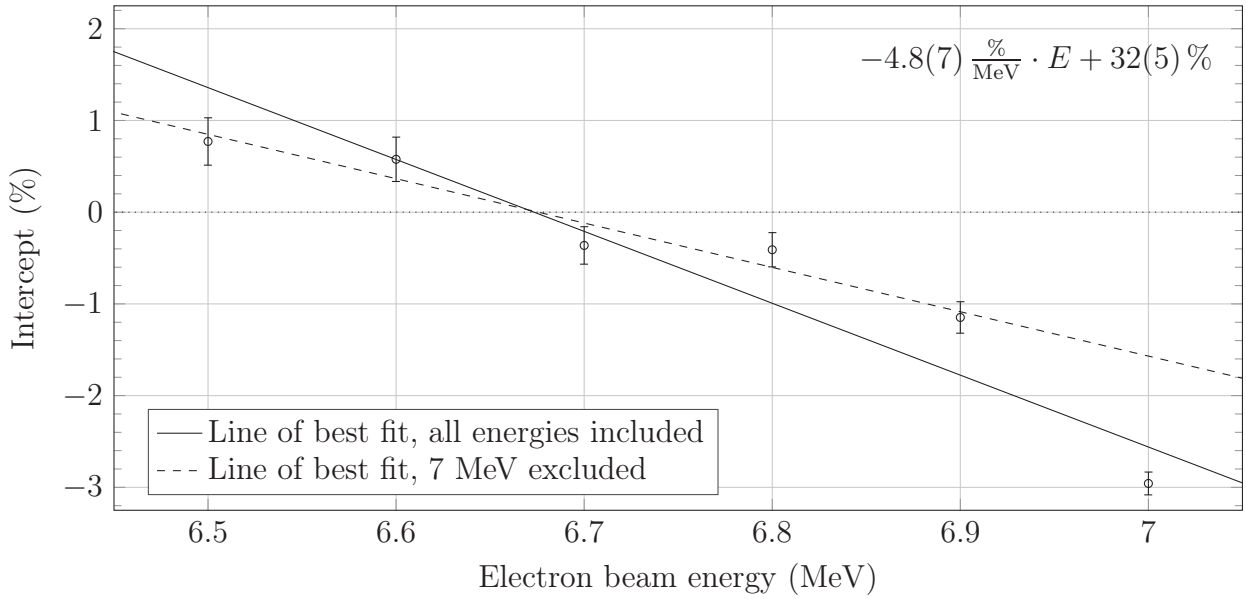

(b) y-intercept of the line of best fit against initial electron energy E.

Figure 2–3: The line of best fit for the difference between the measured and calculated PDDs for the 60 mm collimator, as a function of depth z, was used to determine the optimal electron energy E. Lines of best fit are calculated for the slope and y-intercept as a function of E, in order to determine the energy at which these parameters are equal to 0. The equations for the lines excluding the 7 MeV energy points (dashed lines) are inscribed in the corresponding figure; the value in parentheses denotes the uncertainty in the last digit of the slope or intercept.

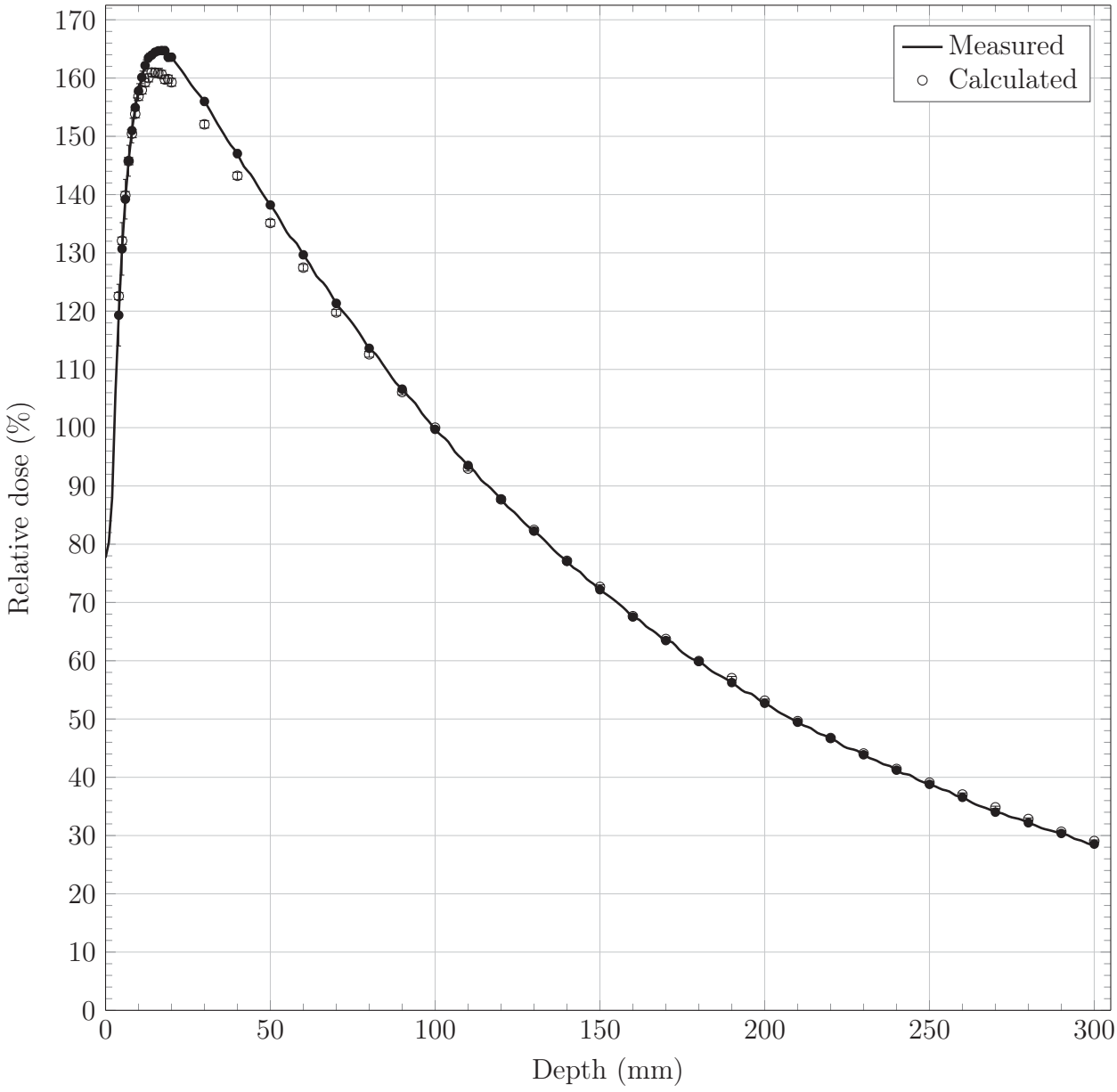

Figure 2–4: Comparison between the PDD for the 60 mm collimator measured using the A16 microchamber, and the corresponding simulation, calculated using the electron beam parameters determined in Sections 2.5.1 and 2.5.2: $E = 6.7\,\text{MeV}$ and FWHM $= 2.5\,\text{mm}$. The error bars for the measured and calculated values are approximately the same size as the circles.

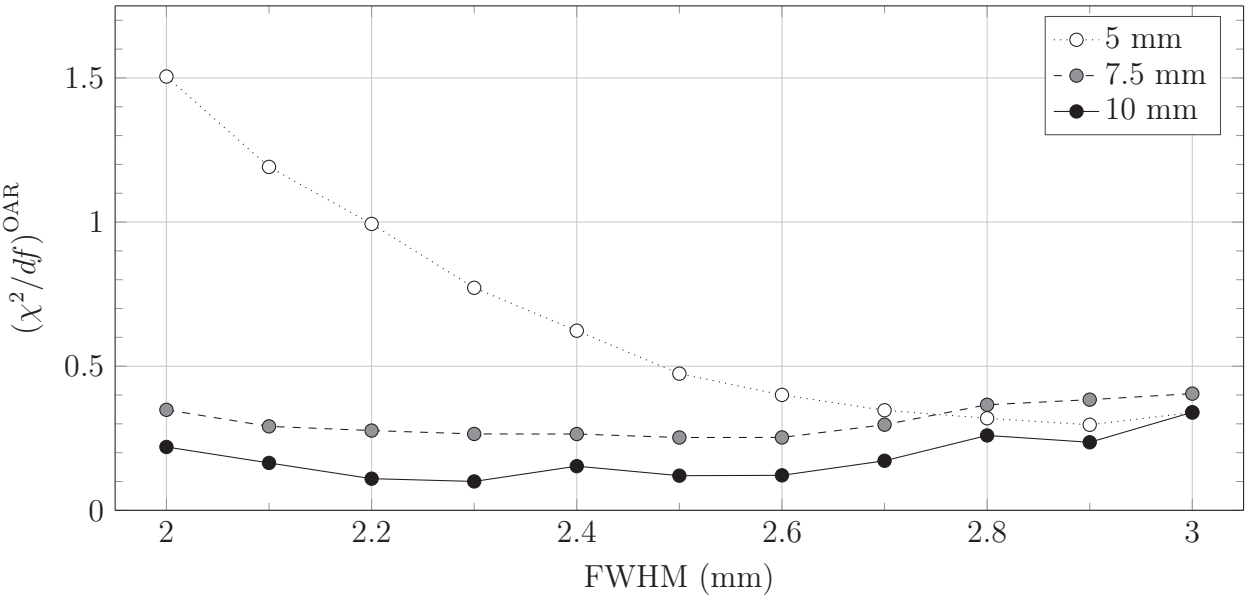

(a) The OAR chi-squared metric.

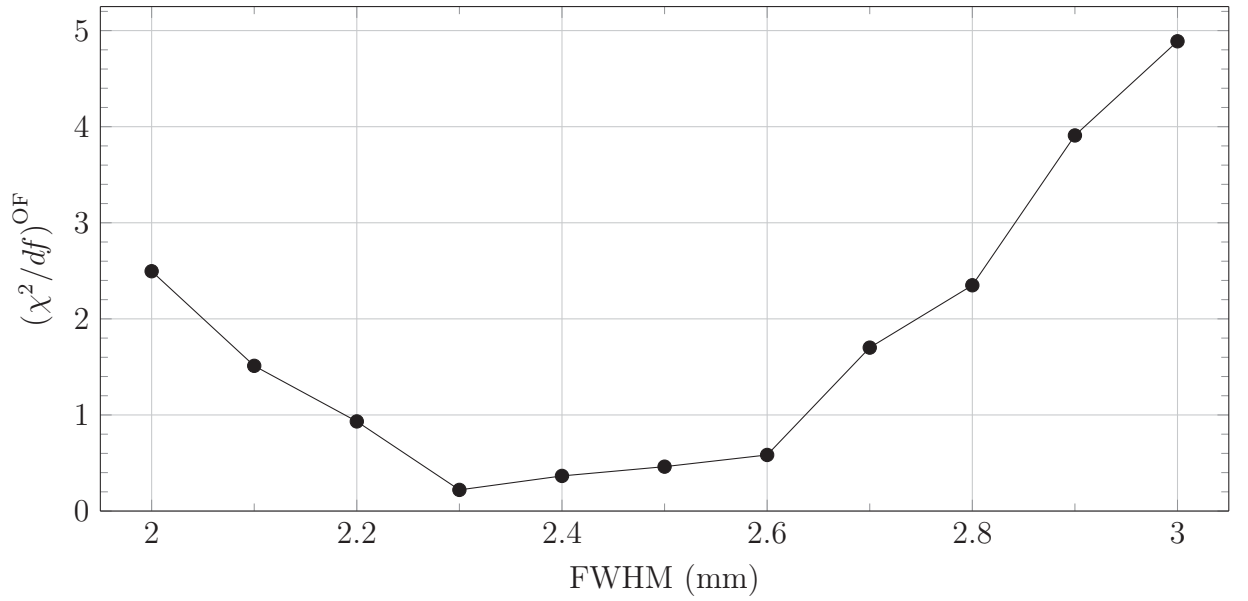

(b) The OF chi-squared metric.

Figure 2–5: The chi-squared metric, measuring the goodness of fit of the calculated to the measured small field OARs and OFs, was used to determine the optimal electron beam FWHM. The value which minimized $(\chi^2)/df$ for the OFs and each OAR was chosen as the final FWHM.

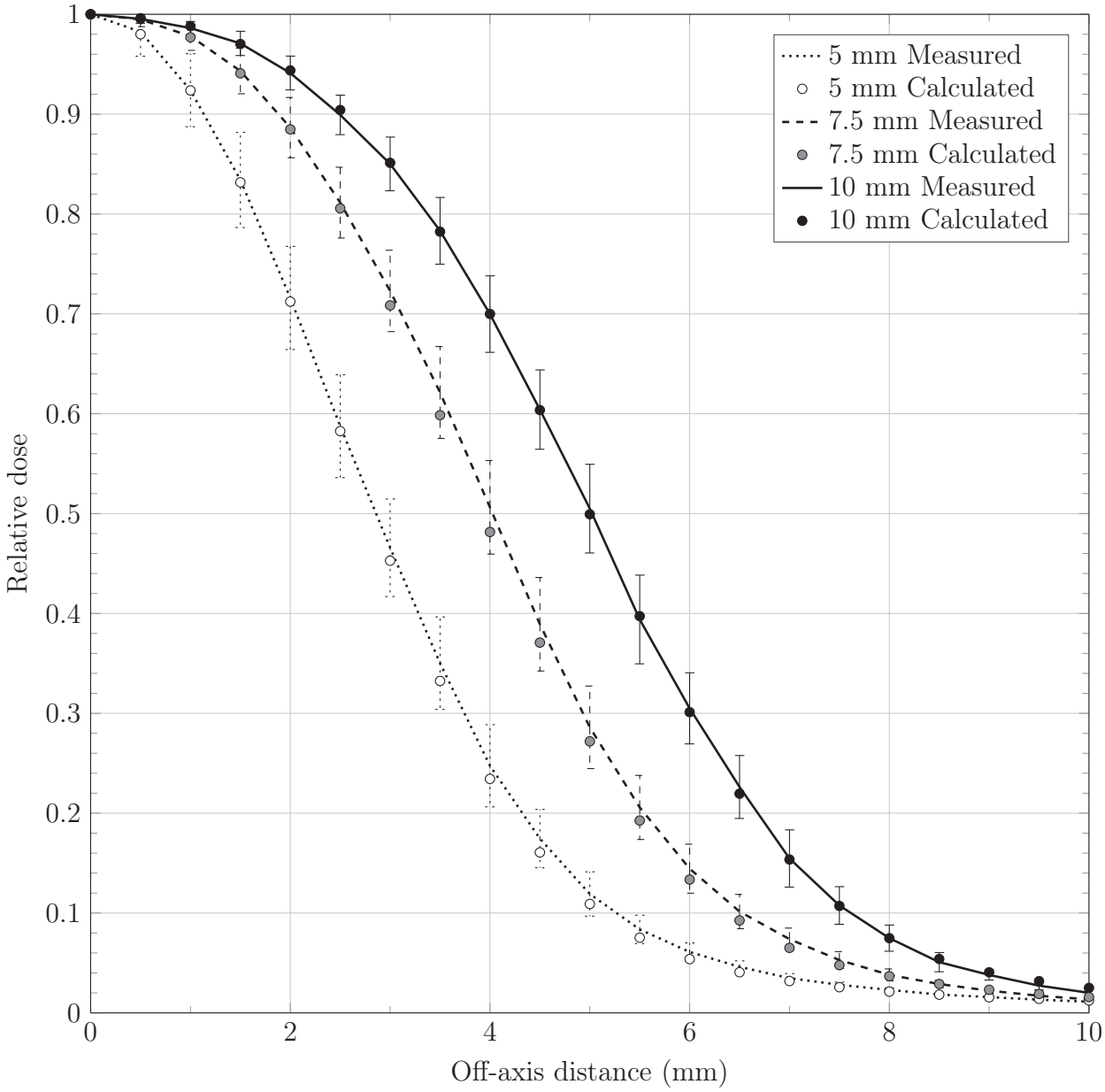

Figure 2–6: Comparison between small field OARs at a depth of 15 mm, measured using the A16 microchamber, and the corresponding simulations, calculated using the electron beam parameters determined in Sections 2.5.1 and 2.5.2: $E = 6.7\,\text{MeV}$ and FWHM $= 2.5\,\text{mm}$. The error bars for the calculated values are approximately the same size as the circles.

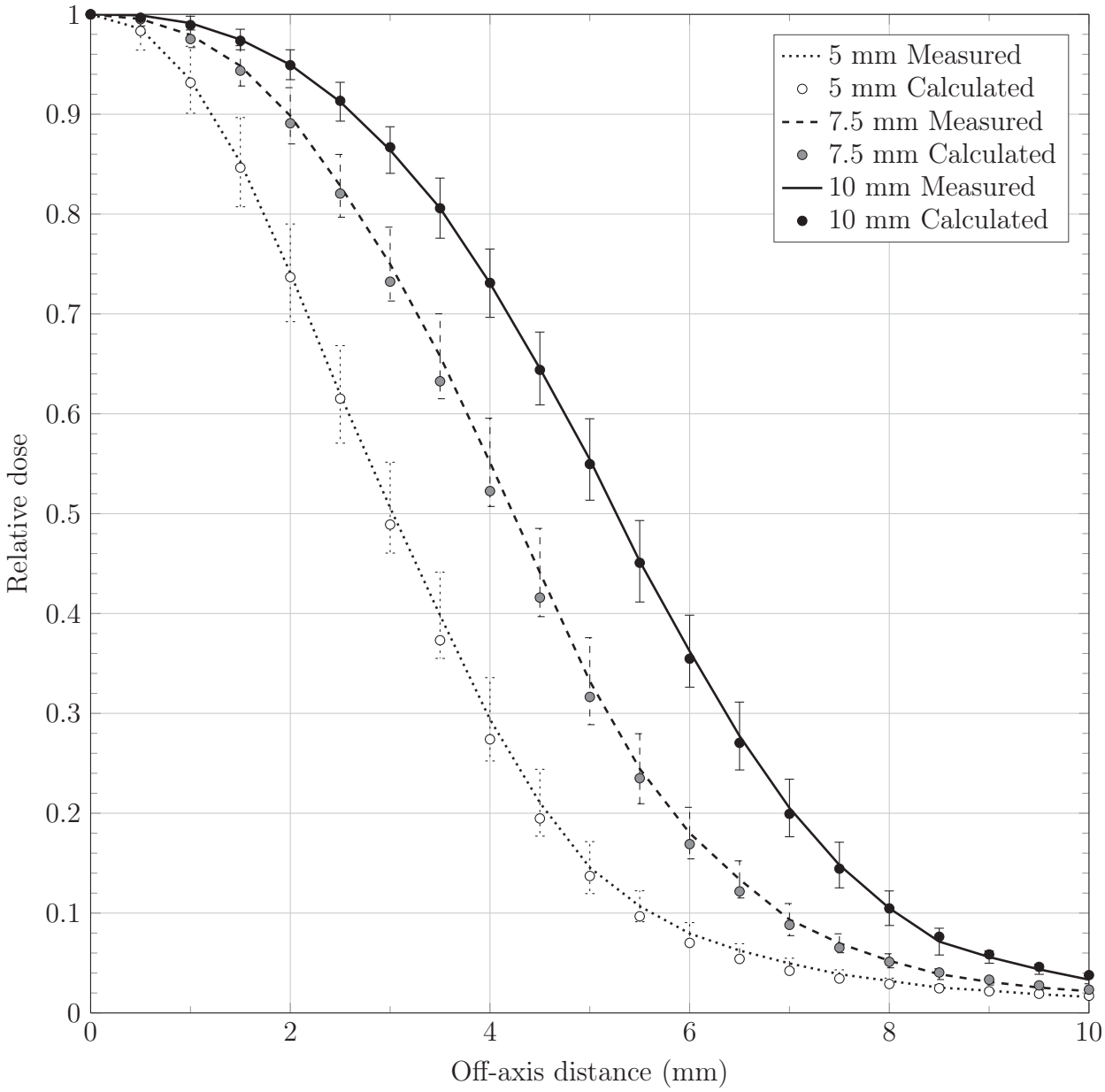

Figure 2–7: Comparison between small field OARs at a depth of 50 mm, measured using the A16 microchamber, and the corresponding simulations, calculated using the electron beam parameters determined in Sections 2.5.1 and 2.5.2: $E = 6.7\,\text{MeV}$ and FWHM $= 2.5\,\text{mm}$. The error bars for the calculated values are approximately the same size as the circles.

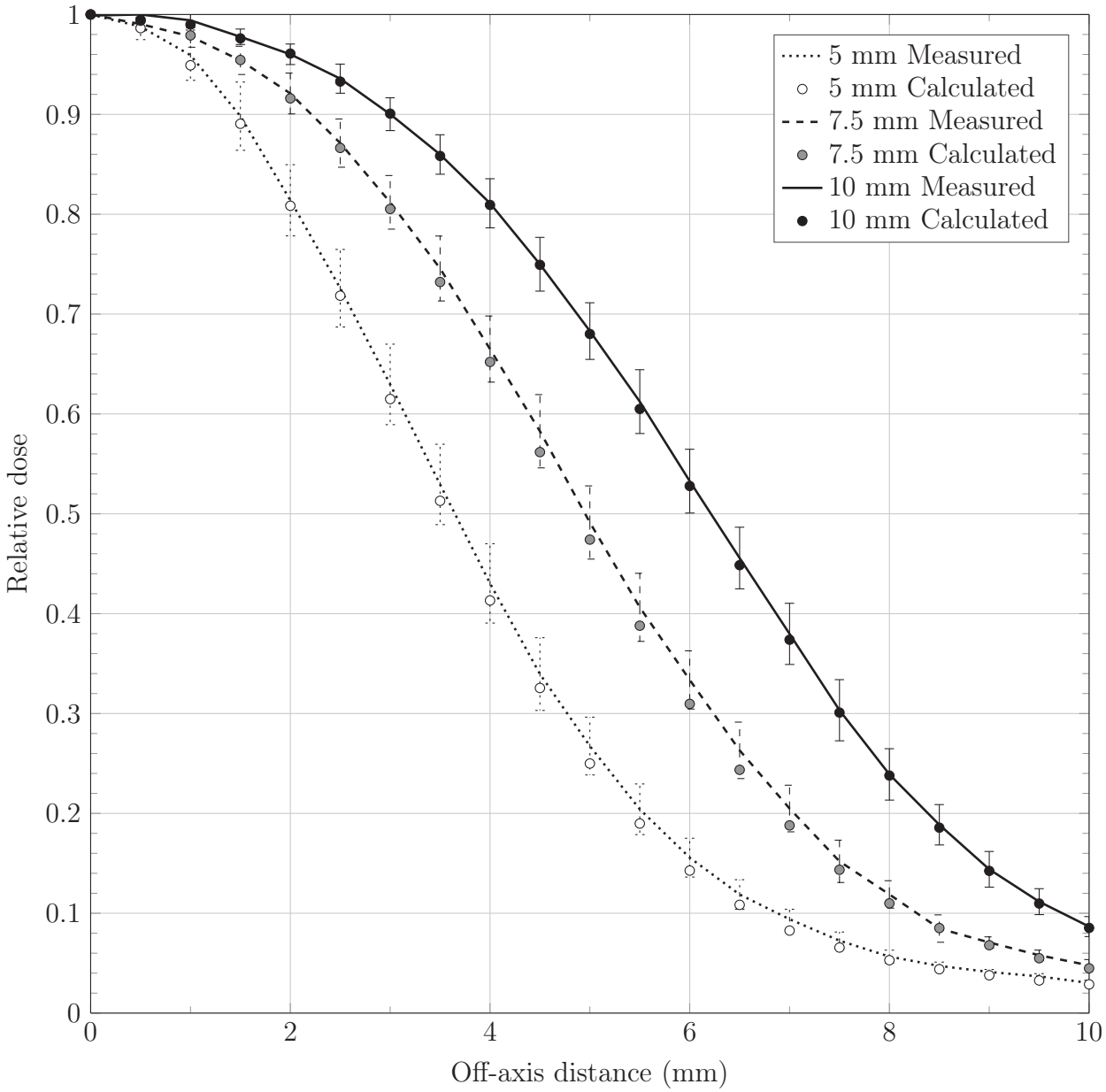

Figure 2–8: Comparison between small field OARs at a depth of 200 mm, measured using the A16 microchamber, and the corresponding simulations, calculated using the electron beam parameters determined in Sections 2.5.1 and 2.5.2: $E = 6.7\,\text{MeV}$ and FWHM $= 2.5\,\text{mm}$. The error bars for the calculated values are approximately the same size as the circles.

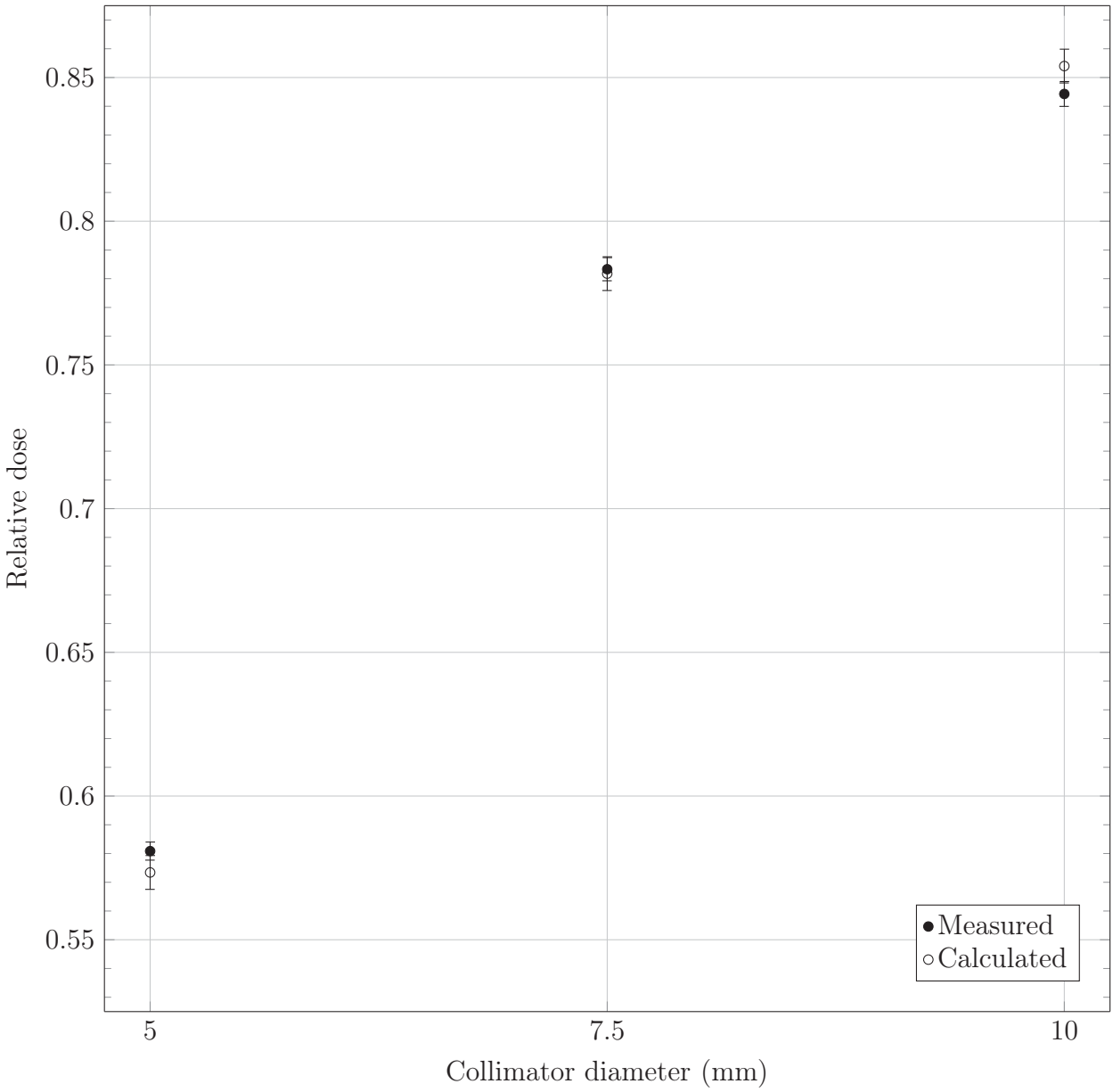

Figure 2–9: Comparison between small field OFs, measured using the A16 microchamber, and the corresponding simulations, calculated using the electron beam parameters determined in Sections 2.5.1 and 2.5.2: $E = 6.7\,\text{MeV}$ and $\text{FWHM} = 2.5\,\text{mm}$.

CHAPTER 3
Calculation of Clinical Field Correction Factors: Methods

Using the model of the CyberKnife linac described and validated in Chapter 2, detector-specific correction factors were calculated for a number of clinical fields. This chapter describes the selection of the investigated clinical fields and plan-classes, as well as the methods used to model the detectors and the composite field delivery for the CyberKnife system.

3.1 Field Selection

As described in Section 1.3.2, the clinical fields were split into plan-classes, grouped according to common pre-identifiable characteristics. Three clinical fields within each plan-class were selected from the CyberKnife plan database at TOHCC. It should be emphasized that these clinical fields were not designed with the present study in mind. Instead, the fields were planned according to standard protocols carried out by the CyberKnife team at TOHCC and were used for actual patient treatments.

3.1.1 Clinical Plan Classes Investigated

The characteristics defining each plan-class are shown in Table 3–1. Both the isocentric (I) and non-isocentric (N) delivery types were investigated. The vast majority of small clinical fields delivered isocentrically at TOHCC were also planned using the skull beam path; very few use the trigeminal neuralgia or body paths. For this reason, isocentric plan-classes used the skull beam path exclusively. Both the trigeminal neuralgia and the skull paths are frequently used in non-isocentric type clinical fields at TOHCC; the body path is typically not used for the purposes of small field delivery.

In addition to the delivery type and beam path, the plan-classes were further subdivided by considering which collimator(s) was used to define the clinical field. Only fields utilizing one or two collimators size were considered. Furthermore, only the three smallest collimators

were used throughout the clinical plans investigated: the 5 mm, 7.5 mm, and 10 mm diameter collimators.

Clinical fields within the isocentric plan-classes (IS1-IS3) are generally used to treat spherical metastases. The size of the collimator is chosen to provide optimal target coverage. Clinical fields within plan-classes NT1 and NT2 are generally used to treat patients with trigeminal neuralgia, a non-malignant neural disease. The use of the smallest two collimators, combined with the non-isocentric delivery and the trigeminal neuralgia path, allows for the coverage of smaller, oblong shaped targets. Finally, clinical fields within plan-class NS1 are generally used to treat acoustic neuromas.

Certain non-isocentric clinical fields, especially those using multiple collimators, can yield irregularly shaped dose distributions in the patient, in which the centre of the target receives less dose than the periphery. This is possible because the targets of the beams comprising the field are randomly distributed on the surface of the target instead of constrained to point at the centre, causing a subset of the beams to intersect at the periphery of the target. Each clinical field in plan-class NS1 was of the type that produced this irregular dose distribution. The clinical fields in plan-classes NT1 and NT2, as well as the isocentric clinical plan-classes IS1, IS2, and IS3, yield dose distributions in which the centre of the target receives a larger dose than the periphery.

Table 3–1: The six clinical plan-classes investigated. Each plan-class is named according to the characteristics defining the clinical fields within that class. The first letter stands for Isocentric or Non-isocentric delivery. The second letter stands for the Skull or Trigeminal neuralgia beam path. The integer following the two letters further distinguishes the plan-classes, according to the collimator size that is used.

Plan class name	Delivery type	Beam path	Collimator diameter(s) (mm)
IS1	Isocentric	Skull	5
IS2	Isocentric	Skull	7.5
IS3	Isocentric	Skull	10
NT1	Non-isocentric	Trigeminal neuralgia	5
NT2	Non-isocentric	Trigeminal neuralgia	5 & 7.5
NS1	Non-isocentric	Skull	5 & 7.5

3.1.2 The PCSR Fields

A PCSR field was created for each plan-class for which the variation of the calculated $k_{Q_{\text{clin}},Q_{\text{msr}}}^{f_{\text{clin}},f_{\text{msr}}}$ for the clinical fields in the plan-class was less than a certain amount. A variation of less than 1% was considered to be ideal, with a maximum variation of 2% tolerated. These figures were selected by considering that the component of the uncertainty in the determination of the dose to water in small composite clinical fields related to the omission of the $k_{Q_{\text{clin}},Q_{\text{pcsr}}}^{f_{\text{clin}},f_{\text{pcsr}}}$ (see Section 1.3.2) should only make up a fraction of the total uncertainty of approximately 2-4% recommended in the AAPM reports for dosimetric accuracy in IMRT [49] and for robotic radiosurgery [50].

The PCSR field was designed to have similar characteristics to the clinical fields within the plan-class that it represented. These characteristics included the delivery type (isocentric or non-isocentric), beam path (trigeminal neuralgia or skull), and the set of collimators used to define the field. The strategy for the creation of the PCSR field for each plan-class was to keep the field as simple as possible, while still maintaining the requirements needed to represent the class.

For the isocentric plan-classes, every beam available for the particular path represented was employed, each beam having equal weight (i.e., MU) to another. This can be compared to the typical clinical isocentric field, in which certain beams have been removed, and the beam weights have been optimized to improve target coverage and to avoid OARs. The requirement that the PCSR field provide a uniform dose over a volume extending over the dimensions of the detector, defined in Section 1.3.2, was not able to be fulfilled in these fields, as the beam central axes meet at a common point in the phantom, leading to a high-dose gradient region. In order to meet this specification using small fields in CyberKnife, a non-isocentric field must be used, in which beam penumbrae overlap, creating a low-dose gradient region. Such a PCSR field, however, would no longer be representative of isocentric clinical fields, therefore the requirement of dose uniformity was relaxed. The definition of

the PCSR field is more complex for non-isocentric plan-classes; this is discussed further in Section 4.2.

3.1.3 The MSR Field

As indicated in Section 1.3.2, the clinical field correction factors for the CyberKnife system are defined relative to a suitable MSR field. The MSR field for the CyberKnife unit was taken to be the 60 mm collimator [13]; the detectors were placed at a depth in water of 50 mm and at an SDD of 800 mm [21].

3.2 Monte Carlo Simulation

The `egs_chamber` user code was used to calculate the detector-specific correction factors for each clinical field investigated. In order to calculate these correction factors, the following must be modelled:

- the CyberKnife linac and small field collimators;
- the phantom in which clinical fields are delivered;
- the delivery of each clinical field; and
- the detectors to be investigated, including intermediate volumes.

The CyberKnife linac and small field collimators have been modelled and validated in BEAMnrc, as described in Chapter 2. This linac was compiled as a shared library and used as a particle source in `egs_chamber`, as indicated in Section 2.4.1. The remaining items are be described below.

3.2.1 Phantom Modeling

Clinical field measurements for the CyberKnife unit at TOHCC are typically performed in a custom solid water phantom, named the "Bullet". The name is taken after its shape, which was designed to approximate a head: a hemisphere attached to a cylinder of the same radius. The Bullet phantom features swappable inserts, each machined for a different detector; the inserts are designed in such a way as to place the centroid of each detector in the centre of the hemisphere, where it meets the cylinder. The phantom also splits apart in the coronal plane, revealing a slot where as many as four radiochromic films can be inserted.

Using the swappable inserts and the film slot, almost any dosimeter can be used inside the Bullet phantom.

Although solid water comprises the bulk of the material used in the Bullet, there are some metallic and other plastic components used. A total of 7 cylindrical fiducials composed of platinum are implanted in the top and bottom parts of the phantom, which are used in the CyberKnife fiducial tracking algorithm to align the phantom within the treatment room. The film slot features 3 stainless steel pin pricks, meant to pierce holes in precise locations in the corners of the film stack. These holes are later identified on the image of the film, and are coregistered to the corresponding locations on a computed tomography (CT) image of the Bullet. The two halves of the phantom are held together using locating pins composed of polyoxymethylene. Finally, the round phantom is held securely by a cradle, which is then placed on the treatment couch during field deliver. The cradle is composed of poly(methyl methacralate) (PMMA).

In order to accurately model the clinical field, the phantom in which measurements are performed must be modelled [13]. Therefore a fully detailed model of the Bullet phantom was constructed in `egs_chamber`. This model included all components described above; the composition of each material was simulated using PEGS4, as described in Section 2.1. A render of the `egs_chamber` model is shown in Figure 3–1.

In addition to the model, a CT image of the Bullet phantom was acquired. This image was needed in order to plan and create the clinical fields. A shifted version of the CT coordinate system was used to define the model in `egs_chamber`. This shift preserved the directions of the (x, y, z) axes, but placed the centroid of the active volume of each detector (and the clinical field phantom) at the origin. The position of the centroid in CT coordinates was estimated using the measuring tools in the CyberKnife treatment planning system (TPS).

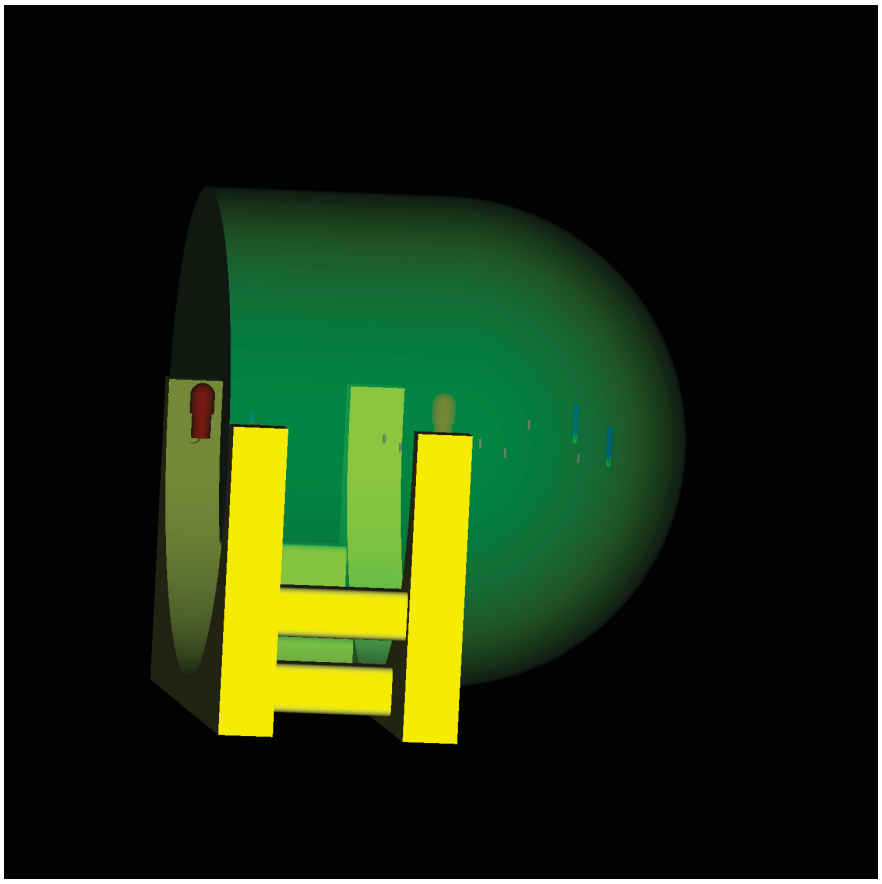

Figure 3–1: Interior view of the `egs_chamber` model of the Bullet phantom. Different colours indicate the materials of each component: green is solid water, yellow is PMMA, red is polyoxymethylene, and the remaining colours are the metal fiducials and pins.

3.2.2 Clinical Field Delivery Modeling

Clinical fields consist of a large number of beams distributed around the patient. The summation of each beam, with its appropriate weight, results in the final clinical field. Each individual beam is specified by the coordinates of the node and target (in patient CT coordinates), the diameter of the collimator that was used to define the beam, and the total MU for the beam. As described in Section 1.1.2, the node position refers to the position of the photon source, while the target position refers to the position of a point typically on the surface of the target towards which the beam is directed. These parameters are stored in a treatment plan Extensible Markup Language (XML) file, which can be used to reconstruct

the clinical field outside of the TPS [51]. The beam information within this XML file was used to model the delivery of each clinical field in `egs_chamber`.

First, the specifications of each beam i were read from the XML file: node and target coordinates ($\vec{n}_i$ and $\vec{t}_i$), collimator diameter (d_i), and MU (MU_i). The base particle source for each beam i was the BEAMnrc source that used the collimator with diameter d_i. In BEAMnrc, particles travel along the $+z$ direction and stop at the phase space scoring plane, at a user-selected node to phase space distance NPD of 600 mm. In the CyberKnife model, the position of the photon source (and therefore node) is the front face of the electron beam target, facing the accelerating waveguide (W. Kilby, private communication). Particles in `egs_chamber` are emitted along the $+z$ direction and begin their transport at the $z = \text{NPD}$ plane.

Therefore in order to bring the base particle source described above to the position and orientation of beam i in the actual clinical field, three transformations are required:

1 translate the base source, so that it has the correct node to target distance;

2 rotate the resulting source, so that particles are emitted in the correct direction relative to the Bullet phantom; and

3 translate the resulting source, so that the target is in the correct position relative to the Bullet phantom.

Each of these transformations is performed within `egs_chamber` using affine source transformations; their implementation is described below. Translations are defined by a vector ($\vec{T_{1,i}}$ or $\vec{T_{2,i}}$ for the first and second translations for beam i), while the rotation is defined by a matrix ($\vec{R}_i$). After every beam i has been transformed from the base particle source to its final position and direction, they are combined into the final clinical field, each beam weighted by MU_i.

Transformation 1: Translation

For transformations 1 and 2, a temporary target is established at the origin; transformation 3 then translates the temporary target to the actual position. Transformation 1, then,

is simply a translation to establish the correct node to target distance for beam i (NTD_i). The NTD_i is calculated as the absolute value of the difference between the node and target position coordinates:

$$\vec{r_i} = \vec{n_i} - \vec{t_i} \tag{3.1a}$$

$$\text{NTD}_i = |\vec{r_i}| \tag{3.1b}$$

In the BEAMnrc simulation the particles have traveled a distance $\text{NPD} = 600\,\text{mm}$ in the $+z$ direction; they originate at the $z = \text{NPD}$ in `egs_chamber`. Therefore the node position of the base particle source is effectively at the origin in `egs_chamber`. This source must be translated in the $-z$ direction, by an amount given by the node to target distance NTD_i. This ensures that particles travel the full NTD_i from the new node to the target at the origin. Therefore the vector defining this translation is:

$$\vec{T_{1,i}} = \begin{bmatrix} 0 \\ 0 \\ -\text{NTD}_i \end{bmatrix} \tag{3.2}$$

Transformation 2: Rotation

The result of transformation 1 is a source emitting particles in the $+z$ direction from a plane at position $\vec{T_{1,i}}$. Transformation 2 combines two rotations into a single step: the composition of both rotations results in a source emitting particles towards the origin, from a plane at position $\vec{r_i}$. First, the source is rotated by an angle θ_i around the x-axis. The matrix defining this rotation is:

$$R_x(\theta_i) = \begin{pmatrix} 1 & 0 & 0 \\ 0 & \cos\theta_i & -\sin\theta_i \\ 0 & \sin\theta_i & \cos\theta_i \end{pmatrix} \tag{3.3}$$

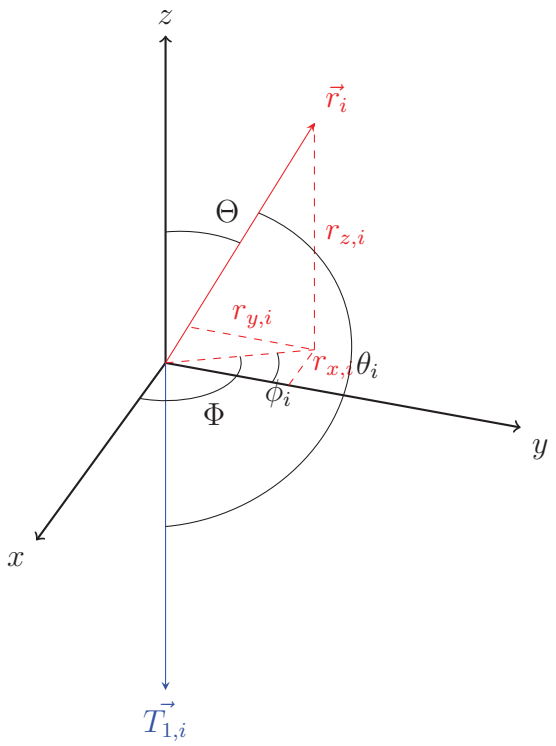

Figure 3–2: Rotation defining transformation 2 for beam number i in the clinical field. The particle source at position $\vec{T}_{1,i}$ (blue) is rotated to the new position at $\vec{r}_i$ (red), first by an angle θ_i around the x-axis, then by an angle ϕ_i around the z-axis.

Next, the resulting source is rotated by an angle ϕ_i around the z-axis. The matrix defining this rotation is:

$$R_z(\phi_i) = \begin{pmatrix} \cos\phi_i & -\sin\phi_i & 0 \\ \sin\phi_i & \cos\phi_i & 0 \\ 0 & 0 & 1 \end{pmatrix} \tag{3.4}$$

The total rotation R_i is defined by the matrix product of the two matrices defining the individual rotations:

$$R_i = R_z(\phi_i)R_x(\theta_i) \tag{3.5a}$$

$$R_i = \begin{pmatrix} \cos\phi_i & -\sin\phi_i\cos\theta_i & \sin\phi_i\sin\theta_i \\ \sin\phi_i & \cos\phi_i\cos\theta_i & -\cos\phi_i\sin\theta_i \\ 0 & \sin\theta_i & \cos\theta_i \end{pmatrix} \tag{3.5b}$$

The angles θ_i and ϕ_i are best understood as modifications of the standard spherical angles Θ and Φ, as seen in Figure 3–2. From this diagram, the following relations are obtained:

$$\Theta = \pi - \theta_i \tag{3.6a}$$

$$\Phi = \phi + \pi/2 \tag{3.6b}$$

In order to compute the rotation matrix R_i defined in Equation (3.5), the sine and cosine of angles θ_i and ϕ_i must be calculated. This can be done by first calculating sine and cosine of Θ and Φ. These quantities are defined in terms of the x, y, z-coordinates of $\vec{r}_i$ ($r_{x,i}$, $r_{y,i}$, $r_{z,i}$) and its vector norm:

$$\cos\Theta = \frac{r_{z,i}}{|\vec{r}_i|} \qquad \sin\Theta = \sqrt{1-\cos^2\Theta} \tag{3.7a}$$

$$\cos\Phi = \frac{r_{x,i}}{r_{x,i}^2 + r_{y,i}^2} \qquad \sin\Phi = \frac{r_{y,i}}{r_{x,i}^2 + r_{y,i}^2} \tag{3.7b}$$

Inserting Equation (3.6) into Equation (3.7) and rearranging terms yields the following expressions for the sine and cosine of angles θ_i and ϕ_i:

$$\cos\theta_i = -\frac{r_{z,i}}{|\vec{r}_i|} \qquad \sin\theta_i = \sqrt{1-\cos^2\Theta} \tag{3.8a}$$

$$\cos\phi_i = \frac{r_{y,i}}{r_{x,i}^2 + r_{y,i}^2} \qquad \sin\phi_i = -\frac{r_{x,i}}{r_{x,i}^2 + r_{y,i}^2} \tag{3.8b}$$

These values are inserted into the rotation matrix R_i defined in Equation (3.5) in order to generate the rotation required to bring beam i to the correct orientation relative to the Bullet phantom.

Transformation 3: Translation

The final transformation required to generate beam i in the clinical field is a translation. After transformations 1 and 2, the beam is pointed at a temporary target positioned at the origin; transformation 3 will translate the beam so that it is pointing to the correct target $\vec{t}_i$. The coordinate system of the `egs_chamber` model of the bullet phantom Bullet

phantom was shifted in order to place the centroid of the detector active volume at the origin. Both centroid position $\vec{c}$ and target position $\vec{t_i}$ are given in CT coordinates. Therefore the translation required in `egs_chamber` is given by the difference between $\vec{t_i}$ and $\vec{c}$:

$$\vec{T_{2,i}} = \vec{t_i} - \vec{c} \tag{3.9}$$

These source transformations were validated by calculating the dose distribution resulting from a 3-beam test field directed onto the Bullet phantom. Each beam was defined using the 5 mm collimator; the positions of the nodes were chosen randomly, while the target positions were each set to lie in the centre of the phantom. The dose distribution was calculated twice: once using the CyberKnife TPS, and again by simulating the test field in `egs_chamber` using the algorithm described above. In each case, no detector was inserted in the Bullet phantom. The transverse, coronal, and sagittal planes at the point of intersection of the beams were extracted from the TPS dose grid. In the `egs_chamber` simulation, dose was scored in $2 \times 2 \times 2\,\mathrm{mm}^3$ cubes corresponding to the voxels comprising each of these three planes. These six two-dimensional dose distributions are shown in Figure 3–3. The path that each beam takes within the phantom is easily seen using these orthogonal views. The similarity of the shapes of the TPS and `egs_chamber` dose distributions implies that the beam orientations and positions have been modeled correctly.

3.2.3 Total Correction Factor Calculation

The clinical field correction factors were calculated for three different detectors: the Exradin A16 and A26 microchambers, and the W1 plastic scintillator. The A16 has been described previously in Section 2.3.1; it has a nominal collecting volume of $7\,\mathrm{mm}^3$, and the wall and central electrode are composed of C-552 air-equivalent plastic and aluminum, respectively. The A26 has a larger collecting volume of $15\,\mathrm{mm}^3$. This microchamber features a guard ring, and the guard ring, central electrode and wall are all composed of C-552 air-equivalent plastic. The W1 is constructed entirely out of plastic materials similar to water. The scintillating fiber has a diameter of 1.0 mm and a length of 3.0 mm; it is composed of

polysterene. The scintillating fibre is enclosed in an acrylonitrile butadiene styrene (ABS) plastic wall, and coupled to a PMMA optical fibre.

Each detector was modelled in `egs_chamber` within the Bullet phantom. As described in Section 3.2.1, the centroid of the active volume of each detector was placed at the origin of the coordinate system; this position coincides with the centre of the plane of intersection of the hemisphere and cylinder of the phantom. A separate geometry was defined, in which a sphere of water with radius 0.3 mm was placed within the solid water phantom; this geometry is necessary in order to calculate the numerators in the $k^{f_{\text{clin}},f_{\text{msr}}}_{Q_{\text{clin}},Q_{\text{msr}}}$ and $k^{f_{\text{pcsr}},f_{\text{msr}}}_{Q_{\text{pcsr}},Q_{\text{msr}}}$ correction factors. The water sphere was also placed at the origin, at the position of the centroid of the detector active volumes. Dose was scored within the active volume of each detector, as well as the water sphere, in order to compute the dose ratio $D^{f_{\text{clin}}}_{w,Q_{\text{clin}}}/D^{f_{\text{clin}}}_{det,Q_{\text{clin}}}$ (or $D^{f_{\text{pcsr}}}_{w,Q_{\text{pcsr}}}/D^{f_{\text{pcsr}}}_{det,Q_{\text{pcsr}}}$ if a PCSR field was simulated) present in the numerator of the $k^{f_{\text{clin}},f_{\text{msr}}}_{Q_{\text{clin}},Q_{\text{msr}}}$ and $k^{f_{\text{pcsr}},f_{\text{msr}}}_{Q_{\text{pcsr}},Q_{\text{msr}}}$ correction factors.

A similar method was used to calculate the denominator of the $k^{f_{\text{clin}},f_{\text{msr}}}_{Q_{\text{clin}},Q_{\text{msr}}}$ and $k^{f_{\text{pcsr}},f_{\text{msr}}}_{Q_{\text{pcsr}},Q_{\text{msr}}}$ correction factors, the $D^{f_{\text{msr}}}_{w,Q_{\text{msr}}}/D^{f_{\text{msr}}}_{det,Q_{\text{msr}}}$ ratio. Each detector was modelled in the 60 mm MSR field described in Section 3.1.3; the 0.3 mm radius water sphere was again placed at the position of the centroid of the detector active volumes. Dose was scored within the active volume of each detector, as well as the water sphere, in order to compute the dose ratio $D^{f_{\text{msr}}}_{w,Q_{\text{msr}}}/D^{f_{\text{msr}}}_{det,Q_{\text{msr}}}$ present in the denominator of the $k^{f_{\text{clin}},f_{\text{msr}}}_{Q_{\text{clin}},Q_{\text{msr}}}$ and $k^{f_{\text{pcsr}},f_{\text{msr}}}_{Q_{\text{pcsr}},Q_{\text{msr}}}$ correction factors.

3.2.4 Intermediate Correction Factor Calculation

The correction factor $k^{f_{\text{clin}},f_{\text{msr}}}_{Q_{\text{clin}},Q_{\text{msr}}}$ is specific to the detector, as well as the clinical field under investigation. Each non-water detector component perturbs the photon and charged particle fluence, contributing separately to the total correction factor. The method described in Section 3.2.3 is used to calculate $k^{f_{\text{clin}},f_{\text{msr}}}_{Q_{\text{clin}},Q_{\text{msr}}}$ and $k^{f_{\text{pcsr}},f_{\text{msr}}}_{Q_{\text{pcsr}},Q_{\text{msr}}}$, which is used to correct for the overall detector response in the clinical/PCSR field relative to the MSR field. However, this method cannot be used to determine the magnitude of the perturbation that each component

contributes to the total correction factor. Instead, this can be accomplished by calculating a chain of intermediate correction factors, each one accounting for the influence of a different detector component.

This chain of intermediate correction factors is calculated by defining a series of geometries, starting with the fully modelled detector, and ending with a 0.3 mm radius sphere of water placed at the centroid of the active volume. This size was chosen to emulate the work done by Papaconstadopoulos *et al.* [23]; minimal volume averaging is expected over a sphere of such a small radius. Dose is scored within the active volume of the detector for each of these geometries, except for the sphere of water, where dose is only scored within the sphere. This results in a series of cavity doses, defined by Bouchard *et al.* [8]:

- D_{det}: dose in the active volume of the fully modelled detector;
- $D_{\text{cel,wall}}$: dose in the active volume of the detector without the stem (not applicable for the W1 plastic scintillator);
- D_{wall}: dose in the active volume of the detector without the stem and central electrode;
- D_{act}: dose in the bare active volume (no stem, central electrode, or wall);
- D_{vapor}: dose in the bare active volume filled with water of the same density as the active volume material (1.20479 mg/cm^3 for the ion chambers, and 1.05 g/cm^3 for the W1 plastic scintillator);
- $D_{w,\text{vol}}$: dose in the bare active volume filled with water of the density of water (1 g/cm^3); and
- $D_{w,\text{point}}$: dose in the 0.3 mm radius sphere of water.

Since the W1 plastic scintillator does not have a central electrode, the $D_{\text{cel,wall}}$ volume is not applicable for this detector. These volumes are shown explicitly for the A16 in Figure 3–4. In general, when a component is removed, it is replaced by the material that is surrounding it. In the case of the ion chambers, the central electrode is therefore replaced with air. All other detector components are replaced with the phantom material: either the solid water in the Bullet phantom for the clinical/PCSR fields, or water for the MSR field.

The perturbation factors are calculated according to the following definitions:

$$P_{\text{stem}} = \frac{D_{\text{cel,wall}}}{D_{\text{det}}} \tag{3.10a}$$

$$P_{\text{cel}} = \frac{D_{\text{wall}}}{D_{\text{cel,wall}}} \tag{3.10b}$$

$$P_{\text{wall}} = \frac{D_{\text{act}}}{D_{\text{wall}}} \tag{3.10c}$$

$$\left(\frac{\overline{L}}{\rho}\right)^{w}_{det} P_{\text{fl}} = \frac{D_{\text{vapor}}}{D_{\text{act}}} \tag{3.10d}$$

$$P_{\rho} = \frac{D_{w,\text{vol}}}{D_{\text{vapor}}} \tag{3.10e}$$

$$P_{\text{vol}} = \frac{D_{w,\text{point}}}{D_{w,\text{vol}}} \tag{3.10f}$$

P_{stem}, P_{cel}, and P_{wall} correct for the detector response relative to water due to the perturbations of the stem, central electrode (if applicable), and wall, respectively. After these perturbations are removed, a bare cavity composed of the detector active volume material (air for the A16 and A26, polystyrene for the plastic scintillator) remains embedded in the phantom. $\left(\frac{\overline{L}}{\rho}\right)^{w}_{det} P_{\text{fl}}$ and P_{ρ} correct for the effect of replacing this detector material with water: $\left(\frac{\overline{L}}{\rho}\right)^{w}_{det} P_{\text{fl}}$ deals with the difference in atomic composition between the two materials, while P_{ρ} corrects for the varying density. The final perturbation factor is the volume averaging factor P_{vol}. In high-gradient or non-uniform dose distributions, the dose averaged over the water cavity is not necessarily representative of the dose to water at a mathematical point. The volume averaging perturbation factor approximately corrects for this effect by determining the dose in a small sphere of water with radius 0.3 mm, located at the centroid of the active volume.

These perturbations factors are computed for the three detectors, in each clinical, PCSR, and MSR field. The detector perturbation in the clinical or PCSR field due to each component c is calculated relative to the corresponding perturbation in the MSR field, in order to

obtain the full intermediate correction factor:

$$[P_c]^{f_{\text{clin}},f_{\text{msr}}}_{Q_{\text{clin}},Q_{\text{msr}}} = \frac{P^{f_{\text{clin}}}_{c,Q_{\text{clin}}}}{P^{f_{\text{msr}}}_{c,Q_{\text{msr}}}} \tag{3.11a}$$

$$[P_c]^{f_{\text{pcsr}},f_{\text{msr}}}_{Q_{\text{pcsr}},Q_{\text{msr}}} = \frac{P^{f_{\text{pcsr}}}_{c,Q_{\text{pcsr}}}}{P^{f_{\text{msr}}}_{c,Q_{\text{msr}}}} \tag{3.11b}$$

The product of all of the intermediate correction factors for a clinical or PCSR field yields the total correction factor for that field:

$$k^{f_{\text{clin}},f_{\text{msr}}}_{Q_{\text{clin}},Q_{\text{msr}}} = \left[P_{\text{stem}} P_{\text{cel}} P_{\text{wall}} \left(\frac{\overline{L}}{\rho}\right)^{w}_{det} P_{\text{fl}} P_{\rho} P_{\text{vol}} \right]^{f_{\text{clin}},f_{\text{msr}}}_{Q_{\text{clin}},Q_{\text{msr}}} \tag{3.12a}$$

$$k^{f_{\text{pcsr}},f_{\text{msr}}}_{Q_{\text{pcsr}},Q_{\text{msr}}} = \left[P_{\text{stem}} P_{\text{cel}} P_{\text{wall}} \left(\frac{\overline{L}}{\rho}\right)^{w}_{det} P_{\text{fl}} P_{\rho} P_{\text{vol}} \right]^{f_{\text{pcsr}},f_{\text{msr}}}_{Q_{\text{pcsr}},Q_{\text{msr}}} \tag{3.12b}$$

3.2.5 Detector Position within the Clinical Fields

For static fields, the detector-specific correction factors $k^{f_{\text{clin}},f_{\text{msr}}}_{Q_{\text{clin}},Q_{\text{msr}}}$ depends on the field of interest, as well as the position of the detector within the field (see Section 1.3.3), with the off-axis position having a larger effect on the correction factor than the depth or SDD. Composite clinical fields in CyberKnife consist of many static fields superimposed on one another; therefore in general, the $k^{f_{\text{clin}},f_{\text{msr}}}_{Q_{\text{clin}},Q_{\text{msr}}}$ should depend on detector position for these fields as well. In light of this, a standard procedure must be followed to select the detector position within the clinical fields, so that differences between the $k^{f_{\text{clin}},f_{\text{msr}}}_{Q_{\text{clin}},Q_{\text{msr}}}$ for different fields are not due to detector placement, but to the field properties.

In measurements of CyberKnife clinical fields, the detector is typically placed in the point of maximum dose. For isocentric plans, this point corresponds to the point of intersection of all of the beam central axes. For non-isocentric fields, there is by definition no point of intersection of the beam central axes, however, the point of maximum dose is still typically chosen for the detector position. Since the dose from each contributing beam is highest on the central axis, this point is near many of the beam central axes, although how near depends on the size of the target and the collimator chosen.

This point of maximum dose is a point at which the dose gradient is zero, however, when clinical field measurements are performed in highly conformal dose distributions, the setup uncertainty may contribute a significant amount to the total measurement uncertainty at that point. Furthermore, this region may be quite different from the optimal PCSR field, which has a low dose gradient in a volume surrounding the point of measurement as recommended in the Alfonso formalism [13]. Therefore, a different approach is proposed to select the point of measurement within clinical fields, seeking to minimize the dose gradient in a region surrounding the detector.

This approach follows an iterative algorithm. First, the dose distribution $D(\vec{r})$ of the clinical field is calculated on the Bullet phantom using the ray-tracing dose calculation algorithm of the Multiplan TPS from Accuray. Then, the integral I is defined for each point $\vec{r}$ in the dose distribution $D(\vec{r})$:

$$I(\vec{r}) = \iiint_{|\vec{r}-\vec{r}'|\leq 2\,\mathrm{mm}} \left| \frac{\vec{\nabla} D(\vec{r}')}{D(\vec{r}')} \right| \mathrm{d}\vec{r}'^3 \tag{3.13}$$

This quantity is small at points for which the magnitude of the normalized gradient $\left|\frac{\vec{\nabla} D(\vec{r}')}{D(\vec{r}')}\right|$ is small in a sphere of radius 2 mm surrounding the point. The 2 mm radius was chosen to make the integrated volume comparable to the largest volume detector considered, the A26 microchamber, which has a 3.3 mm diameter active volume. It was observed that for non-isocentric fields, the exact position chosen by this algorithm was sensitive to the size of the volume over which the dose gradient metric was integrated, therefore this method is by no means presented as the only way to select such a point.

The optimal dose gradient metric point $\vec{r}_{I_{min}}$ is found by searching for the point $\vec{r}$ for which the integral $I(\vec{r})$ is minimized:

$$I(\vec{r}_{I_{min}}) = \min_{\vec{r}} \{ I(\vec{r}) \mid D(\vec{r}) \geq 80\% \cdot D_{max} \} \tag{3.14}$$

Only points that have a dose higher than 80% of the maximum dose D_{max} are considered. In this way, low-dose areas that might be more uniform, but less relevant for the clinical field measurement, are avoided.

The position of the detector is changed to the optimal dose gradient metric point $\vec{r}_{I_{min}}$ by shifting the entire Bullet phantom. This constitutes the first iteration of the algorithm; the phantom has changed position within the field, therefore strictly speaking, the dose distribution has changed. The optimal dose gradient metric point within this new dose distribution may not be at the same position as before. The dose is therefore recalculated for the phantom's new position, and the optimal dose gradient metric point $\vec{r}_{I_{min}}$ is determined. This procedure of shifting the phantom, recalculating the dose, and determining $\vec{r}_{I_{min}}$ is repeated until the optimal dose gradient metric point is stable to within one dose matrix voxel from one iteration to the next. Typically no more than one iteration of this process was required.

The final $\vec{r}_{I_{min}}$ is the point at which the detectors are placed for the $k_{Q_{\text{clin}},Q_{\text{msr}}}^{f_{\text{clin}},f_{\text{msr}}}$ and $k_{Q_{\text{pcsr}},Q_{\text{msr}}}^{f_{\text{pcsr}},f_{\text{msr}}}$ calculations. Simulations were also performed with the detector at the point of maximum dose in order to determine the effect that the detector position has on the correction factor. For the isocentric fields, the optimal dose gradient metric point coincided with the point of maximum dose, and therefore the point of intersection of the beam central axes. This is expected, since the region near central axis for small (and large) static fields generally has a smaller dose gradient than the penumbra region away from central axis.

3.3 `egs_chamber` Settings

The `egs_chamber` user code was used to model particle transport within the phantom and each detector studied for the calculation of the clinical field correction factors. Similar settings were used for these calculations as for the beam modelling (see Section 2.4.2). Low-energy particle transport thresholds of `ECUT`=512 keV and `PCUT`=10 keV for charged particles and photons, respectively, were used throughout the `egs_chamber` simulations. The EGSnrc particle transport settings were set to the `egs_chamber` default values.

Variance Reduction

Every variance reduction technique available in `egs_chamber` was employed to improve the efficiency of the calculation of the clinical field correction factors. Full descriptions of these techniques are found in Section 2.4.2.

The IPSS technique [36, 45] allowed for the efficient and simultaneous calculation of the total and intermediate correction factors for all three detectors in a single simulation. The IPSS volume was a cylinder of radius 3.176 mm and length 41.479 mm, just large enough to enclose the entire volume of each detector. This first part of the particle shower was done in the phantom (Bullet for clinical and PCSR fields, water for the MSR field) until particles reached the IPSS volume. In the second part of the shower, particle transport is performed in every intermediate geometry for each detector, and dose is calculated in the scoring regions; the intermediate geometries and cavity doses are described in Section 3.2.4. The use of this technique ensures that the phantom portion of the particle shower only occurs once, which can significantly reduce the time required to calculate intermediate and total correction factors for the three different detectors.

CS was used in conjunction with IPSS, in order to automatically and more efficiently calculate dose ratios present in the total and intermediate correction factors. Large efficiency gains are realized when the two geometries representing the numerator and denominator of the ratio are similar and are therefore highly correlated [36, 47]. This is the case for the intermediate perturbation factors, where detectors components are individually replaced with phantom material or air.

The XCSE technique was also employed for these simulations. For the first part of the simulation, an XCSE shell of 10 mm thickness was defined around the IPSS volume. once the second part of the simulation began, XCSE shells of the same thickness were defined for each detector's intermediate volumes, around the wall surrounding the chamber active volume. An XCSE factor of 256 was used for these simulations.

The final variance reduction technique used in the `egs_chamber` simulations was range-based Russian Roulette. For the total and intermediate correction factors, the first RR volume was the IPSS volume; any charged particle not able to reach this region was subjected to RR. After reaching the IPSS volume, the RR volume was changed to include only the active volume of the detector of interest. An RR parameter of $N_r = 512$ was used for each simulation, chosen in order to optimize efficiency.

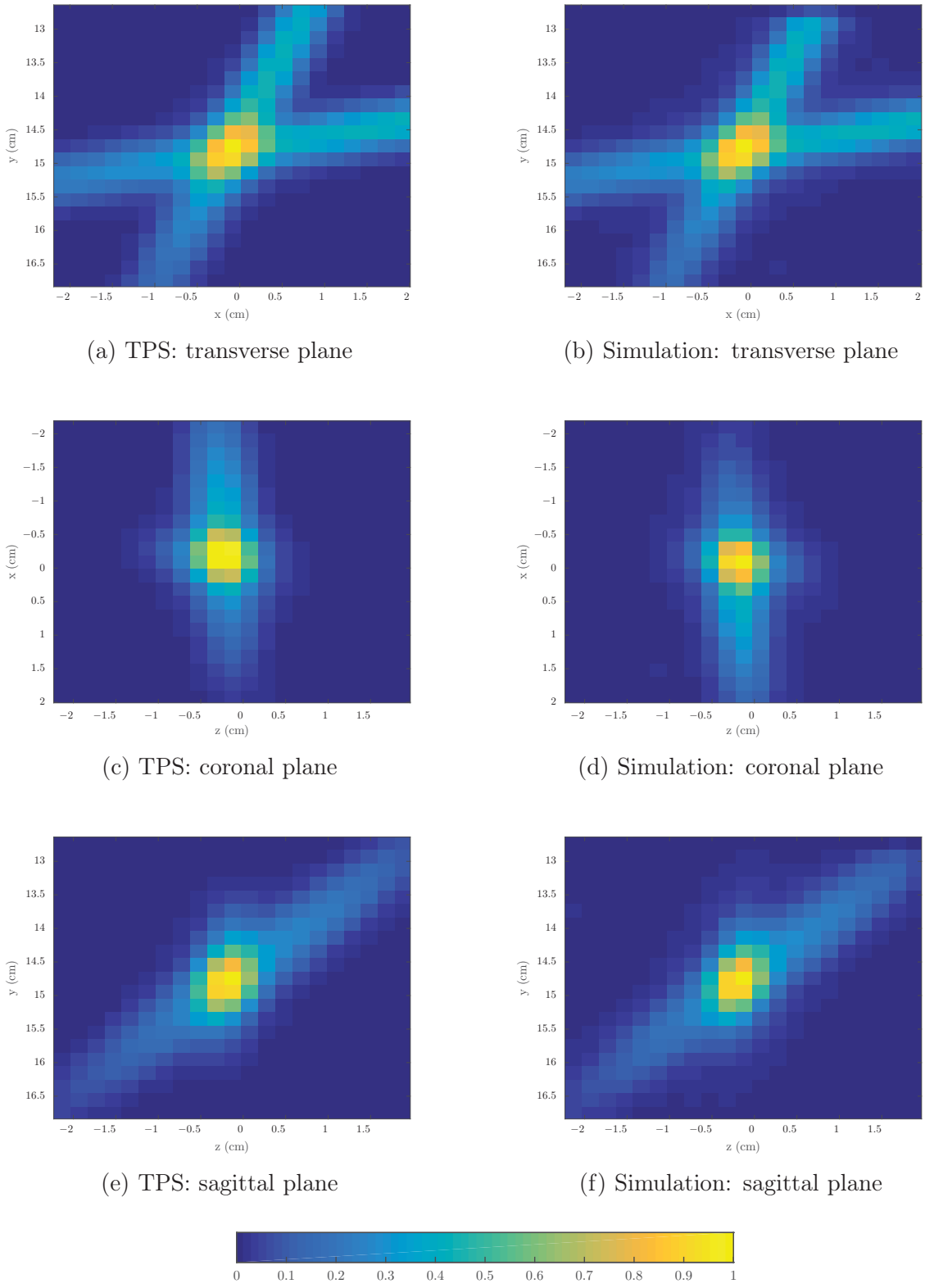

(a) TPS: transverse plane

(b) Simulation: transverse plane

(c) TPS: coronal plane

(d) Simulation: coronal plane

(e) TPS: sagittal plane

(f) Simulation: sagittal plane

Figure 3–3: Three orthogonal views of the dose distribution of the clinical field used to validate field delivery in the Monte Carlo simulation. Dose distributions were calculated by the TPS and using `egs_chamber`. Each distribution was normalized to 1, and the colourmap is scaled such that yellow corresponds to this maximal value.

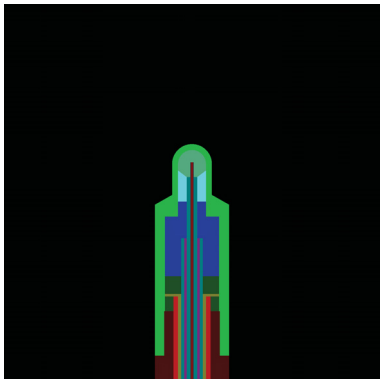

(a) D_{det}

(b) $D_{\text{cel,wall}}$

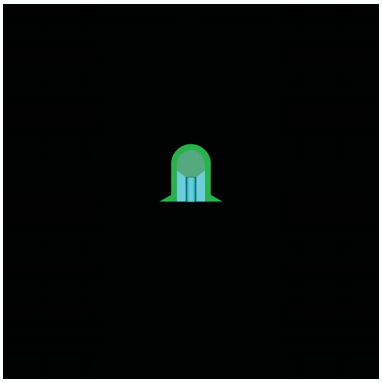

(c) D_{wall}

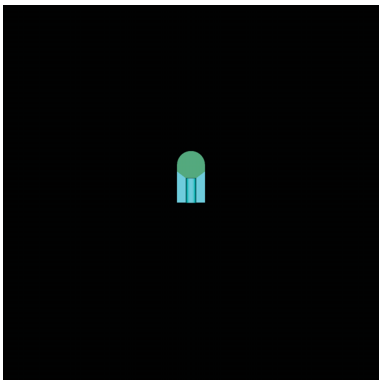

(d) D_{act}

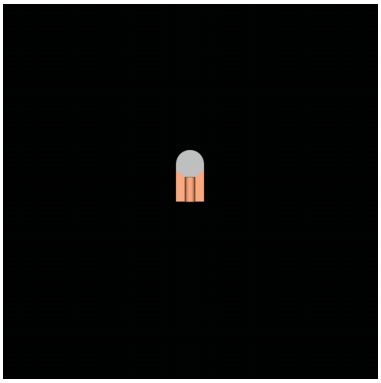

(e) D_{vapor}

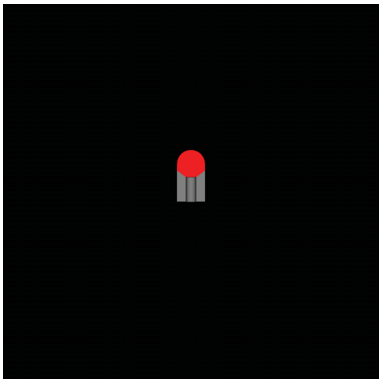

(f) $D_{w,\text{vol}}$

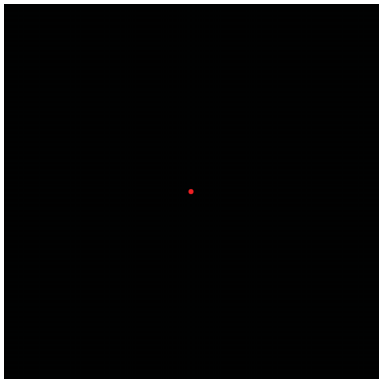

(g) $D_{w,\text{point}}$

Figure 3–4: The intermediate dose volumes for the A16 microchamber are displayed. Different colours indicate the materials of each component. In addition, the active volume of air surrounding the central electrode is coloured differently than regular air (a)-(d), indicating the region in which dose is scored. This is also done when air is replaced with air-dense water (e) and water-dense water (f).

CHAPTER 4
Calculation of Clinical Field Correction Factors: Results and Discussion

Total and intermediate correction factors were calculated for 21 composite fields in 6 clinical plan classes, and for three detectors: the A26 and A16 microchambers, and the W1 plastic scintillator. The results of these calculations are presented and discussed in this chapter.

4.1 Isocentric Clinical Plan Classes

4.1.1 Total Correction Factors

The total correction factors for the three clinical fields and the PCSR field within the isocentric plan-classes IS1, IS2, and IS3 are presented in Figures 4–1, 4–2, and 4–3, respectively. Figures 4–1a, 4–2a, and 4–3a show the $k_{Q_{\rm clin},Q_{\rm msr}}^{f_{\rm clin},f_{\rm msr}}$ correction factors, in which the detector response is calculated relative to the MSR field, while Figures 4–1b, 4–2b, and 4–3b show the $k_{Q_{\rm clin},Q_{\rm pcsr}}^{f_{\rm clin},f_{\rm pcsr}}$, in which the detector response is calculated relative to the particular PCSR field. The error bars represent the estimated statistical uncertainty in the calculated correction factors. Since for each field in the isocentric plan-classes, the point of maximum dose coincides with the optimal dose gradient metric point $\vec{r}_{I_{min}}$ (see Section 3.2.5), only one set of data for each field is shown.

In general, the $k_{Q_{\rm clin},Q_{\rm msr}}^{f_{\rm clin},f_{\rm msr}}$ correction factors were larger for the A26 than for the A16 microchamber, both requiring corrections greater than unity. The correction factors decreased as the collimator size used in the clinical field increased, in agreement with the results found by Francescon *et al.* [19]. The value of the A16 $k_{Q_{\rm pcsr},Q_{\rm msr}}^{f_{\rm pcsr},f_{\rm msr}}$ correction factors for the clinical fields are approximately 1% higher than the correction factors calculated for static fields in that study (when adjusted for the dependence on the electron beam FWHM), as shown in Table 4–1. It is important to note that the static field correction factors were calculated for the detector in the parallel orientation, while for the clinical fields used in this study,

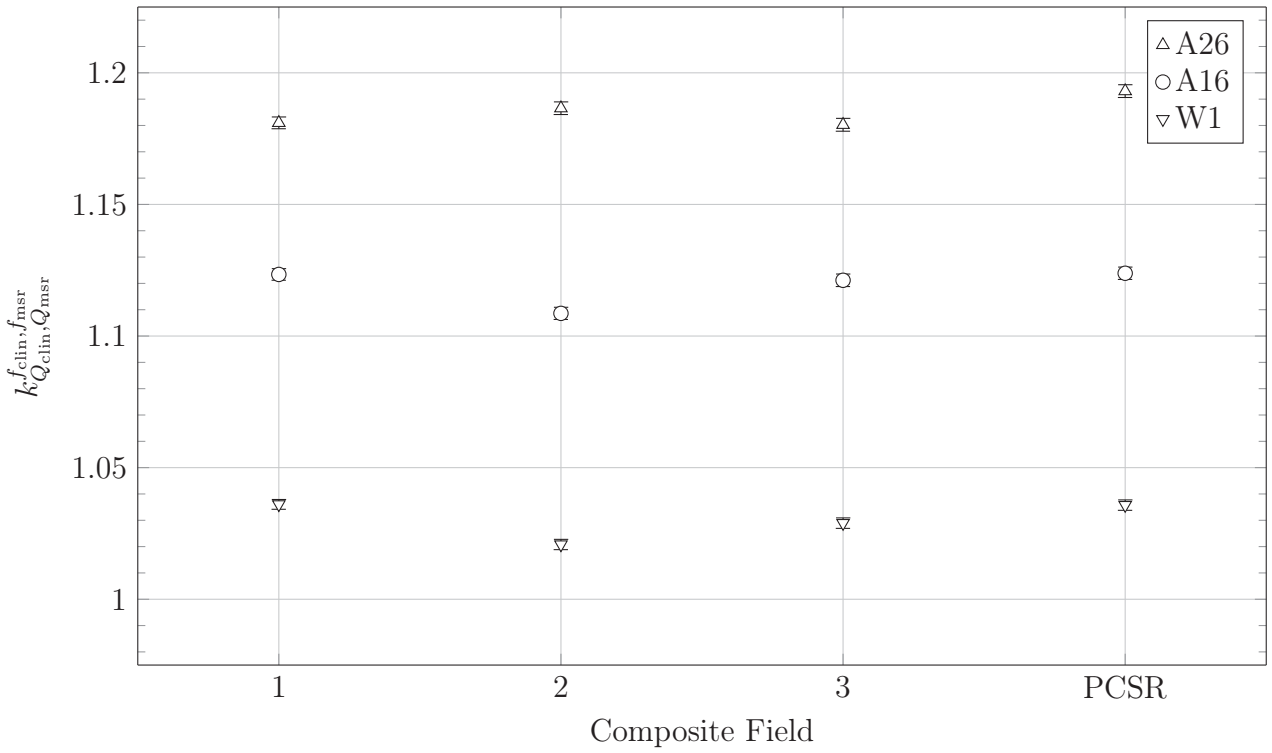

(a) Detector response relative to MSR field.

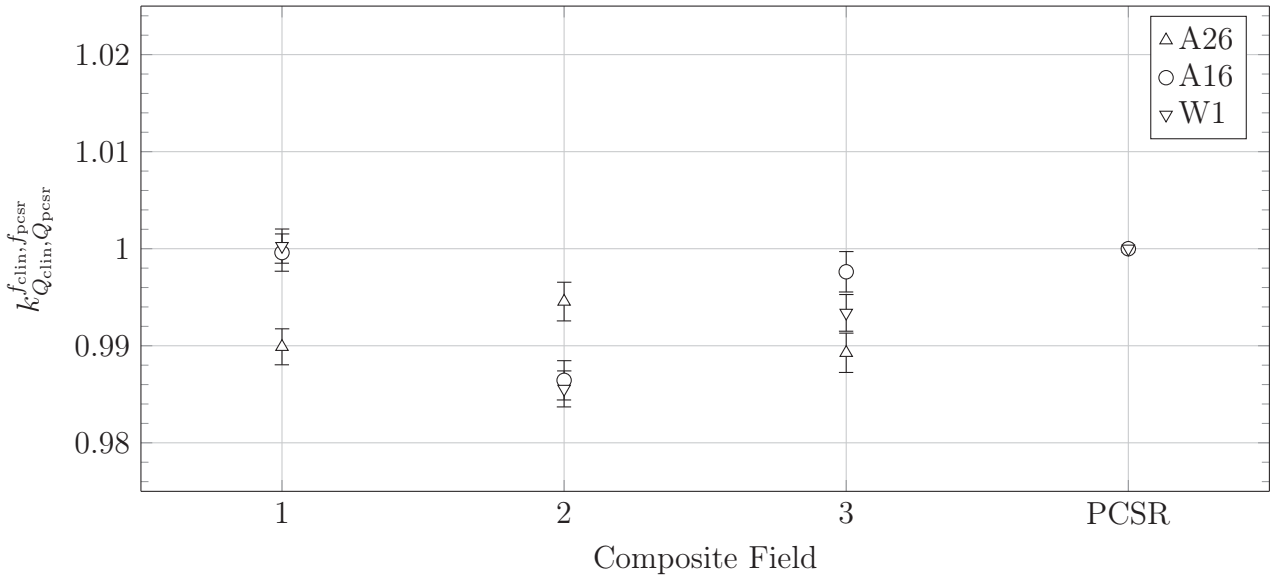

(b) Detector response relative to PCSR field.

Figure 4–1: Total $k_{Q_{\text{clin}},Q_{\text{msr}}}^{f_{\text{clin}},f_{\text{msr}}}$ and $k_{Q_{\text{clin}},Q_{\text{pcsr}}}^{f_{\text{clin}},f_{\text{pcsr}}}$ correction factors for clinical fields in plan-class IS1: isocentric delivery, skull path, and 5 mm collimator used exclusively.

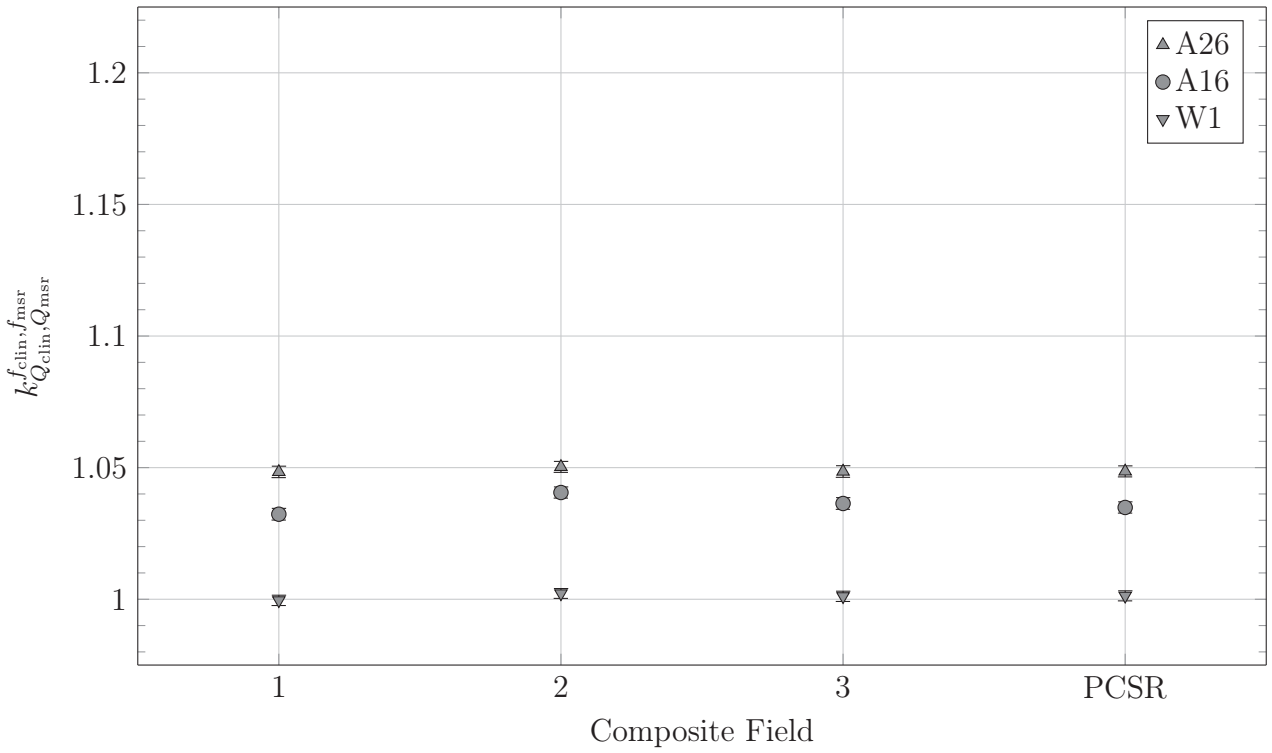

(a) Detector response relative to MSR field.

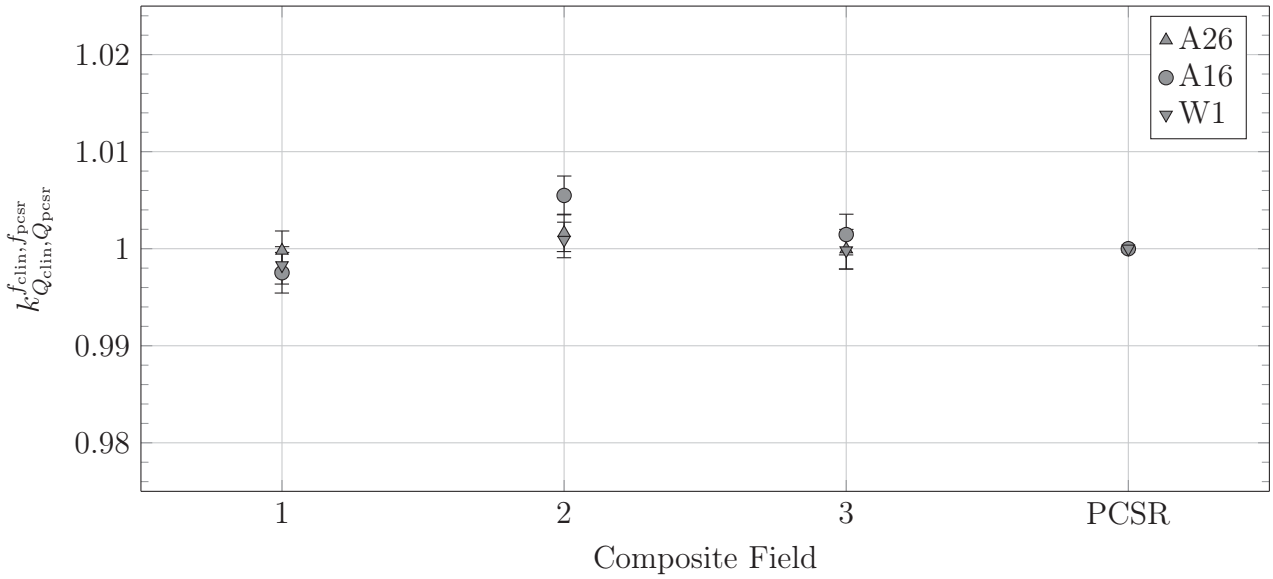

(b) Detector response relative to PCSR field.

Figure 4–2: Total $k_{Q_{\text{clin}},Q_{\text{msr}}}^{f_{\text{clin}},f_{\text{msr}}}$ and $k_{Q_{\text{clin}},Q_{\text{pcsr}}}^{f_{\text{clin}},f_{\text{pcsr}}}$ correction factors for clinical fields in plan-class IS2: isocentric delivery, skull path, and 7.5 mm collimator used exclusively.

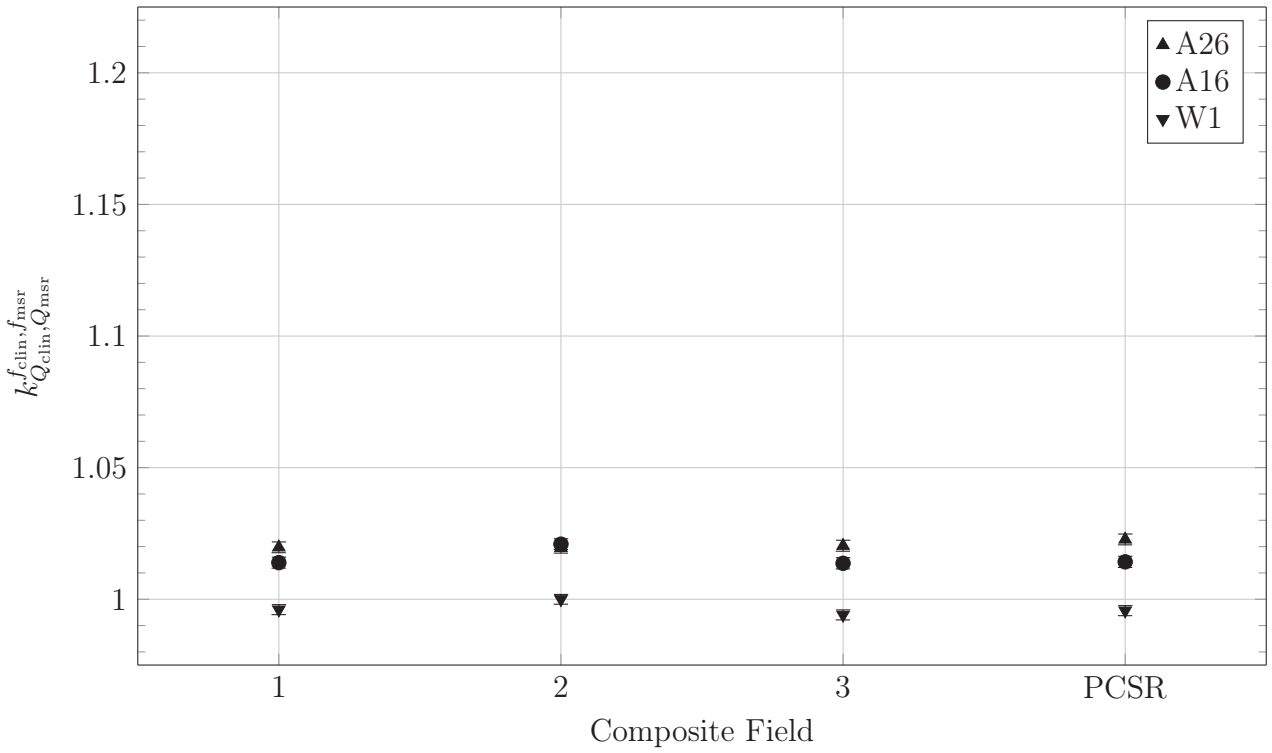

(a) Detector response relative to MSR field.

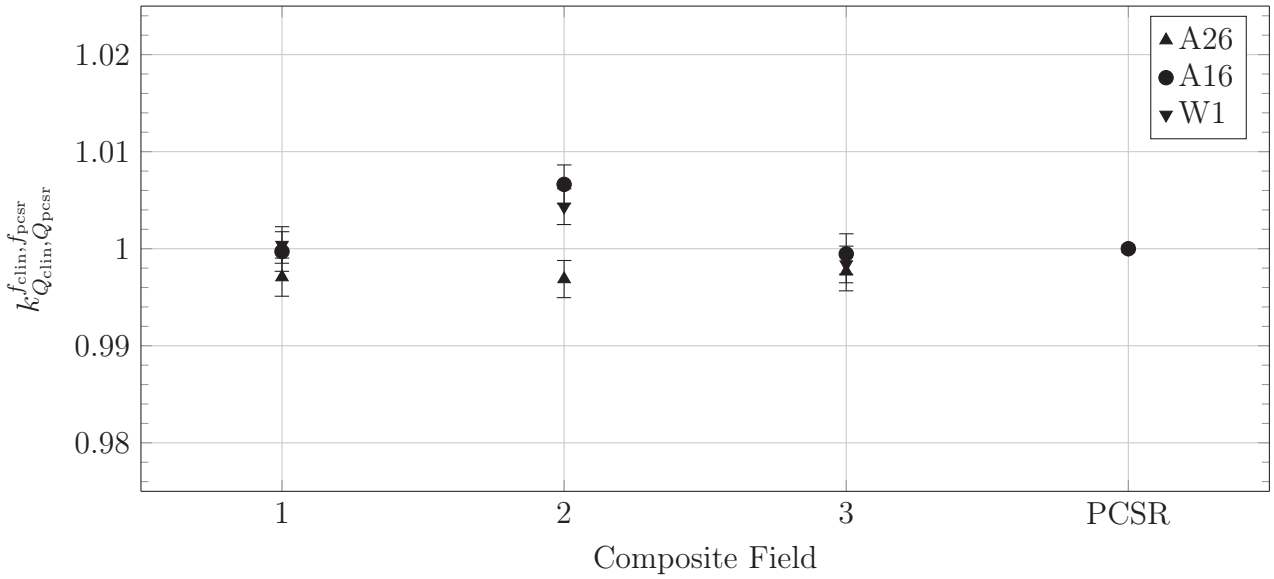

(b) Detector response relative to PCSR field.

Figure 4–3: Total $k_{Q_{\text{clin}},Q_{\text{msr}}}^{f_{\text{clin}},f_{\text{msr}}}$ and $k_{Q_{\text{clin}},Q_{\text{pcsr}}}^{f_{\text{clin}},f_{\text{pcsr}}}$ correction factors for clinical fields in plan-class IS3: isocentric delivery, skull path, and 10 mm collimator used exclusively.

the detector is rarely in this orientation relative to the beam. As Francescon *et al.* later reported an increase in the $k_{Q_{\text{clin}},Q_{\text{msr}}}^{f_{\text{clin}},f_{\text{msr}}}$ correction factor when the orientation was changed to the perpendicular orientation [22], a 1% increase from the static field, parallel orientation to composite clinical fields is not unreasonable.

Table 4–1: Comparison of the calculated clinical field correction factors to published values for small static fields for the A16 microchamber. The $k_{Q_{\text{pcsr}},Q_{\text{msr}}}^{f_{\text{pcsr}},f_{\text{msr}}}$ correction factors were used to represent the three plan-classes using different collimator sizes. Francescon *et al.* calculated the correction factors in static fields for a range of electron beam FWHMs [19] at a depth of 15 mm and SAD of 800 mm, with the detector oriented parallel to the beam. The values given below were found by interpolating these results using the beam FWHM used in this study, 2.5 mm.

Collimator diameter (mm)	Static field $k_{Q_{\text{clin}},Q_{\text{msr}}}^{f_{\text{clin}},f_{\text{msr}}}$	Composite field $k_{Q_{\text{pcsr}},Q_{\text{msr}}}^{f_{\text{pcsr}},f_{\text{msr}}}$
5	1.110	1.124
7.5	1.025	1.035
10	1.011	1.014

The correction factors for the W1 plastic scintillator were closest to 1, with less than a 4% correction required for the clinical and PCSR fields within the IS1 plan-class using the 5 mm collimator. The $k_{Q_{\text{clin}},Q_{\text{msr}}}^{f_{\text{clin}},f_{\text{msr}}}$ for the W1 for the clinical fields in the other isocentric plan-classes using the larger collimators were within 0.5% of unity. As shown in Section 1.3.3, Francescon *et al.* calculated a correction factor within 1% of unity for the W1 for the 5 mm collimator, through a range of depths and off-axis positions. The discrepancy between this result and the $k_{Q_{\text{clin}},Q_{\text{msr}}}^{f_{\text{clin}},f_{\text{msr}}}$ correction factors of fields in plan-class IS1 will be resolved by analyzing the intermediate correction factors in Section 4.1.2.

The detectors respond similarly in the clinical fields within each plan-class to the PCSR field representing the class, as seen by comparing the $k_{Q_{\text{clin}},Q_{\text{msr}}}^{f_{\text{clin}},f_{\text{msr}}}$ and $k_{Q_{\text{pcsr}},Q_{\text{msr}}}^{f_{\text{pcsr}},f_{\text{msr}}}$ correction factors. The $k_{Q_{\text{clin}},Q_{\text{pcsr}}}^{f_{\text{clin}},f_{\text{pcsr}}}$ (ratio of the former to the latter correction factor) are within 1.5%, 0.6%, and 0.7% of unity for each clinical field within plan-classes IS1 (5 mm), IS2 (7.5 mm), and IS3 (10 mm), respectively. Therefore the chosen PCSR field fulfills the requirements defined in Section 1.3.2 to be representative of each of the three clinical fields within its represented class, for the three isocentric plan-classes investigated. This is true for all three

detectors, including the A26, which requires the largest $k^{f_{\text{clin}},f_{\text{msr}}}_{Q_{\text{clin}},Q_{\text{msr}}}$ correction factor. This demonstrates that for the isocentric clinical fields investigated, the collimator and beam path used to define the field may be used to determine the $k^{f_{\text{clin}},f_{\text{msr}}}_{Q_{\text{clin}},Q_{\text{msr}}}$ and $k^{f_{\text{pcsr}},f_{\text{msr}}}_{Q_{\text{pcsr}},Q_{\text{msr}}}$.

4.1.2 Intermediate Correction Factors

The intermediate correction factors, as defined in Section 3.2.4, were calculated for the PCSR field representing plan-classes IS1, IS2, and IS3, and are presented in Figures 4–4, 4–5, and 4–6, respectively. The error bars represent the estimated statistical uncertainty in the calculated correction factors. The intermediate correction factors for the clinical fields in each plan-class are within 1.5% of the corresponding intermediate correction factor for the PCSR field representing that plan-class. Therefore the intermediate correction factors for the clinical fields are not shown here, as the PCSR field represents the class adequately.

The largest magnitude intermediate correction factors for both the A16 and A26 microchambers are the $[P_\rho]^{f_{\text{pcsr}},f_{\text{msr}}}_{Q_{\text{pcsr}},Q_{\text{msr}}}$ and $[P_{\text{vol}}]^{f_{\text{pcsr}},f_{\text{msr}}}_{Q_{\text{pcsr}},Q_{\text{msr}}}$ intermediate correction factors. This agrees with the small field correction factors calculated by several authors [8, 16, 18]. As explained in Section 3.2.4, these correct for the difference in density between water and air, and the volume averaging effect, respectively. The large $[P_\rho]^{f_{\text{pcsr}},f_{\text{msr}}}_{Q_{\text{pcsr}},Q_{\text{msr}}}$ correction factor is due to the lack of lateral CPE in the small fields composing the clinical field: the low-density air cavity causes a large perturbation to the detector response relative to the situation in which lateral CPE is established (see Section 1.3.1). Conversely, the $[P_{\text{vol}}]^{f_{\text{pcsr}},f_{\text{msr}}}_{Q_{\text{pcsr}},Q_{\text{msr}}}$ correction factor is due to the highly non-uniform dose distribution in the small field across the detector volume.

The A26 microchamber has a larger air cavity than the A16 (3.3 mm cavity diameter versus 2.4 mm). Therefore the lack of CPE in the small fields, as well as the non-uniform dose distribution, have a greater effect on the $[P_\rho]^{f_{\text{pcsr}},f_{\text{msr}}}_{Q_{\text{pcsr}},Q_{\text{msr}}}$ and $[P_{\text{vol}}]^{f_{\text{pcsr}},f_{\text{msr}}}_{Q_{\text{pcsr}},Q_{\text{msr}}}$ correction factors for this larger chamber. This causes these two intermediate correction factors to be larger for the A26 than for the A16, resulting in the larger total correction factor for the former detector shown in Section 4.1.1.

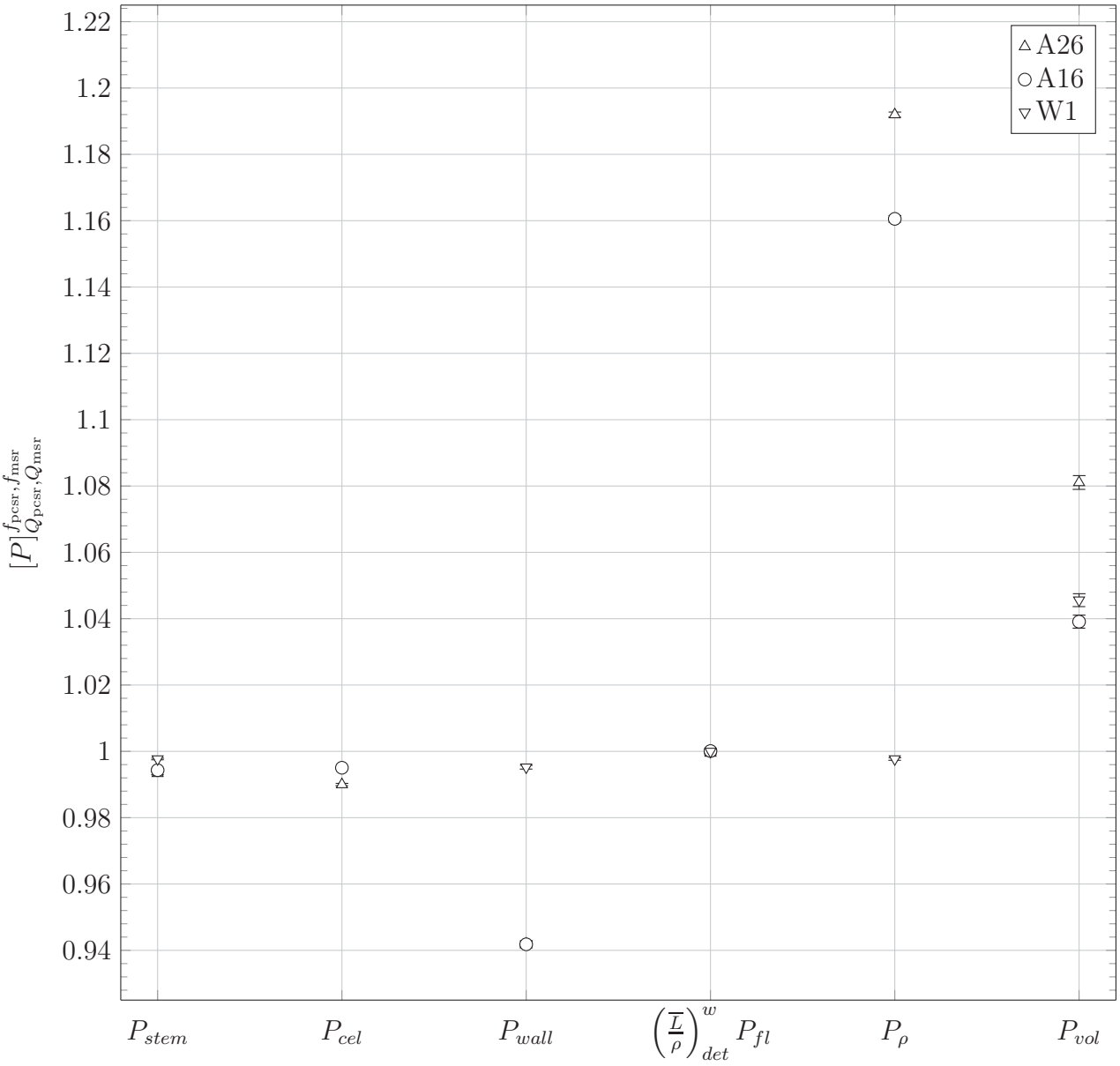

Figure 4–4: Intermediate correction factors $[P_c]^{f_{\mathrm{pcsr}},f_{\mathrm{msr}}}_{Q_{\mathrm{pcsr}},Q_{\mathrm{msr}}}$ for the representative PCSR field of isocentric plan-class IS1 (5 mm collimator).

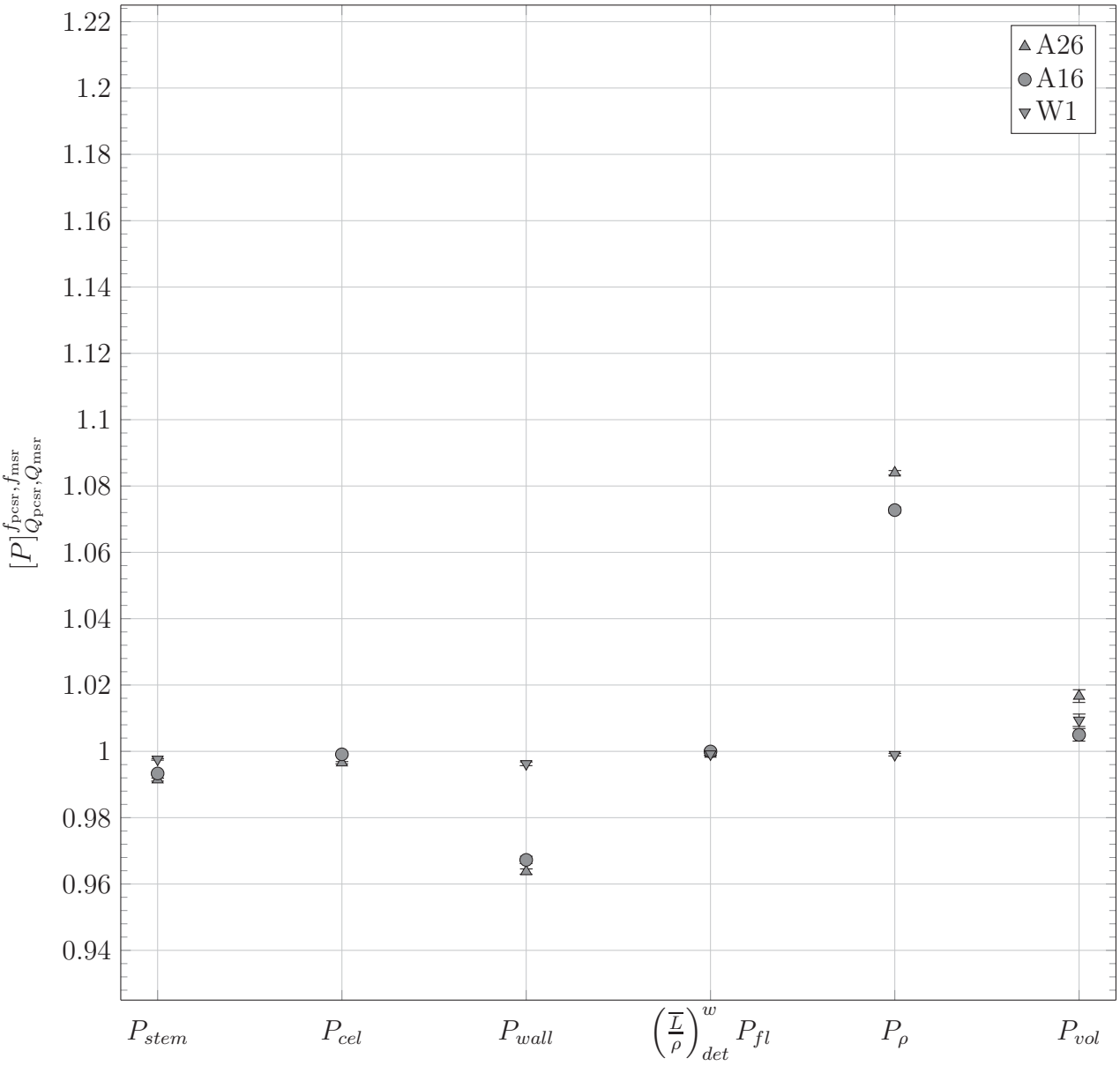

Figure 4–5: Intermediate correction factors $[P_c]^{f_{\mathrm{pcsr}},f_{\mathrm{msr}}}_{Q_{\mathrm{pcsr}},Q_{\mathrm{msr}}}$ for the representative PCSR field of isocentric plan-class IS2 (7.5 mm collimator).

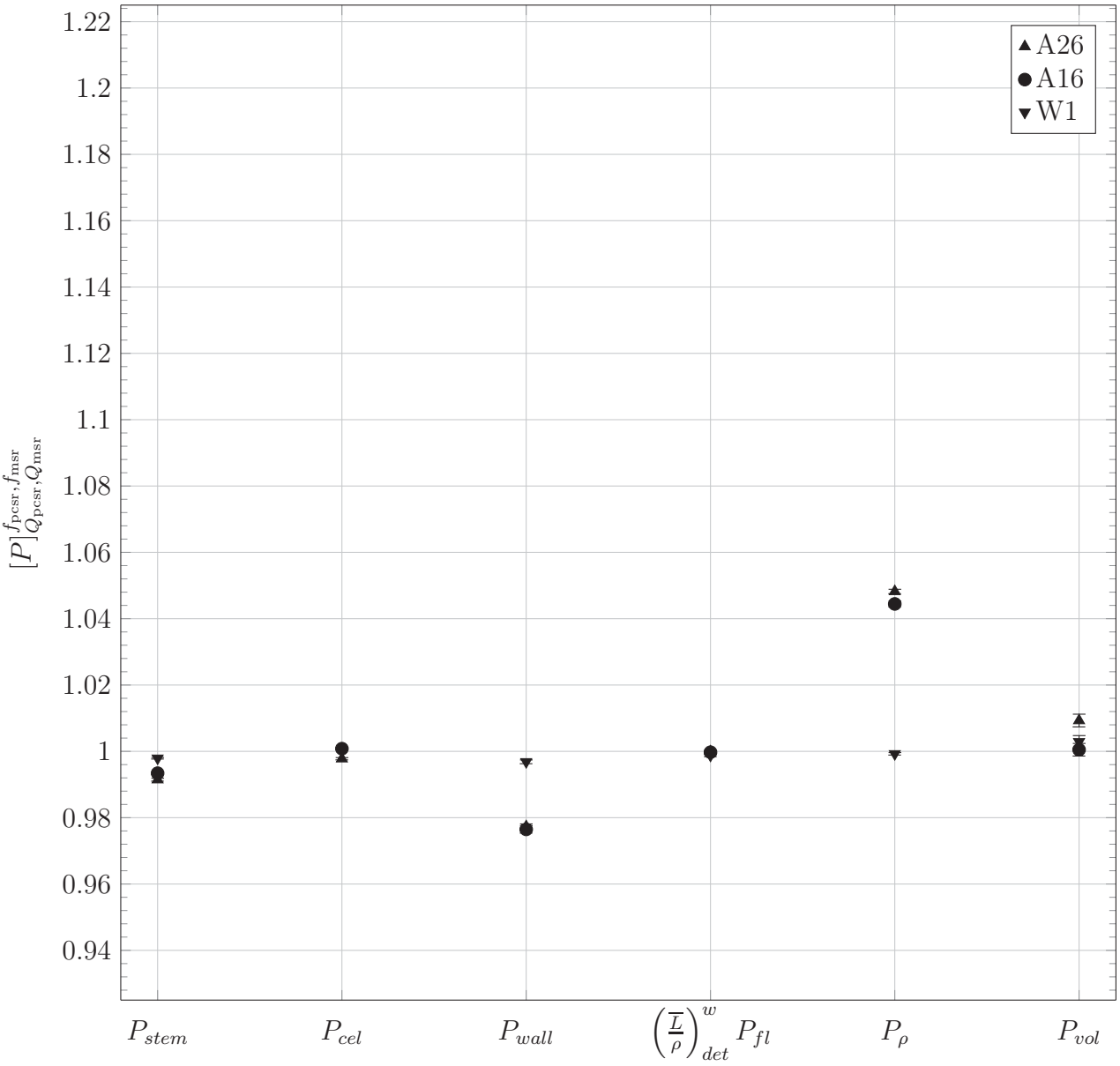

Figure 4–6: Intermediate correction factors $[P_c]^{f_{\mathrm{pcsr}},f_{\mathrm{msr}}}_{Q_{\mathrm{pcsr}},Q_{\mathrm{msr}}}$ for the representative PCSR field of isocentric plan-class IS3 (10 mm collimator).

Both the $[P_\rho]^{f_{\text{pcsr}},f_{\text{msr}}}_{Q_{\text{pcsr}},Q_{\text{msr}}}$ and $[P_{\text{vol}}]^{f_{\text{pcsr}},f_{\text{msr}}}_{Q_{\text{pcsr}},Q_{\text{msr}}}$ intermediate correction factors decrease as the collimator diameter used in the PCSR field increases. As seen in Section 1.3.3, the decrease of $[P_\rho]^{f_{\text{pcsr}},f_{\text{msr}}}_{Q_{\text{pcsr}},Q_{\text{msr}}}$ can be attributed to an increase in the lateral CPE in the larger fields, while the decrease of $[P_{\text{vol}}]^{f_{\text{pcsr}},f_{\text{msr}}}_{Q_{\text{pcsr}},Q_{\text{msr}}}$ is due to the more uniform dose distribution present in the larger collimators. The decrease of these two intermediate correction factors in turn causes the decrease of the total correction factors $k^{f_{\text{clin}},f_{\text{msr}}}_{Q_{\text{clin}},Q_{\text{msr}}}$ and $k^{f_{\text{pcsr}},f_{\text{msr}}}_{Q_{\text{pcsr}},Q_{\text{msr}}}$ with increasing collimator diameter, which is shown in Section 4.1.1.

The remaining intermediate correction factors are within 1% of unity for the microchambers, with the exception of $[P_{\text{wall}}]^{f_{\text{pcsr}},f_{\text{msr}}}_{Q_{\text{pcsr}},Q_{\text{msr}}}$. This correction factor accounts for the difference in dose scored in the chamber active volume when the plastic wall is replaced with solid water. A 6% correction below unity is required for both microchambers for clinical fields using the 5 mm collimator, decreasing to 4% for the 7.5 mm collimator and 2% for the 10 mm.

With the exception of $[P_{\text{vol}}]^{f_{\text{pcsr}},f_{\text{msr}}}_{Q_{\text{pcsr}},Q_{\text{msr}}}$ in the IS1 PCSR field (5 mm collimator), the intermediate correction factors for the W1 plastic scintillator were calculated to be within 0.5% of 1. In the case of $[P_{\text{stem}}]^{f_{\text{pcsr}},f_{\text{msr}}}_{Q_{\text{pcsr}},Q_{\text{msr}}}$, $[P_{\text{wall}}]^{f_{\text{pcsr}},f_{\text{msr}}}_{Q_{\text{pcsr}},Q_{\text{msr}}}$, and $\left[\left(\frac{\overline{L}}{\rho}\right)^{w}_{det} P_{\text{fl}}\right]^{f_{\text{pcsr}},f_{\text{msr}}}_{Q_{\text{pcsr}},Q_{\text{msr}}}$, this can be attributed to the use of water-equivalent materials throughout the scintillator's construction, as there is no significant perturbation presented by the detector components. The active volume is comparatively small (1.0 mm diameter, 3.0 mm length) and constructed of polystyrene, which has a density that is similar to water (1.05 g/cm^3); therefore this volume presents a minimal perturbation relative to a water volume of the same size. These properties explain why although the small fields have a lack of lateral CPE, the $[P_\rho]^{f_{\text{pcsr}},f_{\text{msr}}}_{Q_{\text{pcsr}},Q_{\text{msr}}}$ correction factor is within 0.3% of 1 for the plastic scintillator.

The volume averaging intermediate correction factor is therefore responsible for the approximately 3% under-response calculated for the W1 in clinical fields within plan-class IS1, as all other intermediate correction factors are not significantly different from unity. Indeed, $[P_{\text{vol}}]^{f_{\text{pcsr}},f_{\text{msr}}}_{Q_{\text{pcsr}},Q_{\text{msr}}}$ for the PCSR field of this plan-class is equal to 1.046. As discussed in Section 4.1.1, Francescon *et al.* did not observe such an under-response with the W1 in

the parallel orientation, even when using the 5 mm collimator in CyberKnife [16]. In this orientation, the detector is presenting its smallest dimension (1.0 mm diameter) to the beam: minimal volume averaging is observed. However, in CyberKnife clinical fields, the detector is rarely in this orientation; instead, it is at a non-zero angle with respect to the beam. At these orientations, the active volume can appear as long as 3 mm from the beam's perspective (this being the actual length of the active volume). The averaging of the dose distribution in the active volume for fields using the 5 mm collimator results in the non-unity values of the $k_{Q_{\text{clin}},Q_{\text{msr}}}^{f_{\text{clin}},f_{\text{msr}}}$ and $k_{Q_{\text{pcsr}},Q_{\text{msr}}}^{f_{\text{pcsr}},f_{\text{msr}}}$ for fields in plan-class IS1.

4.2 Non-Isocentric Clinical Plan Classes

4.2.1 Total Correction Factors

As described in Table 3–1, three non-isocentric plan-classes were investigated: NT1 (trigeminal neuralgia path, 5 mm collimator), NT2 (trigeminal neuralgia path, 5 mm and 7.5 mm collimator), and NS1 (skull path, 5 mm and 7.5 mm collimator). The total correction factors for the three clinical fields within each plan-class are presented in Figures 4–7, 4–8, and 4–9, respectively. The error bars represent the estimated statistical uncertainty in the calculated correction factors. As mentioned in Section 3.2.5, the selection of the detector position is non-trivial, therefore $k_{Q_{\text{clin}},Q_{\text{msr}}}^{f_{\text{clin}},f_{\text{msr}}}$ correction factors were calculated at two points within each clinical field. The point of maximum dose coincides with the optimal dose gradient metric point $\vec{r}_{I_{min}}$ for each field within plan-class NT1, therefore only one set of data for each field is shown. However, with the exception of field 2 in plan-class NT2, the clinical fields in plan-classes NT2 and NS1 did not have this property. Figures 4–8a and 4–9a show the $k_{Q_{\text{clin}},Q_{\text{msr}}}^{f_{\text{clin}},f_{\text{msr}}}$ at the point of maximum dose within the field, while Figures 4–8b and 4–9b show the correction factors at the optimal dose gradient metric point $\vec{r}_{I_{min}}$.

The correction factors for clinical fields in plan-class NT1 represented the largest $k_{Q_{\text{clin}},Q_{\text{msr}}}^{f_{\text{clin}},f_{\text{msr}}}$ observed for all non-isocentric fields. The variation of the correction factors between fields in this class was high when the A26 was included, at 3.5%. When the A26 was omitted, the agreement improved to less than 1%, meeting the ideal requirements for consideration

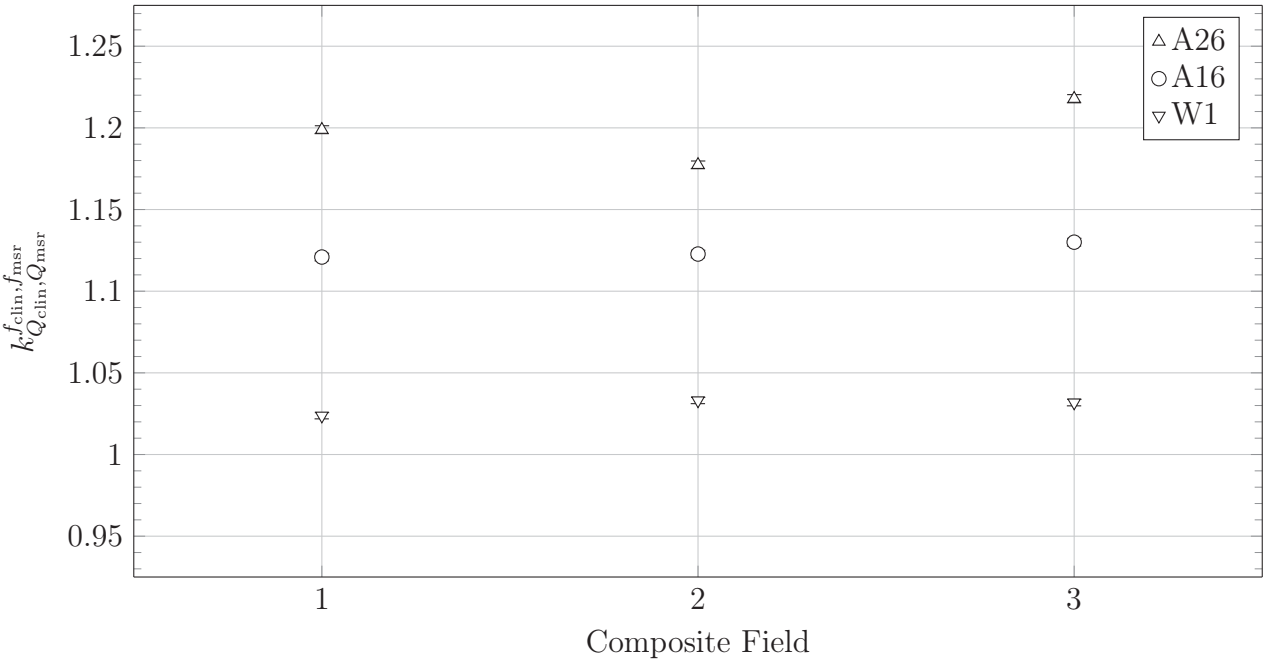

Figure 4–7: Total $k^{f_{\text{clin}},f_{\text{msr}}}_{Q_{\text{clin}},Q_{\text{msr}}}$ and correction factors for clinical fields in plan-class NT1: non-isocentric delivery, trigeminal neuralgia path, and 5 mm collimator used exclusively.

of a PCSR field in Section 3.1.2. The decision to not create such a field for this plan class is discussed below.

The $k^{f_{\text{clin}},f_{\text{msr}}}_{Q_{\text{clin}},Q_{\text{msr}}}$ correction factors for clinical fields in plan-class NT2 were calculated at two points within the field: the point of maximum dose (Figure 4–8a), and the optimal dose gradient metric point $\vec{r}_{I_{min}}$ (Figure 4–8b), described in Section 3.2.5. For clinical field 2, these two points coincided, while they were distinct for the other fields. As expected, correction factors for these fields are smaller than those for fields using the 5 mm exclusively (plan-classes IS1 and NT1), and greater than those for fields using only the 7.5 mm collimator (plan-class IS2); the W1 plastic scintillator still requires as much as a 1% correction above unity, due to the use of the 7.5 mm and the smaller 5 mm collimators. For field 1, $k^{f_{\text{clin}},f_{\text{msr}}}_{Q_{\text{clin}},Q_{\text{msr}}}$ is larger at the optimal dose gradient metric point than at the maximum dose point, by as much as 3.8%, while $k^{f_{\text{clin}},f_{\text{msr}}}_{Q_{\text{clin}},Q_{\text{msr}}}$ for field 3 is lower at the optimal dose gradient metric point by as much as 1.0%.

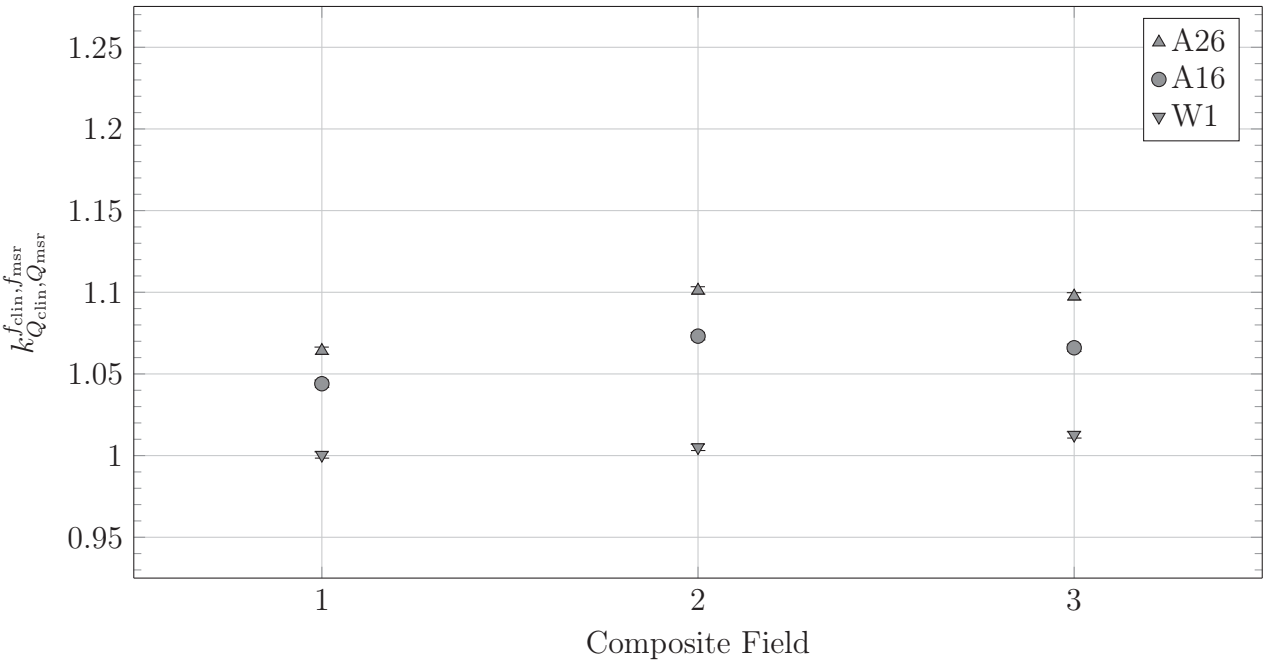

(a) Detector response relative to MSR field at maximum dose point.

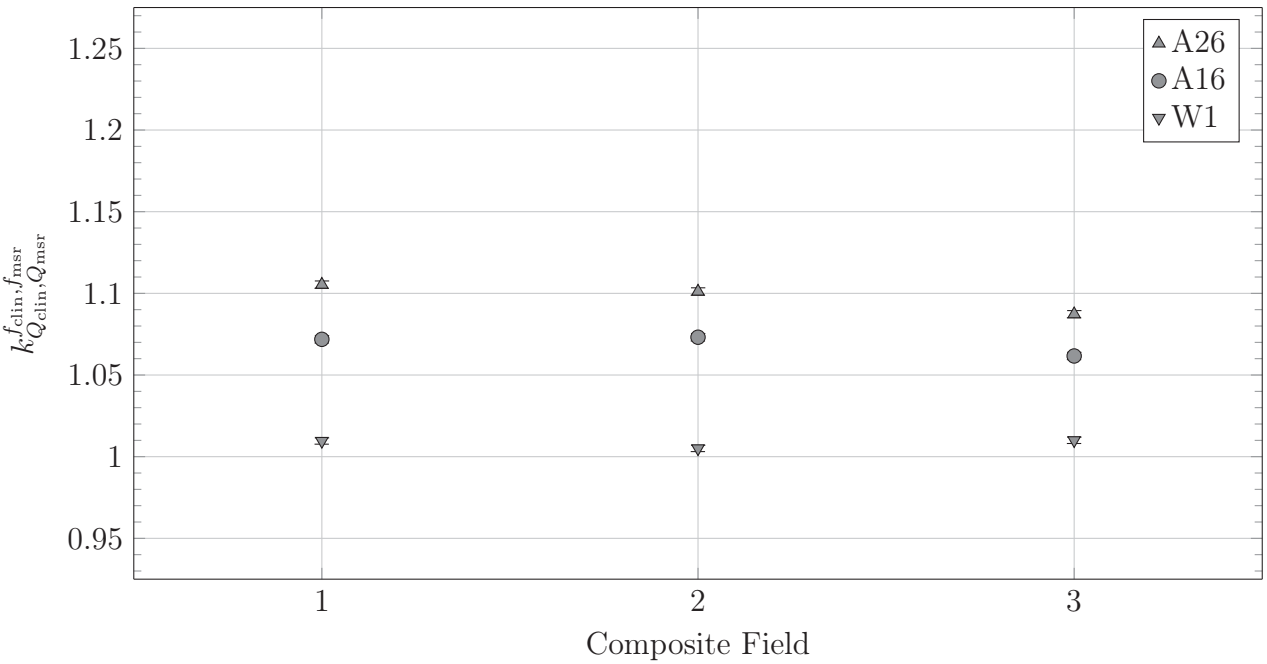

(b) Detector response relative to MSR field at optimal dose gradient metric point.

Figure 4–8: Total $k^{f_{\text{clin}},f_{\text{msr}}}_{Q_{\text{clin}},Q_{\text{msr}}}$ correction factors for clinical fields in plan-class NT2: non-isocentric delivery, trigeminal neuralgia path, and both 5 mm and 7.5 mm collimators used.

In addition, the intra-plan-class variability of the total correction factor is decreased when moving from the point of maximum dose to the optimal dose gradient metric point, from 3.5% to 1.7%. This suggests that the notion of grouping non-isocentric clinical fields in which detectors require similar correction factors performs better at this optimal dose gradient metric point for these fields. Unlike the non-isocentric fields in plan-class NT1, these fields utilize two different collimators. Therefore the $k_{Q_{\text{clin}},Q_{\text{msr}}}^{f_{\text{clin}},f_{\text{msr}}}$ correction factors for fields in plan-class NT2 cannot be easily compared to a those of a corresponding isocentric field, as the ones investigated in this study used only a single collimator.

The results of the total correction factor calculation for clinical fields in plan-class NS1 can be found in Figures 4–9a and 4–9b for the maximum dose point and the optimal dose gradient metric point, respectively. For each field within this plan-class, these two points are distinct. The $k_{Q_{\text{clin}},Q_{\text{msr}}}^{f_{\text{clin}},f_{\text{msr}}}$ is larger at the maximum dose point than at the optimal dose gradient metric point for fields 1 and 2 by as much as 4.8%; there is a negligible difference for field 3. For fields 1 and 2, the $k_{Q_{\text{clin}},Q_{\text{msr}}}^{f_{\text{clin}},f_{\text{msr}}}$ are within 1% of unity at the optimal point, with all detectors having a correction factor less than 1 for field 1, while for field 2 (and field 3) this is true of only the W1 plastic scintillator. This is unintuitive behaviour for microchambers, as it seemingly contradicts the under-response typically observed in small fields, as explained in Sections 1.3.1 and 1.3.3. This also leads to a larger intra-plan-class variability of the total correction factor at the optimal dose gradient metric point compared to the maximum dose point (4.2% and 1.9%, respectively).

It is useful to recall one of the properties of clinical fields in this plan-class, particularly the distribution of dose around the target: the beams were delivered in such a way that the centre of the target receives less dose than the periphery. In certain clinical fields, the central region of the target may therefore constitute a low-dose gradient area, which is selected by the algorithm defined in Section 3.2.5 to be the optimal dose gradient metric point $\vec{r}_{I_{min}}$. This was the case for fields 1 and 2, while the optimal dose gradient metric point for field 3 was on the high-dose edge of the target. The difference in dosimetric conditions in this

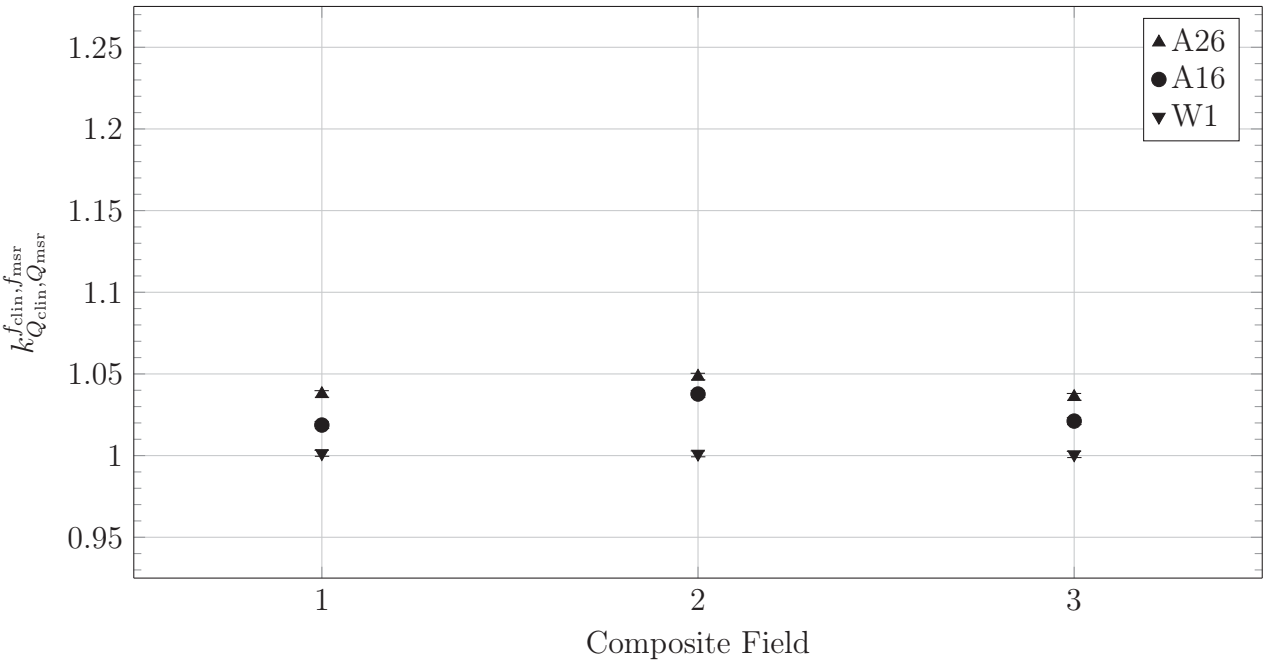

(a) Detector response relative to MSR field at maximum dose point.

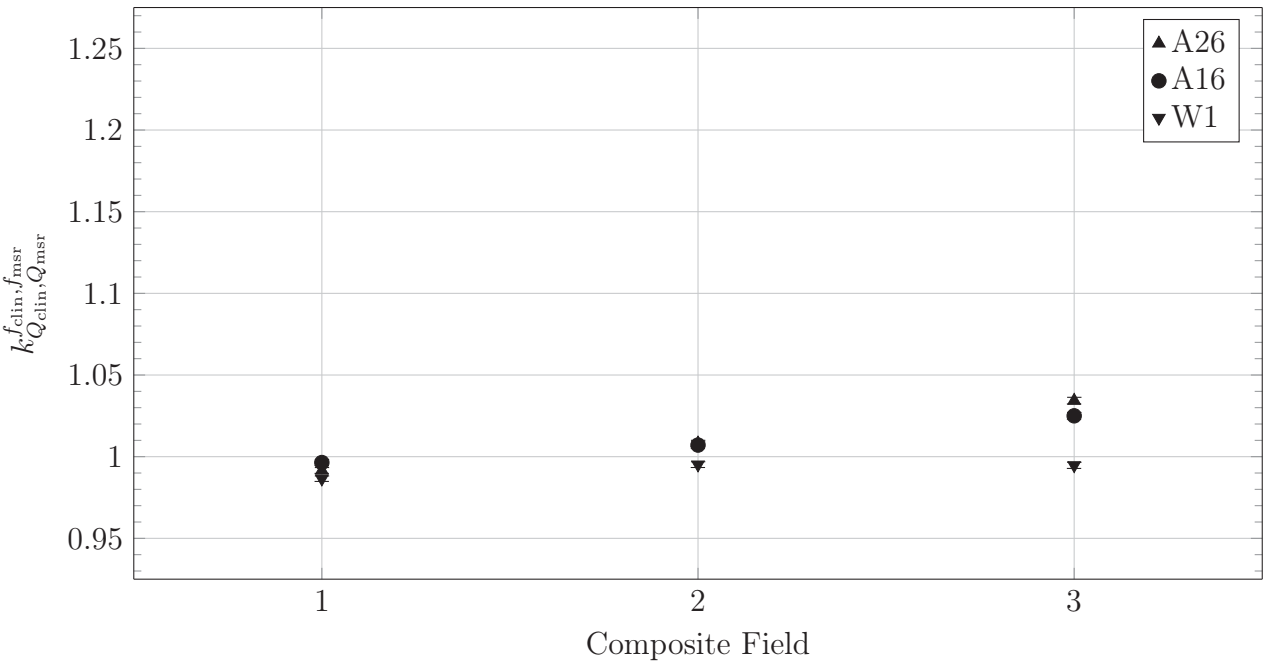

(b) Detector response relative to MSR field at optimal dose gradient metric point.

Figure 4–9: Total $k_{Q_{\text{clin}},Q_{\text{msr}}}^{f_{\text{clin}},f_{\text{msr}}}$ correction factors for clinical fields in plan-class NS1: non-isocentric delivery, skull path, and both 5 mm and 7.5 mm collimators used.

low-gradient centre compared to the edge of the target, where the point of maximum dose for these fields lies, will be investigated in Section 4.2.2. These conditions will help explain the differences seen in the $k_{Q_{\text{clin}},Q_{\text{msr}}}^{f_{\text{clin}},f_{\text{msr}}}$ between the two points for fields 1 and 2, as well the absence of a meaningful difference for field 3.

Table 4–2: The beam statistics of fields in plan-class NS1 are shown at the maximum dose point (Maximum) and the optimal dose gradient metric point (Optimal). Fields have been split into the 5 mm and 7.5 mm collimator portions. The average off-axis distance of the detector in the beams defined by each collimator is calculated, as well as the proportion of MU that is delivered using that collimator. The volume of the target for each clinical field has also been calculated.

Point in field	Collimator diameter (mm)	Off-axis distance (mm)	MU ratio
Clinical Field 1 (Target Volume = 598.1 mm^3)			
Maximum	5	6.1	67%
	7.5	6.1	33%
Optimal	5	4.9	67%
	7.5	5.1	33%
Clinical Field 2 (Target Volume = 540.0 mm^3)			
Maximum	5	6.0	73%
	7.5	5.3	27%
Optimal	5	4.9	73%
	7.5	4.9	27%
Clinical Field 3 (Target Volume = 806.1 mm^3)			
Maximum	5	5.4	44%
	7.5	6.5	56%
Optimal	5	5.9	44%
	7.5	6.1	56%

Some of the differences between each field are further illustrated in Table 4–2, where the beam statistics for each field in plan-class NS1 are shown at the maximum dose and optimal dose gradient metric points. A larger difference is observed in the detector distance off-axis between these two points for fields 1 and 2 than for field 3: for beams defined by the 5 mm collimator, the off-axis distance changed by approximately 1.2 mm in fields 1 and 2, but only by 0.5 mm in field 3; for beams defined by the 7.5 mm collimator, the off-axis distance changed by an average of 0.7 mm in fields 1 and 2, and by 0.4 mm in field 3. This, combined with the variation of the $k_{Q_{\text{clin}},Q_{\text{msr}}}^{f_{\text{clin}},f_{\text{msr}}}$ correction factor with the off-axis distance, confirms that

the difference in dosimetric conditions between the two points is larger for fields 1 and 2 than it is for field 3.

A PCSR field was not created or considered for the non-isocentric plan-classes, although the fields plan-class NT1 met the relevant criteria defined in Section 3.1.2 for the A16 and W1 detectors. The $k_{Q_{\text{clin}},Q_{\text{msr}}}^{f_{\text{clin}},f_{\text{msr}}}$ correction factors for clinical fields in the non-isocentric plan-class NT1 are similar to the $k_{Q_{\text{pcsr}},Q_{\text{msr}}}^{f_{\text{pcsr}},f_{\text{msr}}}$ of the PCSR field representing the isocentric plan-class IS1 (found in Figure 4–1a), to within 2.2%. The agreement increases to 1.2% if the A26 microchamber, having the largest correction factors, is excluded. Clinical fields in both plan-classes use the 5 mm collimator exclusively, however they do differ in certain ways. As the names imply, fields in plan-class IS1 are isocentric and planned on the skull path, while fields in plan-class NT1 are non-isocentric and planned on the trigeminal neuralgia path, having a smaller SAD of 700 mm versus 800 mm and utilizing a different set of beams. As described in Section 1.1.2, the beams comprising the clinical field in a non-isocentric delivery are not constrained to point at a common position; therefore the detector must be away from central axis in the beam penumbra for some subset of these beams. Francescon *et al.* have shown that the $k_{Q_{\text{clin}},Q_{\text{msr}}}^{f_{\text{clin}},f_{\text{msr}}}$ increases with decreasing SAD [22], and decreases for microchambers and the W1 as the respective detector moves away from central axis. This combination of effects results in a likely coincidental similarity of $k_{Q_{\text{clin}},Q_{\text{msr}}}^{f_{\text{clin}},f_{\text{msr}}}$ for the fields in plan classes IS1 and NT1. The creation of a non-isocentric PCSR field for this plan-class is non-trivial and must be done in careful consideration of the effect of overlapping beam penumbra on the $k_{Q_{\text{pcsr}},Q_{\text{msr}}}^{f_{\text{pcsr}},f_{\text{msr}}}$ correction factor.

The $k_{Q_{\text{clin}},Q_{\text{msr}}}^{f_{\text{clin}},f_{\text{msr}}}$ was found to depend on the position within the field for clinical fields in plan-classes NT2 and NS1, especially so for the latter. Furthermore, the intra-plan-class agreement was also seen to depend on this position, as there was better agreement at the optimal dose gradient metric point for plan-class NT2, while the variability was better at the maximum dose point for plan-class NS1; at each respective point, the variability in the $k_{Q_{\text{clin}},Q_{\text{msr}}}^{f_{\text{clin}},f_{\text{msr}}}$ was less than the maximum tolerable variation of 2%. Finally, the value of the

correction factors for fields in NS1 are lower in general than those for fields in NT2, despite both sets of fields using the same set of collimators. The major difference between the two plan-classes is the distribution of dose around the target: the dose is higher in the centre than on the periphery for fields in NT2, while the opposite is true for fields in NS1.

Since the $k_{Q_{\text{clin}},Q_{\text{msr}}}^{f_{\text{clin}},f_{\text{msr}}}$ depends not only on the set of collimators, but on the dose distribution and by extension the selection of the dose gradient metric used to select the optimal point, the creation of a PCSR field that adequately represents the clinical fields within its plan-class must be done by considering this dose distribution. Situations such as field 3 in plan-class NS1, in which the dose gradient metric point was determined to be on the periphery of the target instead of near the centre, pose further problems. If the optimal dose gradient metric point in a potential PCSR field for plan-class NS1 is near the centre, then fields such as field 3 will not be represented well by this PCSR field: the $k_{Q_{\text{clin}},Q_{\text{msr}}}^{f_{\text{clin}},f_{\text{msr}}}$ will be greater than from the $k_{Q_{\text{pcsr}},Q_{\text{msr}}}^{f_{\text{pcsr}},f_{\text{msr}}}$ by as much as 3%. Conversely, if the optimal dose gradient metric point in the PCSR field is on the periphery, then fields 1 and 2 will not be adequately represented, as the $k_{Q_{\text{clin}},Q_{\text{msr}}}^{f_{\text{clin}},f_{\text{msr}}}$ will be less than from the $k_{Q_{\text{pcsr}},Q_{\text{msr}}}^{f_{\text{pcsr}},f_{\text{msr}}}$ by as much as 3%. Further work must be done in order to investigate the creation of representative PCSR fields for CyberKnife clinical fields having these irregular dose distributions.

4.2.2 Intermediate Correction Factors

The intermediate correction factors, defined in Section 3.2.4, were calculated for fields 1, 2, and 3 in plan-class NS1, and can be seen in Figures 4–10, 4–11, and 4–12, respectively. The error bars represent the estimated statistical uncertainty in the calculated correction factors. Figures 4–10a, 4–11a, and 4–12a show the correction factors at the maximum dose point in each field, while Figures 4–10b, 4–11b, and 4–12b show the correction factors at the respective optimal dose gradient metric point. The intermediate correction factors for fields in plan-classes NT1 and NT2 were similar to those shown for the isocentric clinical fields using similar collimators (see Figures 4–4, 4–5, and 4–6). In general, $[P_{\rho}]_{Q_{\text{clin}},Q_{\text{msr}}}^{f_{\text{clin}},f_{\text{msr}}}$ and $[P_{\text{vol}}]_{Q_{\text{clin}},Q_{\text{msr}}}^{f_{\text{clin}},f_{\text{msr}}}$ presented the largest contributions to the total correction factors, representing

a density correction which is enhanced by a lack of lateral CPE in the smallest fields, and volume averaging in a non-uniform dose distribution, respectively. These two intermediate correction factors were larger for fields in plan-class NT1 than they were for fields in plan-class NT2. The latter plan-class used both the 5 mm and 7.5 mm collimators, whereas the former used only the 5 mm collimator, explaining the difference observed here.

The intermediate correction factors for clinical field 1 in plan-class NS1 share this behaviour at the maximum dose point only; this was also the point at which the total correction factor $k_{Q_{\text{clin}},Q_{\text{msr}}}^{f_{\text{clin}},f_{\text{msr}}}$ for this field was greater than 1 for the microchambers (see Figure 4–9a). At the optimal dose gradient metric point, as seen in Figure 4–9b, the total correction factor was less than 1; the intermediate correction factors in Figure 4–10b reveal why. The $[P_\rho]_{Q_{\text{clin}},Q_{\text{msr}}}^{f_{\text{clin}},f_{\text{msr}}}$ intermediate correction factor, indicating the degree of lack of CPE, is reduced to a value of approximately 1.2% above unity for the microchambers, from 4% and 5% (for the A16 and A26 microchambers, respectively). This suggests that at this optimal dose gradient metric point, the individual beams comprising the total clinical field probably combine in such a way as to bring about a situation of approximate CPE. This is true despite the fact that lateral CPE is never achieved in any singular beam, as each one utilizes a small collimator.

The $[P_{\text{vol}}]_{Q_{\text{clin}},Q_{\text{msr}}}^{f_{\text{clin}},f_{\text{msr}}}$ is also greatly reduced when moving from the point of maximum dose to the optimal dose gradient metric point. This intermediate correction factor is less than 1 for each detector investigated, implying that the dose in the centre of the detector active volume is less than the dose averaged over the entire active volume. This is due to the selection of the optimal dose gradient metric point in the central region of the target, receiving a lower dose than the periphery. This, along with the approximate CPE established at this point, defines dosimetric conditions that are highly unlike conditions typically observed in small fields (see Section 1.3.1).

Clinical field 2 was similar to field 1, as the optimal dose gradient metric point was also chosen to lie in the lower dose central region of the target. The intermediate correction factors for this field, shown in Figure 4–11, reveal a similar pattern to field 1, in which the

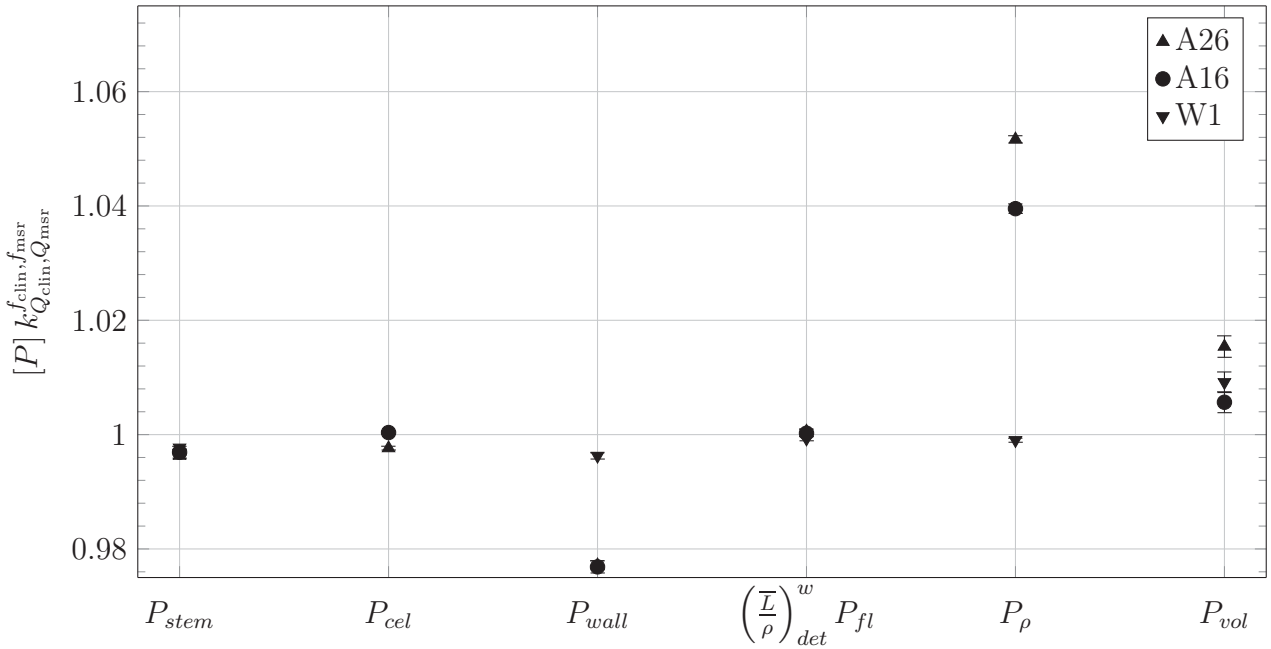

(a) $[P_c]^{f_{\text{clin}},f_{\text{msr}}}_{Q_{\text{clin}},Q_{\text{msr}}}$ at maximum dose point.

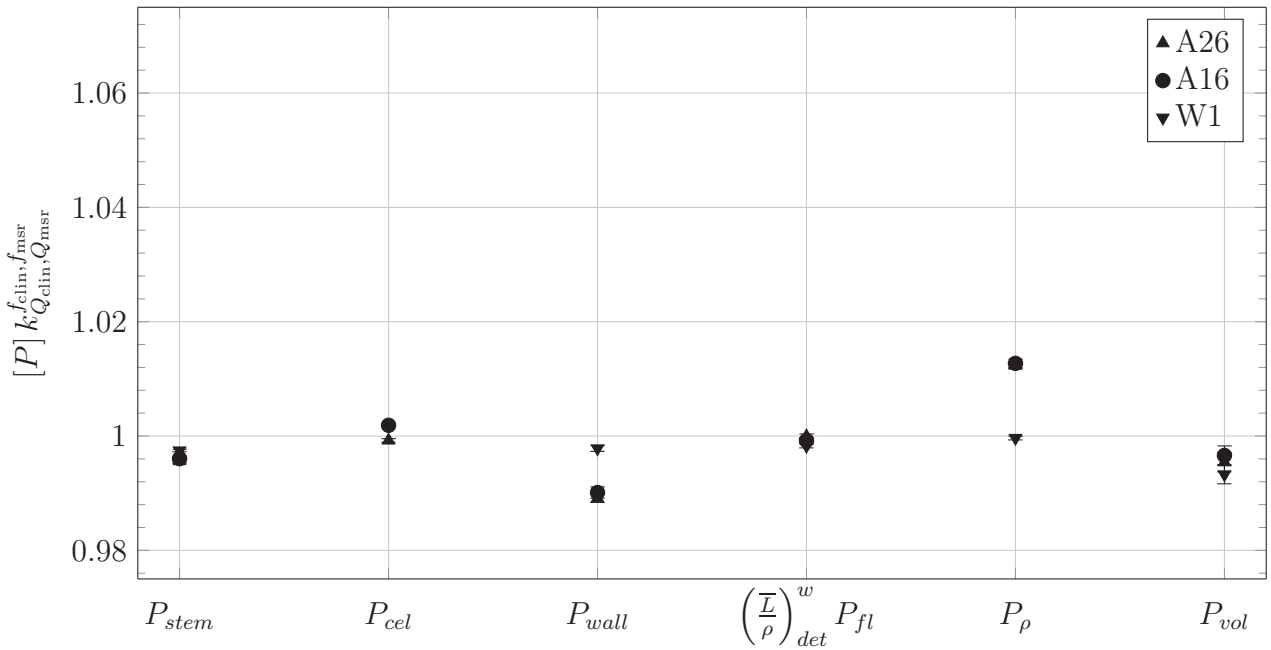

(b) $[P_c]^{f_{\text{clin}},f_{\text{msr}}}_{Q_{\text{clin}},Q_{\text{msr}}}$ at optimal dose gradient metric point.

Figure 4–10: Intermediate correction factors $[P_c]^{f_{\text{clin}},f_{\text{msr}}}_{Q_{\text{clin}},Q_{\text{msr}}}$ for clinical field 1 in plan-class NS1, at the point of maximum dose and the optimal dose gradient metric point.

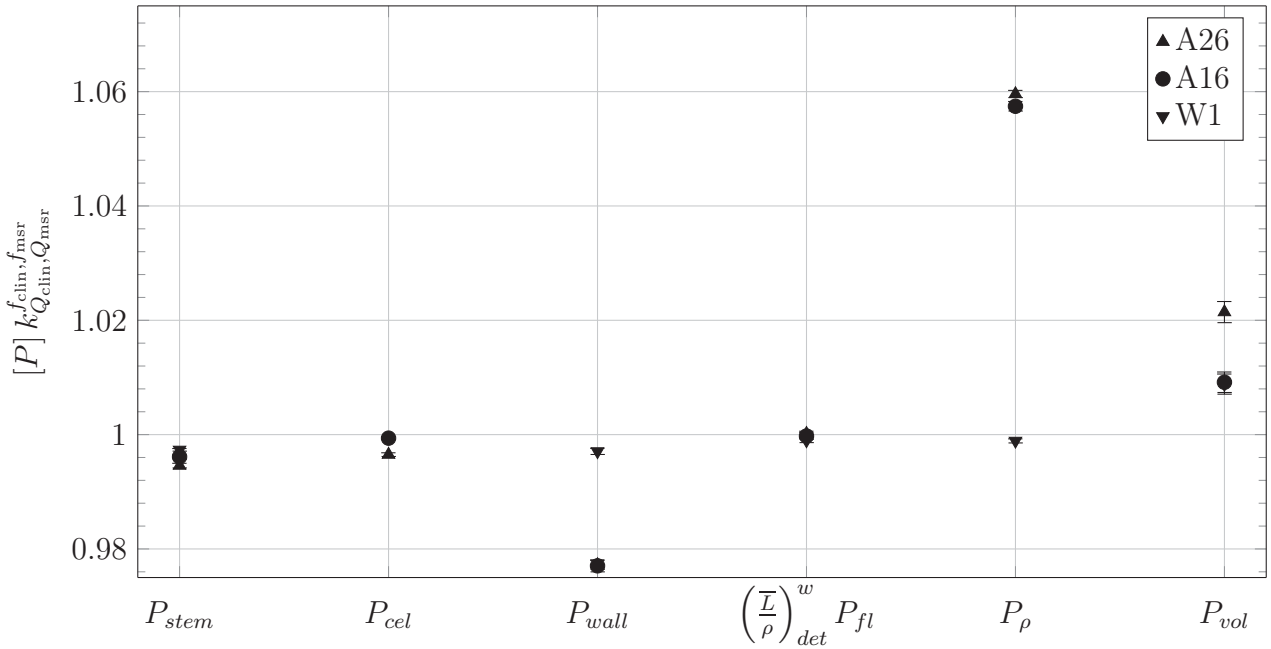

(a) $[P_c]^{f_{\text{clin}},f_{\text{msr}}}_{Q_{\text{clin}},Q_{\text{msr}}}$ at maximum dose point.

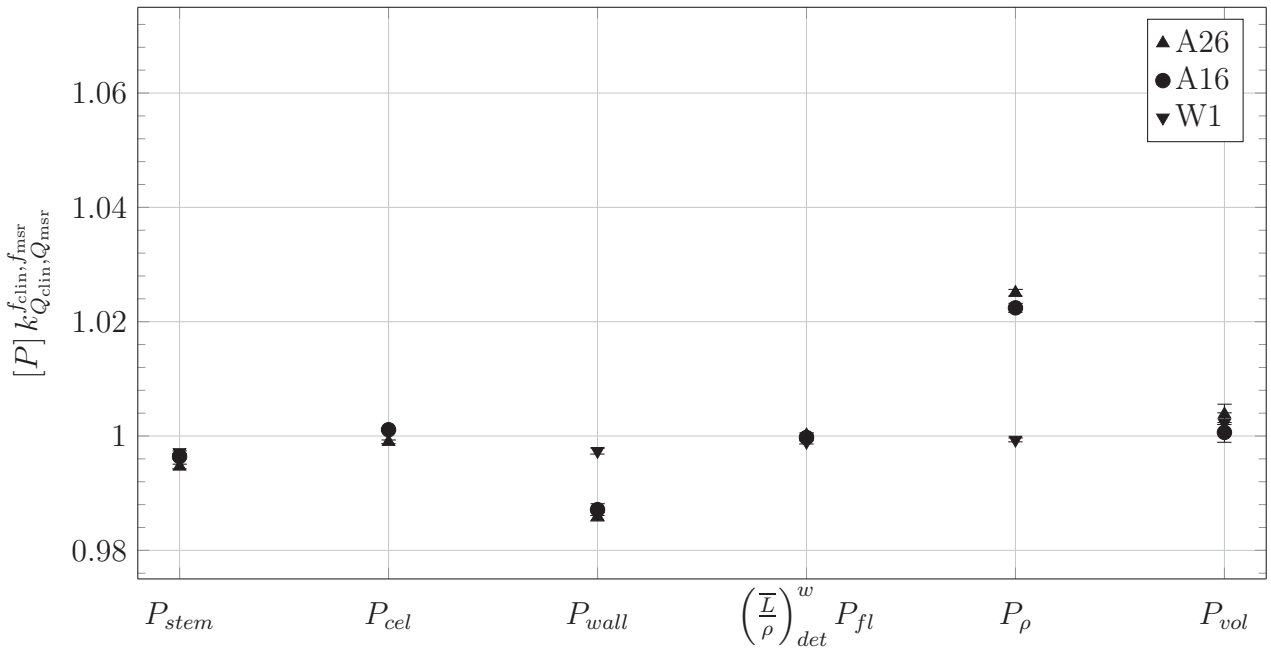

(b) $[P_c]^{f_{\text{clin}},f_{\text{msr}}}_{Q_{\text{clin}},Q_{\text{msr}}}$ at optimal dose gradient metric point.

Figure 4–11: Intermediate correction factors $[P_c]^{f_{\text{clin}},f_{\text{msr}}}_{Q_{\text{clin}},Q_{\text{msr}}}$ for clinical field 2 in plan-class NS1, at the point of maximum dose and the optimal dose gradient metric point.

$[P_\rho]^{f_{\text{clin}},f_{\text{msr}}}_{Q_{\text{clin}},Q_{\text{msr}}}$ and $[P_{\text{vol}}]^{f_{\text{clin}},f_{\text{msr}}}_{Q_{\text{clin}},Q_{\text{msr}}}$ decrease from the point of maximum dose to the optimal dose gradient metric point. Unlike field 1, however, the $[P_{\text{vol}}]^{f_{\text{clin}},f_{\text{msr}}}_{Q_{\text{clin}},Q_{\text{msr}}}$ is greater than 1 for all detectors, though only by as much as 0.4% for the A26 microchamber. Though not less than unity, these values are nevertheless unlike typical volume averaging correction factors for small clinical isocentric fields using the 5 mm and 7.5 mm collimators (see Figures 4–4 and 4–5 for the isocentric field intermediate correction factors), for which $[P_{\text{vol}}]^{f_{\text{clin}},f_{\text{msr}}}_{Q_{\text{clin}},Q_{\text{msr}}}$ can be as large as 8.1% above unity for the A26.

For field 3 of plan-class NS1, the optimal dose gradient metric point was calculated to lie on the high-dose periphery of the target instead of the low-dose centre, as was the case in fields 1 and 2. Because of this, each of the intermediate correction factors, including the $[P_\rho]^{f_{\text{clin}},f_{\text{msr}}}_{Q_{\text{clin}},Q_{\text{msr}}}$ and $[P_{\text{vol}}]^{f_{\text{clin}},f_{\text{msr}}}_{Q_{\text{clin}},Q_{\text{msr}}}$, were relatively constant between the point of maximum dose and the optimal dose gradient metric point, to within 0.4% (see Figure 4–12). The lack of lateral CPE is present at both points, as evidenced by the large $[P_\rho]^{f_{\text{clin}},f_{\text{msr}}}_{Q_{\text{clin}},Q_{\text{msr}}}$; volume averaging also perturbs the detector response to a similar degree at both points. Therefore the dosimetric conditions at the optimal dose point can be considered to be equivalent to those at the point of maximum dose, and to typical small field conditions. This is unlike fields 1 and 2, for which dosimetric conditions at the two points are highly unlike one another.

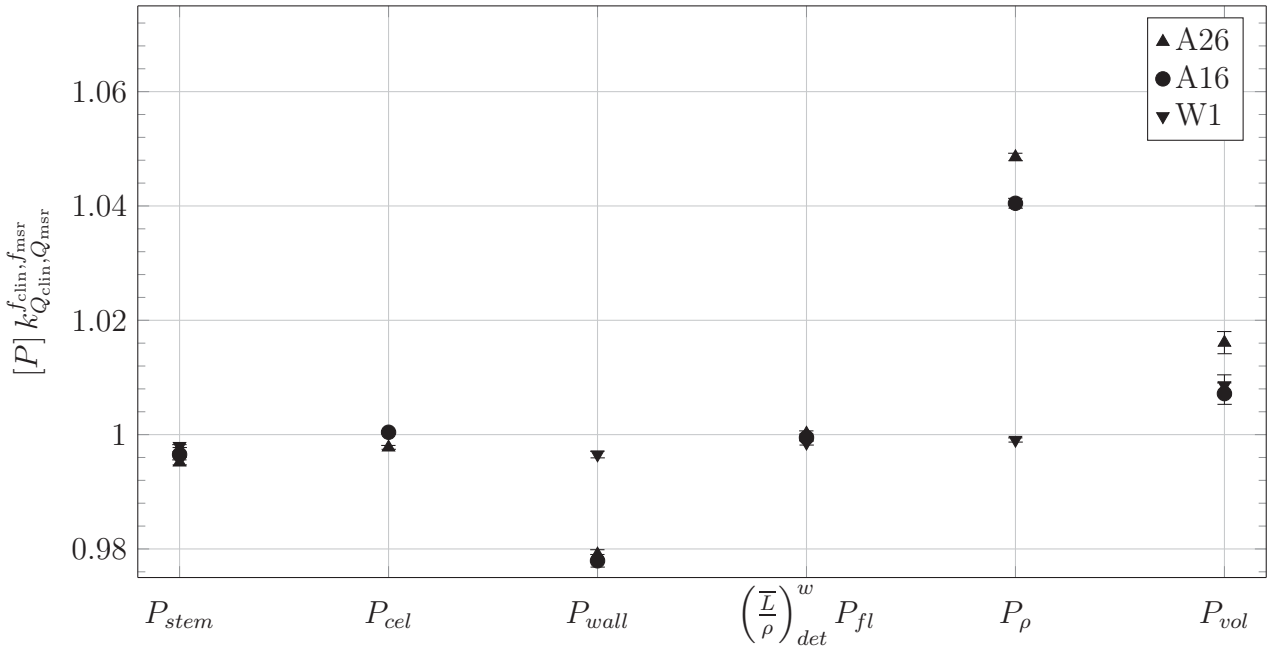

(a) $[P_c]_{Q_{\text{clin}},Q_{\text{msr}}}^{f_{\text{clin}},f_{\text{msr}}}$ at maximum dose point.

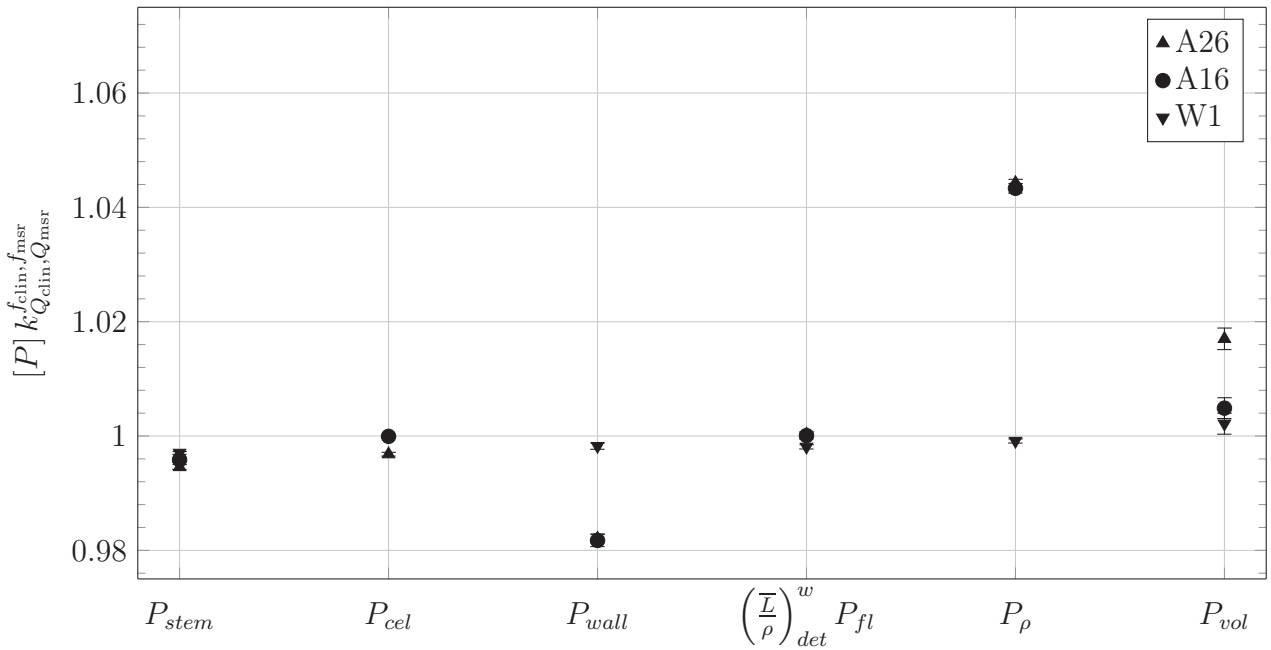

(b) $[P_c]_{Q_{\text{clin}},Q_{\text{msr}}}^{f_{\text{clin}},f_{\text{msr}}}$ at optimal dose gradient metric point.

Figure 4–12: Intermediate correction factors $[P_c]_{Q_{\text{clin}},Q_{\text{msr}}}^{f_{\text{clin}},f_{\text{msr}}}$ for clinical field 3 in plan-class NS1, at the point of maximum dose and the optimal dose gradient metric point.

CHAPTER 5
Conclusions and Future Work

In this study, total and intermediate correction factors were calculated for 21 CyberKnife composite fields employing the smallest collimators, 18 clinical and 3 PCSR. Calculations were done using the `egs_chamber` Monte Carlo user code. First, a model of the CyberKnife beam was constructed in BEAMnrc and subsequently verified by comparing measured dose distribution data to the corresponding Monte Carlo calculations. The large field (60 mm) PDD and small field (5 mm, 7.5 mm, and 10 mm) OARs and OFs were chosen for this comparison. These calculations were performed using a full model of the detector used to measure the data: the A16 microchamber.

Fields were grouped into plan-classes according to easily identifiable characteristics, such as the set of collimators that were used, the type of delivery (isocentric versus non-isocentric), and the beam path set used. A PCSR field was created for each isocentric plan-class, having the same characteristics as the class that it represented. The suitability of using this PCSR field as a representative field for dosimetry was explored, by calculating $k^{f_{\mathrm{pcsr}},f_{\mathrm{msr}}}_{Q_{\mathrm{pcsr}},Q_{\mathrm{msr}}}$ and $k^{f_{\mathrm{clin}},f_{\mathrm{pcsr}}}_{Q_{\mathrm{clin}},Q_{\mathrm{pcsr}}}$ correction factors. Correction factors were calculated for three detectors: the A16 and A26 microchambers, and the W1 plastic scintillator.

Both microchambers were found to require large $k^{f_{\mathrm{clin}},f_{\mathrm{msr}}}_{Q_{\mathrm{clin}},Q_{\mathrm{msr}}}$ factors greater than unity in order to correct for the differing chamber response in these fields relative to the MSR field, the 60 mm collimator. With the use of the intermediate correction factors, this difference in response was attributed primarily to the low density of the active volume of the microchambers relative to water and the volume averaging effect, through the $[P_\rho]^{f_{\mathrm{pcsr}},f_{\mathrm{msr}}}_{Q_{\mathrm{pcsr}},Q_{\mathrm{msr}}}$ and $[P_{\mathrm{vol}}]^{f_{\mathrm{pcsr}},f_{\mathrm{msr}}}_{Q_{\mathrm{pcsr}},Q_{\mathrm{msr}}}$ correction factors, respectively. As expected, the magnitude of the correction factor decreased as the collimator size increased, and the A26 chamber required larger correction factors than the A16 due to its larger active volume. For isocentric fields, correction

factors varied from 1.014 to 1.124 for the A16, and from 1.023 to 1.193 for the A26, depending on the collimator used. The values of $k_{Q_{\text{clin}},Q_{\text{msr}}}^{f_{\text{clin}},f_{\text{msr}}}$ for the A16 agree well with correction factors reported in the literature for this detector in static fields using the same collimator. While the A26 microchamber exceeds the requirements defined in the addendum to TG-51 for a reference-class ion chamber, the large correction factors calculated required for certain CyberKnife clinical fields may discourage its use as a dosimeter for patient-specific quality assurance.

The W1 plastic scintillator requires a correction factor only in clinical fields utilizing the smallest 5 mm collimator. In fields employing this collimator exclusively (i.e. fields in plan-classes IS1 and NT1), the correction factor may be as high as 3.6% above unity, and in fields using the 5 mm collimator in combination with the 7.5 mm collimator (i.e. fields in plan-classes NT2 and NS1), the $k_{Q_{\text{clin}},Q_{\text{msr}}}^{f_{\text{clin}},f_{\text{msr}}}$ is within 1.3% of 1. In all other fields (plan-classes IS2 and IS3), the correction factor is within 0.5% of unity. The small correction factors required for the W1 plastic scintillator can be attributed to its exclusive use of nearly water-equivalent materials, as well as a small active volume (1 mm diameter, 3 mm length). Indeed, for every field investigated, the volume averaging correction factor $[P_{\text{vol}}]_{Q_{\text{pcsr}},Q_{\text{msr}}}^{f_{\text{pcsr}},f_{\text{msr}}}$ was the sole contributor to the W1 total correction factor; this correction factor can be avoided if the dose to the bare active volume filled with water is considered instead of the dose to a point, as suggested by Bouchard *et al.* [8]. These results imply that the W1 plastic scintillator may be used to determine dose to water for the measurement of the $k_{Q_{\text{clin}},Q_{\text{msr}}}^{f_{\text{clin}},f_{\text{msr}}}$ correction factor specific to other detectors, for CyberKnife small clinical fields. This neglects the accuracy of the Cerenkov light removal calibration, which has not yet been verified for arbitrary clinical fields.

For the isocentric plan-classes, the PCSR field was determined to represent all three clinical fields evaluated in each class: the $k_{Q_{\text{clin}},Q_{\text{pcsr}}}^{f_{\text{clin}},f_{\text{pcsr}}}$ correction factors were within 1.5% for fields using the 5 mm collimator, which is less than the maximum tolerable variation of 2%

(see Section 3.1.2). The $k_{Q_{\text{clin}},Q_{\text{pcsr}}}^{f_{\text{clin}},f_{\text{pcsr}}}$ were within 0.7% for fields using the larger 7.5 mm and 10 mm collimators, below the ideal variation of $< 1\%$.

A PCSR field was not considered for the non-isocentric clinical fields in plan-classes NT1, NT2, and NS1, employing the 5 mm and 7.5 mm collimators. Although clinical fields in plan-classes NT2 and NS1 employed the same collimators, the correction factors for fields in class NT2, for which the dose was higher in the centre of the target than the periphery, were generally larger than those for fields in plan-class NS1. In addition to this, the point of measurement within the field was found to affect the value of the $k_{Q_{\text{clin}},Q_{\text{msr}}}^{f_{\text{clin}},f_{\text{msr}}}$ correction factor, as well as the intra-plan-class agreement of the correction factors. For plan-class NT2, the variability was reduced to 1.7% at the optimal dose gradient metric point $\vec{r}_{I_{min}}$, while the variability was best at the maximum dose point for plan-class NS1, at a maximum of 1.9%. Preferably, the agreement would be best for both plan-classes at the same point of measurement in the clinical field, either maximum dose or optimal dose gradient metric point, so that the calculation of $k_{Q_{\text{clin}},Q_{\text{msr}}}^{f_{\text{clin}},f_{\text{msr}}}$ for clinical fields in new plan-classes could be done at one point only.

The selection of the optimal dose gradient metric point for fields in plan-class NS1 was especially problematic, as this caused the relatively large variability of 4.2% seen in the $k_{Q_{\text{clin}},Q_{\text{msr}}}^{f_{\text{clin}},f_{\text{msr}}}$. For fields 1 and 2, this point was chosen to lie close to the centre of the target, in a low-dose, low-gradient region. The dosimetric conditions at this point in the field are such that the lack of lateral CPE is less severe than in the small static field case, and the volume averaging effect is negligible. This causes a decrease of the $[P_\rho]_{Q_{\text{pcsr}},Q_{\text{msr}}}^{f_{\text{pcsr}},f_{\text{msr}}}$ and $[P_{\text{vol}}]_{Q_{\text{pcsr}},Q_{\text{msr}}}^{f_{\text{pcsr}},f_{\text{msr}}}$ intermediate correction factors, respectively, and by consequence the $k_{Q_{\text{clin}},Q_{\text{msr}}}^{f_{\text{clin}},f_{\text{msr}}}$ correction factor is reduced to be less than or equal unity, depending on the field and detector. This is contrary to the usual behaviour for ion chamber correction factors in small fields, for which the correction factors are typically large and greater than 1. This behaviour is restored for field 3 in plan-class NS1, as the optimal dose gradient metric point was placed on the periphery of the target instead of the centre.

A solution to this problem is to simply select a point in a local minimum of the dose gradient distribution for each field in this plan-class; then the $k_{Q_{\text{clin}},Q_{\text{msr}}}^{f_{\text{clin}},f_{\text{msr}}}$ may be approximately equal to 1 for every clinical field. However, a robust algorithm is required to select this point, and such a point may not be available in all plans, some of which are more or less heterogeneous in dose throughout the target. The algorithm presented was anticipated to reduce the variability in $k_{Q_{\text{clin}},Q_{\text{msr}}}^{f_{\text{clin}},f_{\text{msr}}}$, but has failed in this respect, causing the large variability of the total correction factors between fields 1 and 2 and that of field 3 of the non-isocentric plan-class NS1. In addition, the point of measurement for the PCSR field must be selected in a dosimetrically similar region of the dose distribution, so that this field represents each clinical field within its class.

The problems outlined above arose only in clinical fields using multiple collimators; special consideration may therefore be required for these fields. One possible area of future investigation is the splitting up of the total clinical field into subfields only comprising beams using a single collimator. As seen in the isocentric plan-classes, the $k_{Q_{\text{clin}},Q_{\text{msr}}}^{f_{\text{clin}},f_{\text{msr}}}$ depends heavily on the collimator used, therefore calculating the correction factor separately for each collimator could provide some insight as to the differing behaviour seen at the maximum dose and optimal dose gradient metric points for plan-classes NT2 and NS1. An additional benefit to this method is that clinical fields are delivered in such a way that all beams employing each fixed collimator are delivered sequentially. Therefore correction factors may be applied to the detector readings for each collimator, instead of to the reading for the entire field. It should be noted that this method is only applicable to fixed collimators: this solution is not possible for the iris variable aperture collimator or the InCise MLC version of CyberKnife.

An additional problem facing the application of the PCSR field to non-isocentric fields especially is the large complexity and variation in CyberKnife clinical fields. Table 4–2 lists the target volume, average off-axis distance, and ratio of MU delivered by each collimator for the three clinical fields in the non-isocentric plan class NS1. A large variability of these properties, and thus in the $k_{Q_{\text{clin}},Q_{\text{msr}}}^{f_{\text{clin}},f_{\text{msr}}}$ correction factors, is observed. This is true despite the

fact that these clinical fields employ the same set of collimators, and treat the same target (acoustic neuroma) with a similar dose distribution (high dose on the periphery, low dose in the centre of the target). A much larger variation in field properties is seen when considering all CyberKnife clinical non-isocentric fields. This may be accompanied by a large variation in the $k_{Q_{\text{clin}},Q_{\text{msr}}}^{f_{\text{clin}},f_{\text{msr}}}$, implying that a large number of plan-classes and PCSR fields are needed, with only a small number of clinical fields in each plan-class. This could potentially limit the benefit of the plan-class formalism for non-isocentric clinical fields delivered by CyberKnife, as applied in this study. Kamio and Bouchard have demonstrated a correlation between a uniformity index, representing the variation of photon fluence within a field, and the upper bound of the $k_{Q_{\text{clin}},Q_{\text{msr}}}^{f_{\text{clin}},f_{\text{msr}}}$ correction factor for small and composite IMRT fields [52]. A similar study may be carried out for CyberKnife fields in order to investigate if this behaviour can be replicated.

It has been shown that the W1 may be used to determine dose to water without correction for the measurement of the $k_{Q_{\text{clin}},Q_{\text{msr}}}^{f_{\text{clin}},f_{\text{msr}}}$ correction factor for CyberKnife small clinical fields not employing the 5 mm collimator. These measurements of the $k_{Q_{\text{clin}},Q_{\text{msr}}}^{f_{\text{clin}},f_{\text{msr}}}$ should be performed for the A16 and A26 microchambers for a select number of isocentric and non-isocentric fields. This will accomplish two goals, the first of which is to prove the feasibility of using the W1 plastic scintillator as a dose to water detector in these clinical fields. Although this detector requires corrections for the Cerenkov light contamination, it is nonetheless more simple to operate than other dosimeters which have been used for this purpose, including alanine, radiochromic film, and ferrous sulfate dosimetry. Second, and more importantly, the experimental measurement of the microchamber $k_{Q_{\text{clin}},Q_{\text{msr}}}^{f_{\text{clin}},f_{\text{msr}}}$ correction factors will provide a means to validate the Monte Carlo results presented in this thesis. This will permit the application of these correction factors, and this formalism of correction factor calculation, to measurements performed within actual clinical fields. The accuracy of the experimentally

determined absorbed dose to water for patient-specific quality assurance will therefore improve in the dosimetrically challenging conditions present in small field treatments routinely delivered by CyberKnife.

REFERENCES

[1] E. B. Podgorsak, *Radiation Physics for Medical Physicists*. New York: Springer Berlin Heidelberg, 2006.

[2] E. B. Podgorsak, Ed., *Radiation Oncology Physics: A Handbook for Teachers and Students*. Vienna: International Atomic Energy Agency, 2005.

[3] Y. Xiao, S. F. Kry, R. Popple, E. Yorke, N. Papanikolaou, S. Stathakis, P. Xia, S. Huq, J. Bayouth, J. Galvin, and F.-F. Yin, "Flattening filter-free accelerators: a report from the AAPM Therapy Emerging Technology Assessment Work Group," *Journal of Applied Clinical Medical Physics*, vol. 16, no. 3, pp. 12–29, 2015.

[4] E. H. Balagamwala, S. T. Chao, and J. Suh, "Principles of radiobiology of stereotactic radiosurgery and clinical applications in the central nervous system," *Technology in Cancer Research and Treatment*, vol. 11, no. 1, pp. 3–13, 2012.

[5] P. R. Almond, P. J. Biggs, B. M. Coursey, W. F. Hanson, M. S. Huq, R. Nath, and D. W. O. Rogers, "AAPM's TG-51 protocol for clinical reference dosimetry of high-energy photon and electron beams," *Medical Physics*, vol. 26, no. 9, pp. 1847–1870, 1999.

[6] M. McEwen, L. DeWerd, G. Ibbott, D. Followill, D. W. O. Rogers, S. Seltzer, and J. Seuntjens, "Addendum to the AAPM's TG-51 protocol for clinical reference dosimetry of high-energy photon beams," *Medical Physics*, vol. 41, no. 4, p. 041501, 2014.

[7] B. R. Muir and D. W. O. Rogers, "Monte Carlo calculations of k_Q, the beam quality conversion factor," *Medical Physics*, vol. 37, no. 11, pp. 5939–5950, 2010.

[8] H. Bouchard, J. Seuntjens, J.-F. Carrier, and I. Kawrakow, "Ionization chamber gradient effects in nonstandard beam configurations," *Medical Physics*, vol. 36, no. 10, pp. 4654–4663, 2009.

[9] M. R. McEwen, "Measurement of ionization chamber absorbed dose k_Q factors in megavoltage photon beams," *Medical Physics*, vol. 37, no. 5, pp. 2179–2193, 2010.

[10] B. R. Muir, M. R. McEwen, and D. W. O. Rogers, "Measured and Monte Carlo calculated k_Q factors: Accuracy and comparison," *Medical Physics*, vol. 38, no. 8, p. 4600, 2011.

[11] E. Yorke, R. Alecu, L. Ding, D. Fontenla, A. Kalend, D. Kaurin, M. E. Masterson-McGary, G. Marinello, T. Matzen, A. Saini, J. Shi, W. Simon, T. C. Zhu, and X. R. Zhu, "Diode *in vivo* dosimetry for patients receiving external beam radiation therapy," American Association of Physicists in Medicine, Madison, Tech. Rep. 87, 2005.

[12] M. Guillot, L. Gingras, L. Archambault, S. Beddar, and L. Beaulieu, "Spectral method for the correction of the Cerenkov light effect in plastic scintillation detectors: A comparison study of calibration procedures and validation in Cerenkov light-dominated situations," *Medical Physics*, vol. 38, no. 4, pp. 2140–2150, 2011.

[13] R. Alfonso, P. Andreo, R. Capote, M. S. Huq, W. Kilby, P. Kjäll, T. R. Mackie, H. Palmans, K. Rosser, J. Seuntjens, W. Ullrich, and S. Vatnitsky, "A new formalism for reference dosimetry of small and nonstandard fields," *Medical Physics*, vol. 35, no. 11, pp. 5179–5186, 2008.

[14] I. J. Das, G. X. Ding, and A. Ahnesjö, "Small fields: Nonequilibrium radiation dosimetry," *Medical Physics*, vol. 35, no. 1, pp. 206–215, 2008.

[15] X. A. Li, M. Soubra, J. Szanto, and L. H. Gerig, "Lateral electron equilibrium and electron contamination in measurements of head-scatter factors using miniphantoms and brass caps," *Medical Physics*, vol. 22, no. 7, pp. 1167–1170, 1995.

[16] P. Francescon, S. Beddar, N. Satariano, and I. J. Das, "Variation of $k_{Q_{\text{clin}},Q_{\text{msr}}}^{f_{\text{clin}},f_{\text{msr}}}$ for the small-field dosimetric parameters percentage depth dose, tissue-maximum ratio, and off-axis ratio," *Medical Physics*, vol. 41, no. 10, p. 101708, 2014.

[17] U. Fano, "Note on the Bragg-Gray cavity principle for measuring energy dissipation," *Radiation Research*, vol. 1, no. 3, pp. 237–240, 1954.

[18] A. J. D. Scott, S. Kumar, A. E. Nahum, and J. D. Fenwick, "Characterizing the influence of detector density on dosimeter response in non-equilibrium small photon fields," *Physics in Medicine and Biology*, vol. 57, no. 14, pp. 4461–4476, 2012.

[19] P. Francescon, S. Cora, and C. Cavedon, "Total scatter factors of small beams: A multidetector and Monte Carlo study," *Medical Physics*, vol. 35, no. 2, pp. 504–513, 2008.

[20] P. Francescon, S. Cora, C. Cavedon, and P. Scalchi, "Application of a Monte Carlo-based method for total scatter factors of small beams to new solid state micro-detectors," *Medical Physics*, vol. 10, no. 1, pp. 147–152, 2009.

[21] P. Francescon, W. Kilby, N. Satariano, and S. Cora, "Monte Carlo simulated correction factors for machine specific reference field dose calibration and output factor measurement using fixed and iris collimators on the CyberKnife system," *Medical Physics*, vol. 57, no. 12, pp. 3741–3758, 2012.

[22] P. Francescon, W. Kilby, and N. Satariano, "Monte Carlo simulated correction factors for output factor measurement with the CyberKnife system-results for new detectors and correction factor dependence on measurement distance and detector orientation," *Medical Physics*, vol. 59, no. 6, pp. N11–N17, 2014.

[23] P. Papaconstadopoulos, F. Tessier, and J. Seuntjens, "On the correction, perturbation and modification of small field detectors in relative dosimetry," *Physics in Medicine and Biology*, vol. 59, no. 19, pp. 5937–5952, 2014.

[24] A. S. Beddar, T. R. Mackie, and F. H. Attix, "Water-equivalent plastic scintillation detectors for high- energy beam dosimetry: I. Physical characteristics and theoretical considerations," *Physics in Medicine and Biology*, vol. 37, no. 10, pp. 1883–1900, 1992.

[25] A. S. Beddar, T. M. Briere, F. A. Mourtada, O. N. Vassiliev, H. H. Liu, and R. Mohan, "Monte Carlo calculations of the absorbed dose and energy dependence of plastic scintillators," *Medical Physics*, vol. 32, no. 5, pp. 1265–1269, 2005.

[26] L. L. W. Wang, D. Klein, and A. S. Beddar, "Monte Carlo study of the energy and angular dependence of the response of plastic scintillation detectors in photon beams," *Medical Physics*, vol. 37, no. 10, pp. 5279–5286, 2010.

[27] L. L. W. Wang and S. Beddar, "Study of the response of plastic scintillation detectors in small-field 6 MV photon beams by Monte Carlo simulations," *Medical Physics*, vol. 38, no. 3, pp. 1596–1599, 2011.

[28] A. Gago-Arias, E. Antolín, F. Fayos-Ferrer, S. Rocío, D. M. González-Castaño, H. Palmans, P. Sharpe, F. Gómez, and J. Pardo-Montero, "Correction factors for ionization chamber dosimetry in CyberKnife: Machine-specific, plan-class, and clinical fields," *Medical Physics*, vol. 40, no. 1, p. 011721, 2013.

[29] P. Francescon, S. Cora, and N. Satariano, "Calculation of $k_{Q_{\mathrm{clin}},Q_{\mathrm{msr}}}^{f_{\mathrm{clin}},f_{\mathrm{msr}}}$ for several small detectors and for two linear accelerators using Monte Carlo simulations," *Medical Physics*, vol. 38, no. 12, pp. 6513–6527, 2011.

[30] L. Archambault, A. S. Beddar, L. Gingras, F. Lacroix, R. Roy, and L. Beaulieu, "Water-equivalent dosimeter array for small-field external beam radiotherapy," *Medical Physics*, vol. 34, no. 5, pp. 1583–1592, 2007.

[31] J.-C. Gagnon, D. Thériault, M. Guillot, L. Archambault, S. Beddar, L. Gingras, and L. Beaulieu, "Dosimetric performance and array assessment of plastic scintillation detectors for stereotactic radiosurgery quality assurance," *Medical Physics*, vol. 39, no. 1, p. 429, 2012.

[32] M. McEwen, "SU-ET-172: Evaluation of the Exradin A26 Ion Chamber in Megavoltage Photon Beams as a Reference Class Instrument," *Medical Physics*, vol. 42, no. 6, p. 262, 2014.

[33] D. W. O. Rogers, B. A. Faddegon, G. X. Ding, C.-M. Ma, J. We, and T. R. Mackie, "BEAM: A Monte Carlo code to simulate radiotherapy treatment units," *Medical Physics*, vol. 22, no. 5, pp. 503–524, 1995.

[34] I. Kawrakow, "Accurate condensed history Monte Carlo simulation of electron transport. I. EGSnrc, the new EGS44 version," *Medical Physics*, vol. 27, no. 3, pp. 485–498, 2000.

[35] I. Kawrakow and D. W. O. Rogers, "The EGSnrc Code System: Monte Carlo Simulation of Electron and Photon Transport," National Research Council of Canada, Ottawa, Canada, Tech. Rep., 2000.

[36] J. Wulff, K. Zink, and I. Kawrakow, "Efficiency improvements for ion chamber calculations in high energy photon beams," *Medical Physics*, vol. 35, no. 4, pp. 1328–1336, 2008.

[37] ICRU, "Stopping Powers for Electrons and Positrons," International Commission in Radiation Units and Measurement, Washington, DC, Tech. Rep., 1984.

[38] M. J. Berger, J. S. Coursey, M. A. Zucker, and J. Chang, "ESTAR, PSTAR, and ASTAR: Computer Programs for Calculation Stopping-Power and Range Tables for Electrons, Protons, and Helium ions," 2005. [Online]. Available: http://physics.nist.gov/Star

[39] D. Sheikh-Bagheri and D. W. O. Rogers, "Sensitivity of megavoltage photon beam Monte Carlo simulations to electron beam and other parameters," *Medical Physics*, vol. 29, no. 3, pp. 379–390, 2002.

[40] S. S. Almberg, J. Frengen, A. Kylling, and T. Lindmo, "Monte Carlo linear accelerator simulation of megavoltage photon beams: Independent determination of initial beam parameters," *Medical Physics*, vol. 39, no. 1, pp. 40–47, 2012.

[41] D. Sheikh-Bagheri, D. W. Rogers, C. K. Ross, and J. P. Seuntjens, "Comparison of measured and Monte Carlo calculated dose distributions from the NRC linac," *Medical Physics*, vol. 27, no. 10, pp. 2256–2266, 2000.

[42] I. J. Das, C.-W. Cheng, R. J. Watts, A. Ahnesjö, J. Gibbons, X. A. Li, J. Lowenstein, R. K. Mitra, W. E. Simon, and T. C. Zhu, "Accelerator beam data commissioning equipment and procedures: Report of the TG-106 of the Therapy Physics Committee of the AAPM," *Medical Physics*, vol. 35, no. 9, pp. 4186–4215, 2008.

[43] E. S. M. Ali and D. W. O. Rogers, "Efficiency improvements of x-ray simulations in EGSnrc user-codes using bremsstrahlung cross-section enhancement (BCSE)," *Medical Physics*, vol. 34, no. 6, pp. 2143–2154, 2007.

[44] I. Kawrakow, D. W. O. Rogers, and B. R. B. Walters, "Large efficiency improvements in BEAMnrc using directional bremsstrahlung splitting," *Medical Physics*, vol. 31, no. 10, pp. 2883–2898, 2004.

[45] O. Chibani and C.-M. C. Ma, "On the discrepancies between Monte Carlo dose calculations and measurements for the 18 MV Varian photon beam," *Medical Physics*, vol. 34, no. 4, pp. 1206–1216, 2007.

[46] C.-M. Ma and A. E. Nahum, "Calculation of absorbed dose ratios using correlated Monte Carlo sampling," *Medical Physics*, vol. 20, no. 4, pp. 1189–1199, 1993.

[47] L. A. Buckley, I. Kawrakow, and D. W. O. Rogers, "CSnrc: correlated sampling Monte Carlo calculations using EGSnrc," *Medical Physics*, vol. 31, no. 12, pp. 3425–3435, 2004.

[48] I. Kawrakow and B. R. B. Walters, "Efficient photon beam dose calculations using DOSXYZnrc with BEAMnrc," *Medical Physics*, vol. 33, no. 8, pp. 3046–3056, 2006.

[49] G. A. Ezzell, J. M. Galvin, D. Low, J. R. Palta, I. Rosen, M. B. Sharpe, P. Xia, Y. Xiao, L. Xing, and C. X. Yu, "Guidance document on delivery, treatment planning, and clinical implementation of IMRT: Report of the IMRT subcommittee of the AAPM radiation therapy committee," vol. 30, no. 8, pp. 2089–2115, 2003.

[50] S. Dieterich, C. Cavedon, C. F. Chuang, A. B. Cohen, J. A. Garrett, C. L. Lee, J. R. Lowenstein, M. F. d'Souza, D. D. J. Taylor, X. Wu, and C. Yu, "Report of AAPM TG 135: Quality assurance for robotic radiosurgery," vol. 38, no. 6, pp. 2914–2936, 2011.

[51] C.-M. Ma, J. Li, J. Deng, and J. Fan, "Implementation of Monte Carlo Dose calculation for CyberKnife treatment planning," *Journal of Physics: Conference Series*, vol. 102, p. 012016, 2008.

[52] Y. Kamio and H. Bouchard, "Correction-less dosimetry of nonstandard photon fields: a new criterion to determine the usability of radiation detectors," *Physics in Medicine and Biology*, vol. 59, no. 17, pp. 4973–5002, 2014.